UCRL-52955

Mirror Fusion Test Facility magnet system— Final design report

C. D. Henning
A. J. Hodges
J. H. VanSant
E. N. Dalder
R. E. Hinkle
J. A. Horvath
R. M. Scanlan
D. W. Shimer
R. W. Baldi
R. E. Tatro

September 3, 1980

UCRL-52955
Distribution Category UC-20

Mirror Fusion Test Facility magnet system— Final design report

C. D. Henning
A. J. Hodges
J. H. VanSant
E. N. Dalder
R. E. Hinkle
J. A. Horvath
R. M. Scanlan
D. W. Shimer
R. W. Baldi
R. E. Tatro

Manuscript date: September 3, 1980

LAWRENCE LIVERMORE LABORATORY
University of California • Livermore, California • 94550

Available from: National Technical Information Service • U.S. Department of Commerce
5285 Port Royal Road • Springfield, VA 22161 • $10.00 per copy • (Microfiche $3.50)

ACKNOWLEDGMENTS

The authors wish to acknowledge the many contributions of all those who worked on the magnet design. Special credit is given to the following persons:

Andersen, A.
Berkey, J.
Bulmer, R.
Chang, Y.
Cornish, D. N.
Depue, D.
Johnson, G. L.
Karpenko, V. N.
Kozman, T. A.
Lathrop, G.
Lietske, J.
MacDonald, J.
Martinek, R.
Montoya, C.
Peterson, R.
Podesta, D.
Ross, W. N.
Shook, W. R.
Thomassen, K. I.
Witherell, C.
Zimmerman, B.
Jones, R. G.—General Dynamics/Convair
O'Neil, R. F.—General Dynamics/Convair
Roy, C. E.—General Dynamics/Convair

TABLE OF CONTENTS

Mirror Fusion Test Facility magnet system— Final design report

SECTION 1
MAGNET DESCRIPTION

The Mirror Fusion Test Facility (MFTF) is the largest of the mirror program experiments for magnetic fusion energy It seeks to combine and extend the near-classical plasma confinement achieved in 2XIIB[1] with the most advanced neutral beam and magnet technologies available. The product of ion density and confinement time will be improved while the superconducting magnet weight will be extrapolated from 15 tons in Baseball II[2] to 375 tons in MFTF. Other project parameters listed in Table 1 show that the MFTF will traverse much of the distance in magnet technology towards the reactor regime.[3]

Authorized to start construction in FY 1978, the MFTF project is close to its schedule for completion in October 1981. Following a change in geometry at the end of the preliminary design stage, detailed design was commenced in May 1978. By August of 1979 the design was complete and the first coil constructed. The second coil was finished in March 1980. Final assembly, including the case structure, will be completed and ready for test in early 1981. An extension of the project called MFTF-B has been authorized and will delay project completion three years.

MAGNET DESIGN

Figure 1 is a computer graphics display of the MFTF magnet with neutral-beam injection access. The magnet is a yin-yang pair with an average major radius of 2.5 m and an average minor radius of 0.75 m. The geometrical centers of the pair are overlapped by 0.7 m to produce a net outside dimension of about 8 m and a plasma length between mirrors of 3.6 m. A peak magnetic field of 7.68 T occurs at the windings in the minor radius. Because the field is a cusped magnetic well, it drops rapidly to 4.2 T at the mirrors and 2.0 T in the center.

A current-versus-field curve is shown in Fig. 2, with superconductor stability limits determined from test coil results reported by Cornish, et al.[4] The conductor exhibits cold-end recovery, and the stability limit appears to extrapolate in accordance with the copper magnet resistance and a modest surface heat flux of 0.19 $W \cdot cm^{-2}$. This experimental observation can be explained by averaging heat fluxes of 0.4 $W \cdot cm^{-2}$ and 0.1 $W \cdot cm^{-2}$ over the open external and restricted internal cooling surfaces, in accordance with usual heat transfer experiments.

The MFTF conductor is the result of a two-year development effort.[5] Listed in Table 2 are the

TABLE 1. MFTF parameters.

Parameter	Value
Plasma:	
Ion density × containment time, $s \cdot cm^{-3}$	10^{12}
Ion temperature, keV	50
Electron temperature, keV	1
Plasma/magnetic pressure	0.5
Startup beams, A, keV	1000, 20
Sustaining beams, A, keV	750, 80
Magnet:	
Maximum field, T	7.68
Central field, T	2.0
Mirror ratio	2.1:1
Mirror-to-mirror length, m	3.6
Major radius (mean), m	2.5
Minor radius (mean), m	0.75
Current, A	5775
Turns	1392
Stored energy, MJ	409
Conductor current density, $A \cdot cm^{-2}$	3729
Coil current density, $A \cdot cm^{-2}$	2525
Surface heat flux, $W \cdot cm^{-2}$	0.19
Conductor length, km	50
Total weight, kg	341,000

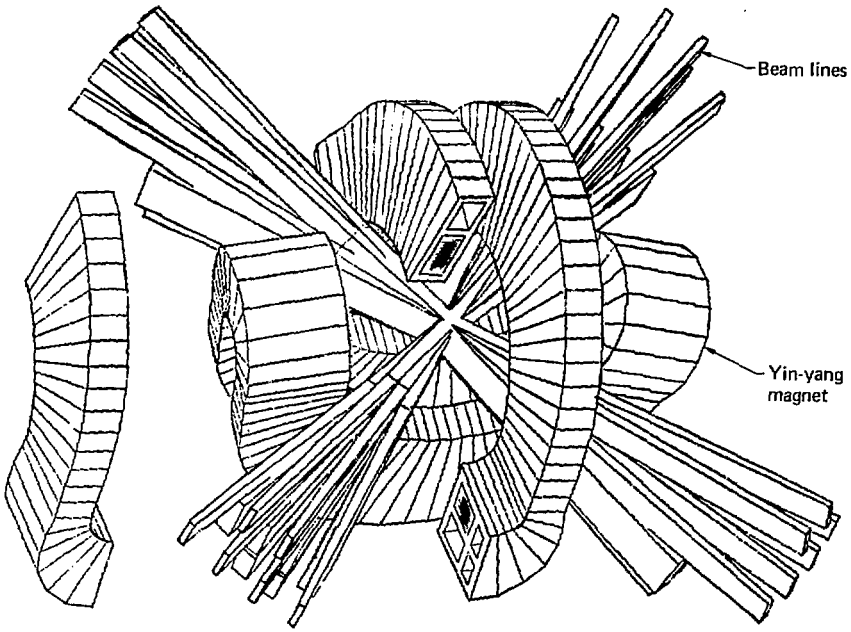

FIG. 1. Computer graphic display of MFTF magnet with neutral beam injection access.

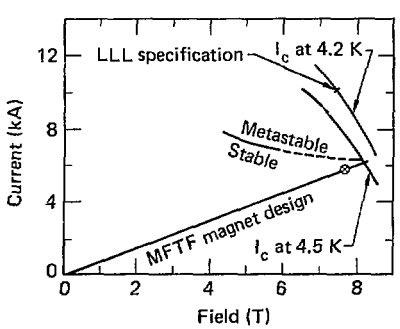

FIG. 2. MFTF magnet load line.

primary specifications of both the core and stabilized conductor. It consists of a 6.5-mm-square, copper-stabilized, niobium-titanium composite wrapped in an embossed and perforated sheath of high-purity copper. The core-to-sheath bond had to be improved by replacing the original 90/10 Pb-Sn solder with 50/50 Pb-Sn solder for improved wetability at lower bonding temperature. Once initial manufacturing difficulties were resolved, both quality and production efficiency were good.

A typical cross section of the coil is shown in Fig. 3. An inner coil form of 316L stainless steel is leveled with epoxy and glass fibers. Then five overlapping layers of Kapton film are installed as a ground-plane insulation. Perforated NEMA G-11 epoxy-glass laminate is placed on top of the Kapton for helium circulation before the 58 layers (24 turns

TABLE 2. MFTF conductor specifications.

Conductor parameters	Value
Superconductor:	
Critical current, kA at 7.5 T, 4.2 K	10
Copper to superconductor	1.7:1
Number of filaments	480
Filament diameter, mm	0.20
Twist pitch, mm	180
Conductor-resistance ratio	150:1
Core size, mm	6.5 × 6.5
Stabilized conductor:	
Maximum conductor field, T	7.68
Maximum conductor current, A	5775
Conductor operating temperature, K	4.5
Overall: copper to superconductor ratio	6.7:1
Stabilizer copper-resistance ratio	220:1
Copper resistance (at 7.68 T, 4.5 K), nΩ·cm	46
Helium-cooled surface area, $cm^2 \cdot cm^{-1}$	8.17
Required heat transfer rate, $W \cdot cm^{-2}$	0.19
Overall size, mm	12.4 × 12.4

each) of conductor are wound. After closing the Kapton ground-plane insulation around the coil, two sheets of Mylar are installed as a slip plane.

In the small-radius area, an additional crushable Dacron-felt layer is applied for controlled spacing. All other spaces are filled with G-11 blocks and fiber-filled epoxy before the outer coil jacket is welded in place.

A stainless-steel bladder is installed around the encased coil so a urethane shim can be injected between the coil jacket and structure. Disks welded to the inner structure surface preserve conductance through the guard-vacuum space for differential pumping. This arrangement greatly relaxes the helium-leakage requirements for both the coil jacket and structure.

The coil-winding operation is shown in Fig. 4. A tension of 600 lb is maintained on the conductor to control the accumulation of winding tolerances below 0.005 in. (0.12 mm) per turn. Compaction tests on conductor stacks and computer modeling of the winding motion confirmed that such tolerances were compatible with the allowable conductor strain. On initial energizing the conductor strain is 0.3%, but is reduced to 0.1% for repeated stress cycles. No degradation has been observed for niobium-titanium conductors at these strain levels.[6]

Conductor joints are made by cold welding the central core and soldering the conductor into a copper tray. The joint exceeds the strength and stability of the core and is redundant, so that some quality control problems experienced with the cold welding were alleviated.

Figure 5 shows the coil-winding rate. Much of the rate improvement was associated with the efficiency in joint making. Once mastered, joints were routinely made in less than four hours. Figure 6 shows the first completed coil being removed from the winder for placement on the shim-bladder assembly stand before the structure is welded around the coil.

THERMAL AND QUENCH PROTECTION

Thermal conditions for the magnet are summarized in Table 3. More than 8,000 liters of liquid helium will circulate by natural convection between the magnet and a storage Dewar located on the fourth floor of the building. The convection is the result of heat input to the magnet. A computer model of the helium loop was developed from the Blasius friction equation, Darcy's porous media equation, and a three-dimensional orifice model.[7] Estimates of effective hydraulic diameter, flow tortuosity, porosity, permeability, friction factor, and effective orifice dimensions were made for the magnet and connection piping. The effects of two-phase flow were included by using the Lockhart-Martenelli correlation.[8] Helium flow rates were estimated by an iterative method corresponding to an

TABLE 3. Thermal conditions in the magnet.

Parameter	Location	Value
Helium temperature, K	Magnet inlet	4.36
Pressure, kPa at 1.28 atm	Magnet bottom	130
Saturation temperature, K	Magnet bottom	4.52
Helium rate (natural circulation), g/s		≃700
Heat load, W	Magnet	≃350
Mean quality of helium, %	Magnet outlet	<5
Minimum transition temperature, K	Conductor	4.98

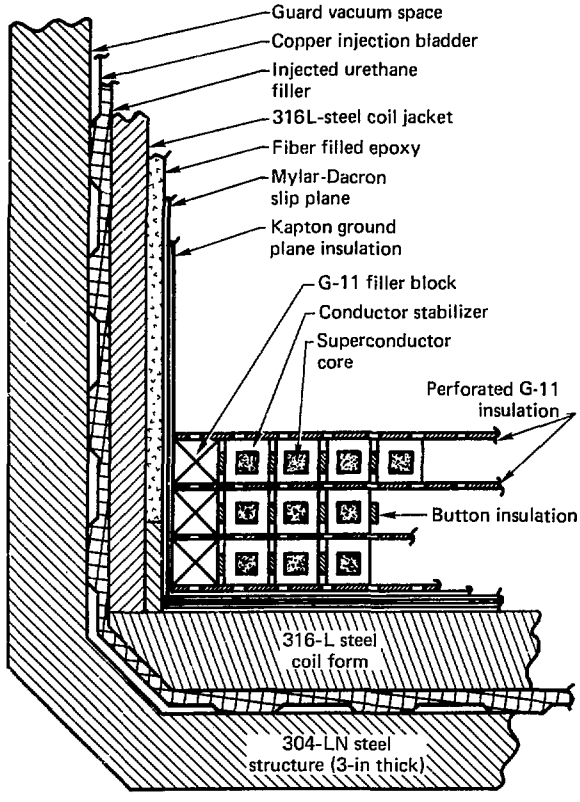

FIG. 3. Coil assembly detail.

assigned heat load for each model element. It was found that, with a magnet heat load of 350 W, the circulating helium flow is 700 g/s with less than 5% vapor volume at the top of the magnet.

Quench protection for the magnet is accomplished by conventional means using an external dump resistor and a 1,000-V discharge. The magnet time constant (see Table 4) is 69 s and an adiabatic conductor temperature rise of 200 K is calculated assuming a 10-s delay for the quench detection circuit to sense the quench condition and activate the circuit breakers to the power supply.

TABLE 4. Quench characteristics.

Characteristic	*Value*
Coil inductance, H	11.0
Mutual inductance, H	1.2
Peak voltage, V	1000
Quench time constant, s	69
Peak conductor temperature after 100 s, K	<200
Delay time, s	10
Propagation velocity, $m \cdot s^{-1}$	1.2
Quench resistor, Ω	0.17

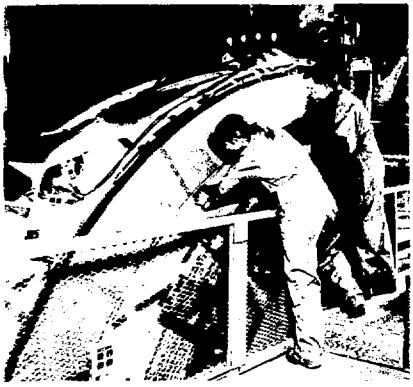

FIG. 4. Coil winding operation.

FIG. 6. First completed coil being removed from the winder for placement on the shim-bladder-assembly stand.

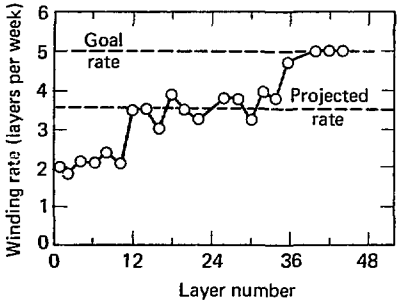

FIG. 5. Magnet winding rate. Rate does not include out-of-conductor time, but does include turnaround time and side glue blocks.

MAGNET STRUCTURE

No code or standard guidanee exists for the design of magnet structures. Instead, referenee was made to Sections III and VIII of the ASME Unfired Pressure Vessel Code. However, blind obedience to existing codes can result in either excessively heavy or dangerously fracture-prone structures. For example, paragraph UA-500 of the ASME Code recommends that 1/4 of the tensile strength or 5/8 of the yield strength be used for design stress, whichever is lower. For some stainless steels like 304, the design would be limited by yield strength and be excessively conservative, considering the very high tensile strength and toughness at low temperature. Also, Charpy impact tests at 77 K are not at all representative of the fracture toughness and crack-growth properties at 4 K, so that insufficient fracture resistance might result. Figure 7 shows a better relationship to compare fracture toughness and yield strength of several stainless steels.

Our criteria[9] for the design of the MFTF magnet are summarized in Table 5. Note that the percents of yield and tensile strength are higher than *those recommended in UA-500 for two reasons:* sophisticated electromagnetic computer codes accurately resolved the forces on the magnetic structure, and the environment is benign and noncorrosive. Because of the tendency of materials to embrittle at low temperatures, the design stress dependence upon fracture mechanics at 4.2 K was more restrictive. The plane-strain fracture toughness, K_{IC}, had to be compatible with the detectible flaw size, a. Equally important was the crack growth rate, da/dn, during cyclic loading conditions. MFTF was designed for a life of 2,000 stress cycles corresponding to a safety factor of four during the expected 10-year service life.

When the aforementioned general design criteria were applied to MFTF and materials properties evaluated, the specific structure-design criteria in Table 6 were adopted for the detailed

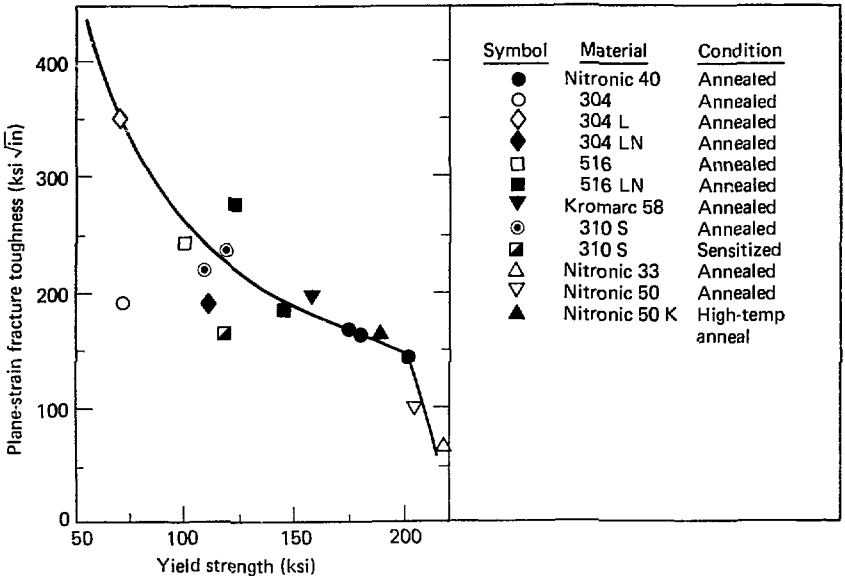

FIG. 7. Decline of fracture toughness with increasing yield strength.

stress analysis to be performed by General Dynamics, Convair Division.[10] A finite-element SAP IV computer analysis was performed and supported by various detailed calculations. In the peak stress region of the structure, three-dimensional elements in the NASTRAN code were used to refine the analysis, so that no calculated stress exceeded the 80 ksi criteria.

After a review of available material properties, 304LN stainless steel was chosen for the structure. Extrapolation of NBS data[11] indicated that the yield strength of 304LN would equal 120 ksi, if 0.14% nitrogen could be added, while the fracture toughness, K_{IC}, was expected to remain about 200 ksi$\sqrt{in.}$ Production of 800,000 lb of 304LN steel was successfully completed with the material passing all

TABLE 5. Design stress criteria for magnetic structure.[a]

Stress	Criteria
Design	2/3 yield strength[b]
Design	100% yield strength[c]
Design	1/2 tensile strength
Design	$1/2\, K_{IC}/\sqrt{\pi a}$
Design, cycles	4 lifetimes

[a] The lowest stress criterion is chosen from among those listed.
[b] Primarily tension and combined stresses.
[c] Primarily bending.

TABLE 6. Minimum structural materials properties.

Property	Value
Design stress, ksi	80
Yield stress, ksi	120
Ultimate stress, ksi	160
Elongation, %	20
Charpy impact at 77 K	
Absorbed energy, ft-lb	40
Lateral expansion, in.	0.030
Toughness (K_{IC}), ksi$\sqrt{in.}$	120

chemistry, microstructural, and ultrasonic inspections, and the steel was supplied for the coil structure fabrication shown in Fig. 8.

An extensive development program was necessary to achieve weld properties that would match those of the base metal. Because 316L weld metal promised to have good yield and ultimate strength, it was selected for development. Steel toughness was known to be influenced by ferrite content[12] (see Fig. 9), so very low ferrite content was necessary. However, below 3% ferrite, microfissuring of this weld metal becomes a problem. Several welding methods were attempted, but only shielded metal-arc welding produced an adequate combination of toughness, sufficient welding speed, and versatility.[13] Table 7 summarizes a few of the weld and base metal properties which qualified the coil structure manufacturing. Careful control of purity, ferrite level, and welding methods achieved the demanding requirements.

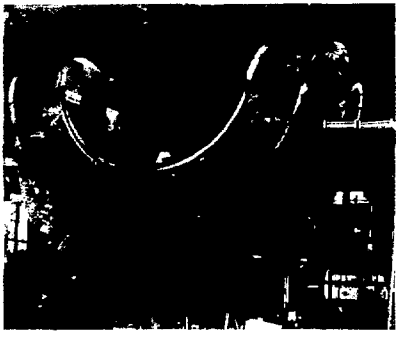

FIG. 8. Coil structure fabrication.

TABLE 7. MFTF structural material properties.[a]

	K_{IC}, ksi$\sqrt{in.}$	Yield strength, ksi	Ultimate strength, ksi	Reduction, area-%
316L-15 Weld	183	112.0	183.2	28.1
304LN Base material	202	111.6	237.4	36.0

[a]All measurements made at 4 K.

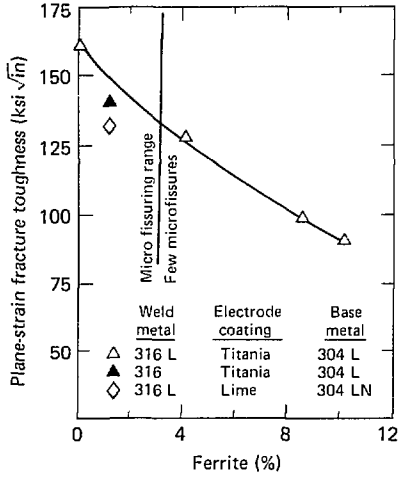

FIG. 9. Effect of ferrite content on weld toughness.

SECTION 2
SUPERCONDUCTOR MANUFACTURE

The MFTF conductor design was developed as part of the general magnet development work at LLNL.[5] Each U.S. manufacturer produced one billet of prototype core material and, based on the results of this work, a specification (MEL77-001373A) was prepared. After selecting a manufacturer (Intermagnetics General Corporation), the details of that manufacturer's design were incorporated into a modified specification (MEL77-001373C) which was used as a basis for the production order.

A copper sheath, shown in Fig. 10, was soldered to the core to provide additional cooling for cryostatic stability. This process was contracted to Airco.[14]

In this wraparound technique, the superconducting core is passed through a continuous electroplating process prior to applying the stabilizer. The latter is prepared from an oxygen-free high-conducting (OFHC) copper by first slitting and rolling a strip, followed by punching helium access holes. On a roll-forming line, the stabilizer is wrapped around the core, and the conductor is then sized by a Turk's-head. The completed conductor then passes through the soldering furnace, a quenching system, and a cleaning process before being wound onto the supply drum.

FIG. 10. MFTF superconducting core and copper sheath.

The choice of a monolith conductor presents several manufacturing and quality assurance problems not encountered with a cable or braid. In order to achieve optimum critical current in Nb-Ti, a large amount of cold work is required.[15] This cold-work requirement can be met for a cable or braid by starting with a billet of 150- to 200-mm diameter, because the braid strand size is typically 0.5 to 2.0 mm in diameter. The final size of the MFTF core is 6.5 mm by 6.5 mm; consequently, a large-diameter billet must be used, and the manufacturing risks are greater. In addition, the MFTF magnet requires continuous lengths of greater than 380 m; large-diameter billets are necessary to produce these lengths in an economical manner, and breakage during manufacture must be minimized.

The absence of redundancy in a monolith such as the MFTF superconductor requires that the quality assurance tests be especially rigorous. Consequently, samples from each end of each length are checked for critical current (I_c), matrix-resistivity ratio (R_{293K}/R_{10K}), copper-to-superconductor ratio, twist pitch, filament size, and filament integrity. A basic premise for the quality assurance of the MFTF superconductor is that samples from both ends of each length are sufficient to guarantee the quality of each length. Nb-Ti alloy in the composition range 46 ± 1.5 wt% Ti, balance Nb, was specified. The Nb-Ti alloy presented few problems and rejections were under 1%. Defects were mainly associated with surface quality, size, and straightness. Many of the surface quality rejections were discovered by the manufacturer to come from "fretting" (self-abrasion) of the material during transit. The solution was simply to pack such that relative motion between the rods was minimal. Ingot and product chemistry were always within specification. All copper used in the billets was either phosphorous-deoxidized oxygen-free

(PDOF) or OFHC brand with a guaranteed resistivity ratio of greater than 180:1.

Conductor fabrication followed a relatively standard sequence for all Nb-Ti superconducting composites.[16] The billets were assembled using hexagonal copper tubes in which cylindrical Nb-Ti rods were inserted. All elements were chemically cleaned and stored under dry nitrogen prior to assembly. The array was stacked to fit within a copper extrusion can which became the shell of the conductor. The billet was then capped with a nose and lid, evacuated, and sealed by electron-beam welding. Electron-beam welding was used to ensure reproducible welds.

The extrusion operation reduced the billet to a much smaller rod and metallurgically bonded the interfaces together to yield a true composite. The press capacity of 5000 tonne was almost fully utilized in the extrusion of the billet. An initial problem of tooling failure resulted in the misextrusion of several billets. The problem was remedied by the design of special tooling to fully utilize the press capacity.

The ends of the extruded rod were cropped and the rod was cut into two lengths. These rods were drawn through a series of dies using several draw benches.

After the rods were reduced to 20-mm diam, drawing was done on conventional bull blocks specially modified to handle the high tensile strengths of these conductors. An intermediate heat treatment was introduced during the drawing process to obtain the maximum superconductor properties. Few problems were noted in the drawing for sizes below 20 mm. The conductor was twisted and Turk's-headed by a special machine designed to rotate the pay-off spool. The final conductor sizing to a tolerance ±0.05 mm was done with a tungsten carbide die. A final annealing step was performed to restore high conductivity to the copper matrix.

QUALITY ASSURANCE

The various steps in the manufacture of the MFTF superconductor were reviewed from the standpoint of quality assurance, and a comprehensive plan was prepared. This plan specified the documentation required for each length of conductor and the method for verifying that each manufacturing step had been performed. A written discrepancy report was required for any condition or procedure which differed from the quality assurance plan. When manufacture was complete, samples from each end of each length were tested to see that the specifications were met. These results, together with any discrepancy reports filed during manufacture, were reported to a Materials Review Board which made the final decision on any out-of-specification material.

CRITICAL-CURRENT TESTS

A total of 350- to 400-critical-current measurements were anticipated and a test facility capable of handling this large number of samples was constructed. A superconducting solenoid with a 25-mm by 50-mm access produces a maximum transverse field of 8.5 T, and a regulated 12,000 A(dc) power supply provides current to the sample. The sample holder with helium-vapor-cooled leads can be changed while the solenoid is maintained at cryogenic temperatures. Three of these sample holders were constructed so that four samples can be tested in one day. Voltage taps spaced 25-mm apart were attached to the sample in the uniform field region, and a criterion of 10^{-11} Ω-cm resistivity (for the Nb-Ti area) is used to define critical current.

One problem encountered in testing large high-current specimens is that the self-field generated by the current in the specimen becomes significant. For the case of untwisted filaments, calculations indicated that the influence of self-field on the measured critical current would be small, due to this effect enhancing the field on one side of the sample but reducing the field on the other side. However, when the twist pitch (190 mm) of the filaments in the MFTF conductor is taken into account, the self-field acts to reduce the measured critical current by about 7%. Measurements of critical currents on identical samples in the twisted and untwisted condition verified this effect. However, I_c for the MFTF samples were typically 15 to 20% above the specification of 10,000 A at 7.5 T, so self-field effects have not created a problem in acceptance of samples. Another consideration for testing high-current samples is the current-transfer length: both the length necessary to transfer current from the sample holder to the sample and the length for redistribution of the current from the outer filaments to the inner filaments as the sample passes

from the low-field to the uniform high-field environment are important. Insufficient area for current transfer from sample holder to sample can result in heating. Insufficient length in the uniform field region on either side of the voltage taps can result in a voltage signal due to current transfer, rather than due to exceeding the critical current. The length in the first case can be obtained from Refs. 16 and 17. The second case is more difficult to calculate, so we determined it experimentally by placing voltage taps spaced 25-mm and 50-mm apart. As a result, we found that using a 610-mm-long sample with 100-mm-long solder joints at the ends and voltage taps spaced 25-mm apart would prevent current-transfer problems from occurring.

COPPER-TO-SUPERCONDUCTOR RATIO

The copper-to-superconductor ratio (Cu:S.C.) is required to be between 1.63 and 1.77. The choice of this range was based on considerations of stability, strength, and quality of cold-welded joints.[18] This parameter is determined by weighing a 100-mm length of core, dissolving the Cu matrix, and weighing the Nb-Ti filaments. The major variable affecting the Cu:S.C. ratio (assuming the current ratio is used in billet construction) is the amount of cropping done at the nose and end of the extruded rod. Initially, a number of lengths were found to be outside this specification. However, a master curve of ratio versus distance along the conductor length at final size has been developed, so that the amount of cropping necessary can be determined from the Cu:S.C. ratio at any point along the length.

MATRIX RESISTIVITY RATIO

The matrix resistivity ratio is specified to exceed a value of 150. This ratio is determined by measuring the resistance at 293 K and at 10 K; the 10 K value is obtained by lowering the sample and its thermometry through the temperature gradient above liquid helium. We mount up to six samples in a horizontal plane and connect them in series, so that six measurements can be made in each experiment. Only one length of MFTF core failed to meet the resistivity ratio specification. A review of the records indicated that this length has missed the final annealing step; after annealing, it met specification.

FILAMENT TWIST PITCH

The twist pitch requirement for mirror fusion magnets such as MFTF are not as stringent as for Tokamak magnets, since the mirror magnets are not exposed to rapidly varying fields. The twist pitch for the MFTF superconductor is dictated by the proposed charging rate and should be less than 100 cm. A specification for twist pitch was chosen as between 16.5 cm and 19.0 cm; this range is easily achieved in a conductor the size of MFTF without danger of the twisting operation causing filament breakage.

Samples were found with out-of-specification twist pitch at the early stages of conductor delivery. This problem was traced to a method of starting the twisting operation. The manufacturing procedure was changed to avoid this problem by performing the end-cropping operation after the twisting operation.

The only other problem involving twist pitch resulted from a malfunction in the twisting-squaring operation when a pin sheared in the twist machine drive. This resulted in a 12-m length having no twist and required that the entire length be rejected. This experience is one case in which sampling each end of each length was inadequate to guarantee the quality of the length; it was necessary to rely on manufacturing quality control to note the problem and to file a discrepancy report.

FILAMENT SIZE AND INTEGRITY

Since MFTF is a cryostable, steady-state magnet, filament size does not play an important role. However, filament uniformity and filament integrity are an important indication of good manufacturing practice. A specification of filament size between 0.18 mm and 0.23 mm was established for this conductor. Metallographic examination of sample cross sections indicated that lengths from billets prepared in the early stages of this program contained nonuniform filaments. A typical case encountered contains several filaments measuring 0.4 mm in diameter (the worst case identified showed

one filament measuring 0.8 mm by 0.4 mm). This condition can arise if a billet is not packed densely enough and can occur anywhere along a given length. This is the other instance in which we found a problem that can remain undetected in samples taken from each end of each length.

Subsequently, improved billet assembly procedures were introduced and these extreme ranges in filament sizes were reduced. This experience suggests that applications needing a close tolerance on filament size, e.g., those requiring intrinsic stability or low ac losses, should specify close tolerances on billet density.

Filament integrity was not anticipated to be a problem for the Nb-Ti core, since the filament size (0.2 mm) is rather large and the amount of cold work is moderate for Nb-Ti. However, routine examination after removal of the matrix revealed slip lines on the filaments and occasional breaks. The density of breaks, i.e., approximately one in a 2-cm length, suggested that broken filaments should not affect the short sample critical current, and the experimental measurements bore this out. The other concern was that broken filaments might affect the strength of the core, so a series of tensile measurements were made at 4.2 K. Again, there was no difference between samples with and without broken filaments. Consequently, lengths with up to 1% broken filaments in a 2-cm length have been accepted.

Analysis of the problem indicates that filament breakage occurs in the final sizing steps; filament breakage occurs only in the outer filaments where the deformation due to converting from a round to a square cross section is greatest. This problem can most probably be eliminated by the addition of an annealing step prior to final sizing or by changing the filament distribution. However, these corrective actions are not being attempted at this time, since the properties of the MFTF core still exceed specification and the manufacturing changes would result in considerable delays in conductor manufacuture.

A benefit of this quality assurance program has been significant improvements in manufacturing techniques: (1) better billet assembly procedures, (2) less reliance on outside rod drawing capabilities, (3) controlled rod-cropping procedures, and (4) careful monitoring of the manufacturing steps to ensure that each step is performed to all specifications.

SECTION 3
MECHANICAL BEHAVIOR OF CONDUCTOR WINDING

INTRODUCTION

The following is a summary of analytical and experimental studies into the mechanical behavior of the Mirror Fusion Test Facility (MFTF) magnet superconductor pack. The superconductor pack is here defined as the 24-turn by 58-layer coil with its interturn and interlayer insulation and any filler material between the superconductors and the coil jacket. The relative shapes and sizes of the MFTF conductor, structural case, and plasma fan are shown in Fig. 11. Mechanical behavior is defined as the stress and strain that the superconductor pack components experience during magnet winding and normal 2-T central field operation, as well as any anticipated conductor motion that impacts the internal design of the coil.

Mechanical properties of the coil components at 4 K are reviewed. This is followed by a description of the electromagnetic loads that the coil will experience, their method of calculation, and the redistribution of these loads due to structural compliance. Investigations of the possible buckling effects of superconductor pretension on the jacketed coil are also discussed.

Superconductor stress and strain analysis, performed by using a selected range of coil mechanical properties, are summarized, as are the possible effects of static and cyclical strain on the niobium-titanium superconductor and its copper stabilizer. Finally, an analytical prediction of superconductor motion is detailed, including a diagram of the expected superconductor pack displacement with respect to the coil jacket.

MECHANICAL PROPERTIES

The first step in modeling the mechanical behavior of the MFTF coil was to determine the physical properties of its components at 4 K. The MFTF superconductor pack may be thought of as a modified orthotropic composite that can carry only compressive loads in two directions and only tensile loads in the third direction. In addition, the properties in each direction are nonlinear and exhibit hysteresis in their stress-strain responses.

The MFTF superconductor core is a 0.25-in.-square copper-stabilized niobium-titanium composite consisting of 480 superconducting filaments in a copper matrix with a copper-to-superconductor ratio of 1.7.[19] An embossed and perforated copper wrap[20] is soldered around the core to provide heat transfer and mechanical support to the core. The final assembled conductor is 0.490-in. square.[21]

Tensile tests of the MFTF superconductor were performed in liquid helium to establish both the stress-strain response curves and the tensile failure loads.[22] Strain-gauged samples were used to obtain the stress-strain curves up to an elongation of 1% using foil gauges designed for use in liquid helium.[23] Figure 12 shows the stress-strain response of the wrapped superconductor at liquid helium temperature. Unload/reload cycles always followed hysteresis loops while loadings beyond the previous peak always followed the envelope curve until being unloaded.

The bare MFTF superconductor core was found to fail in tension at about 8200 lb, while the wrapped superconductor assembly was pulled to beyond 10,600 lb without tensile failure. The addition of a cold weld joint to the superconductor core reduced the failure load to 7100 lb, showing very little sensitivity to the number or length of cold welder strokes. The technique chosen for MFTF joints was five cold welder strokes at 1/2 in. per stroke. Annealing of the cold weld due to soldering of the copper stabilizer further reduced its strength to 5700 lb.

The cold-weld tensile tests showed a large spread in tensile failure values. The design requirement of high reliability placed on the magnet system meant that adequate joint strength must be guaranteed. This matter was resolved by the addition of a monolithic copper joint-reinforcement bar. Joint assembly verification tests showed that the copper-reinforced cold-weld joints can withstand three times the maximum anticipated axial load of 3000 lb and are stronger than the parent superconductor even when no cold weld is applied, thereby providing 100% joint strength redundancy.[24]

The coil pack is made up of the above superconductor in 58 layers of 24 turns each.[25] Interturn

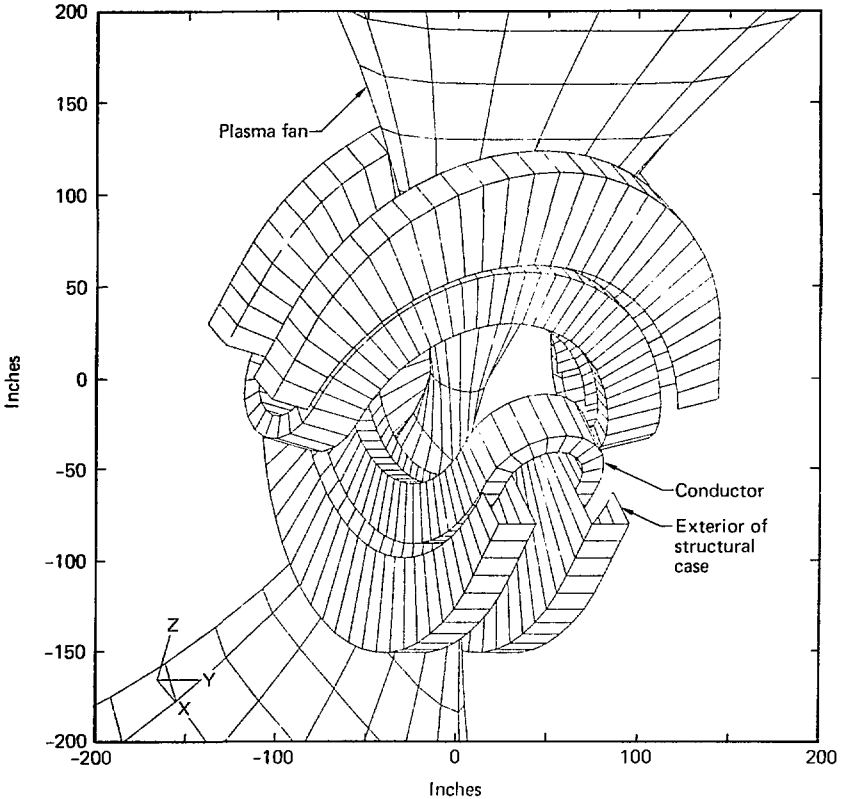

FIG. 11. Relative size and shape of MFTF conductor, structural case, and plasma fan.

insulation is composed of 0.045-in.-thick NEMA G-11 buttons glued to a woven string.[26] Interlayer insulation is 0.0625-in.-thick slotted NEMA G-11 sheets.[27]

The compressive response of the superconductor coil pack was measured at liquid nitrogen and room temperature using a coil pack mock-up.[28] This series of tests revealed a linear compressive modulus of 2.0×10^6 psi in the interturn (button) direction and 3.0×10^6 psi in the interlayer (slotted sheet) direction. Both response curves exhibited an early soft region followed by a stiff linear modulus. Figure 13 shows compression test data in the interlayer direction which illustrates this phenomenon. The initial nonlinear coil pack behavior is associated with the uneven surfaces of the pack components. If ideally "flat" mating surfaces are assumed, the early softness can be interpreted as a 0.005-in. gap per layer of superconductor.

Accumulated stack height measurements performed on the coil winder showed actual winding gaps to be less than 0.005 in. per layer per turn at all monitored stations on the coil.[29] Coil winding procedures such as tensioning at 600 lb, clamping, and coil-height measurements place an emphasis on obtaining a tight winding. This reduces the

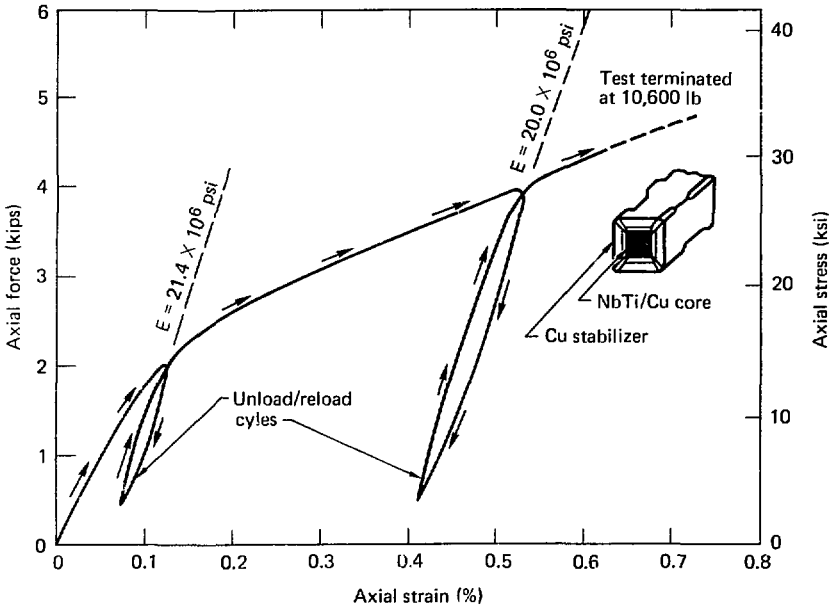

FIG. 12. MFTF superconductor tensile test done in liquid helium.

magnitude of coil pack motion during magnet energizing and de-energizing.

A plenum region is provided between the top of the 58th layer and the inside surface of the coil jacket for the collection of helium bubbles outside of the superconductor itself. The plenum filler material is composed of laminated sheets of slotted NEMA G-11. The laminated assembly was compression tested and found to be structurally sound to beyond 4000 psi.[22] Compressive strength was needed only during coil closure since the bubble plenum region experiences very small compressive loads during magnet operation.

The outside face of the 58-layer coil pack bears against a slip plane on the large radius of both magnets as shown in Fig. 14. The slip plane, consisting of two sheets of 0.007-in.-thick Mylar, allows relative motion between the superconductor pack and the surrounding coil jacket to occur without damaging the Kapton or NEMA G-11 insulation. Analysis of the slip-plane requirements found a coefficient of friction of 0.9 or less to be

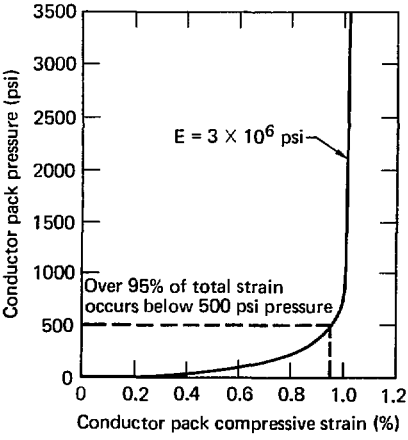

FIG. 13. Compaction of MFTF conductor pack interlayer (slotted G-11) direction at LN temperature.

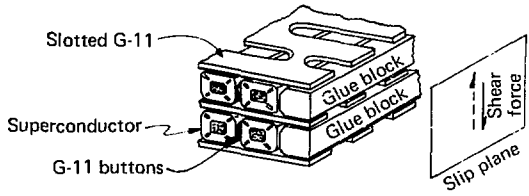

FIG. 14. Bearing face of MFTF superconductor pack.

satisfactory.[30] Laboratory tests on a slip-plane mockup showed a friction coefficient of 0.17 for the Mylar-on-Mylar configuration.[31,32]

Tests were also performed to verify the compressive strength of the filled epoxy used to grout the completed coil prior to applying the jacket.[33] This investigation included a thermal shock test using an embedded steel washer. No damaging effects due to differential thermal contraction were found.

The compressive load, at which the soft copper wrap on the superconductor begins to be permanently indented by interturn insulation, was found by testing to be 4500 psi.[34] The coining load in the interlayer direction is 5400 psi due to the larger effective contact area of the NEMA G-11 sheets. These compare favorably with the anticipated 3400-psi interturn and interlayer compaction pressures exerted during magnet operation at full field.[35]

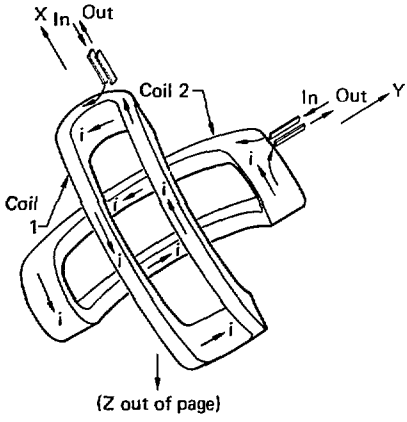

FIG. 15. MFTF magnet current direction.

ELECTROMAGNETIC LOADING

The MFTF yin-yang magnet geometry and the direction of current flow in each coil is illustrated in Fig. 15. As the diagram suggests, the large and small radii of the two coils behave somewhat like segments of solenoids. The peak magnetic field value of 7.68 T occurs on the inside surface of the coil pack in the small radius region, as seen in Fig. 16. The similarity to a solenoid diminishes, however, when the transition from large to small radius is considered (as shown in Fig. 17) where the transition region displays high gradients of electromagnetic forces.

Most of the electromagnetic load calculations for the MFTF yin-yang magnet were performed using the Electromagnetic Fields, Forces and Inductance (EFFI) computer program.[36–38] EFFI is capable of modeling an arbitrary system of coils made from circular arc and/or straight segments of rectangular cross-section conductors, and was used extensively in the analysis of the MFTF magnet.

The internal pressure exerted on the side walls of the coil jacket by the superconductors has been

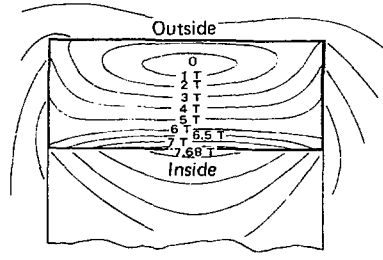

FIG. 16. MFTF magnet field distribution—minor radius symmetry plane.

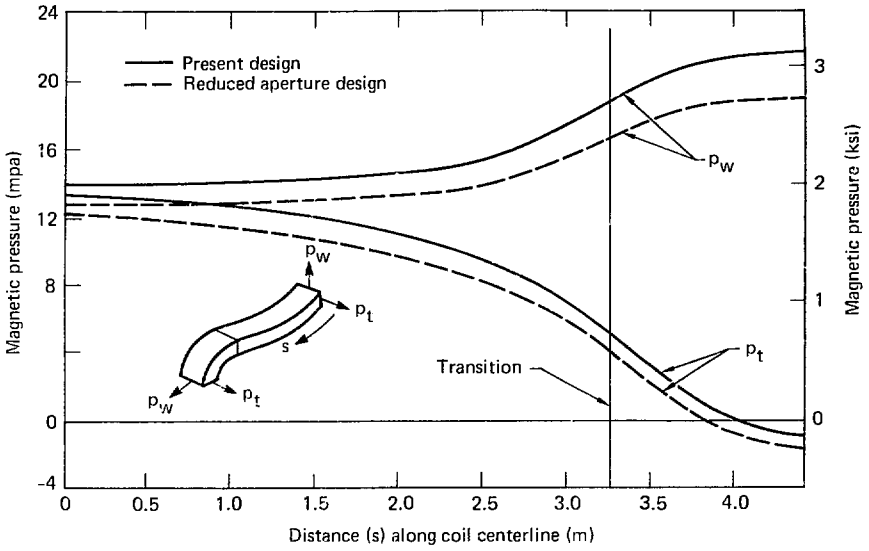

FIG. 17. MFTF magnet. Average magnetic pressure—EFFI calculation prior to redistribution.

calculated using an EFFI computer program model and the load redistribution extracted from integral coil/structure finite element models.[35] The analysis models built by General Dynamics/Convair used six rod elements to represent the coil pack. Transverse coil pack members with appropriate pack modulus properties transferred the applied loads to the structural case.[83] The finite element model is illustrated in Fig. 18.

Another way to illustrate the EFFI-generated loads in Fig. 17 is to use a coil sketch with applied load vectors, as Fig. 19 shows. These loads do not account for the effects of the structural case.[39] Due to the compliance of the supporting case and the motion of the coil pack with respect to the coil jacket, the electromagnetic pressure exerted on the surrounding material is lessened in the small radius region.[40] This effect can be seen by comparing Fig. 20 with Fig. 19.

The superconductor and copper bus lead-outs penetrate the coil jacket and structural case at the helium vapor exit pipe in the manner shown earlier in Fig. 15 and with the applied loads from Fig. 21. The lead support structure has been designed to withstand the maximum expected electromagnetic loads.[41] The geometry selected for the lead-out path allows coil pack motion to occur without jeopardizing the lead-out assembly, as dealt with in more detail later in this report.

COIL WINDING TIGHTNESS

As Fig. 14 shows, the MFTF coil pack is made up of alternate layers of superconductor and NEMA G-11 insulation. The tightness of the wound coil influences the superconductor pack motion and pressure load redistribution. The degree of pack tightness is quantitatively described as the stack-height buildup per layer of conductor above the sum of the individual component heights. This phenomenon is the result of surface features of the superconductor and NEMA G-11 which prevent continuous surface-to-surface contact.

When fictitious, perfectly flat surfaces are considered in analyses, the early reduced compressive stiffness shown in Fig. 13 is interpreted as an initial per-layer "gap." As a result, reference to the word

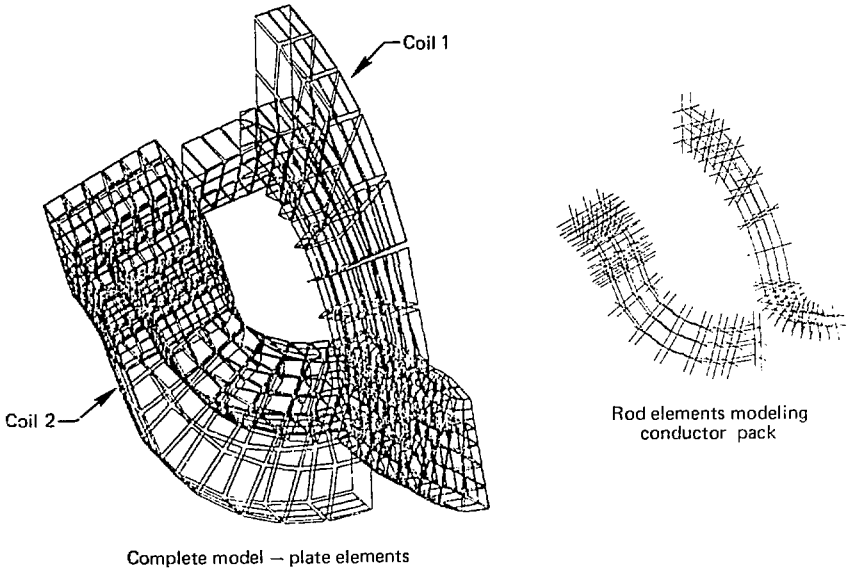

FIG. 18. MFTF—refined model.

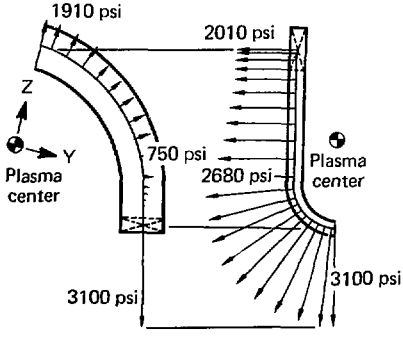

FIG. 19. MFTF electromagnetic loads at 2-T central field.

"gap" in the context of coil winding has come to represent this analog of a surface contact phenomenon.

Several methods were employed to maintain the tightness of the MFTF coil pack. The superconductor was continuously held at a tension of 600 lb during coil winding. Small-radius clamps helped retain superconductor pretension, and side clamps closed interturn gaps on the large radius of the coils. The clamping, tensioning, and compaction measuring techniques are described in the MFTF coil winding specificaton. The actual winding tightness, achieved with the tensioning and clamping scheme described above, was found from stack height measurements to be from 0 to 5 mils per conductor.

An intermediate effect of this pretensioning is the distortion or possible buckling of the jacketed coil during transfer to the structural case subassembly. An early analysis indicated that a potential problem existed and that further investigation was needed.[42] Interference between the jacketed coil

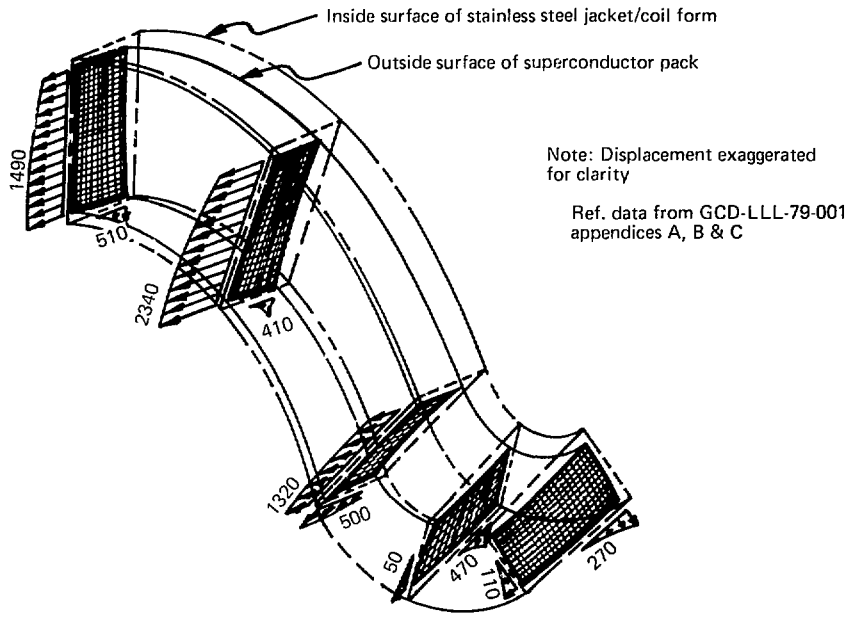

FIG. 20. MFTF average redistributed magnetic pressure (psi).

and the structural case due to coil distortion would result in assembly delays and possibly the design and fabrication of additional hardware.

A comprehensive buckling analysis was later performed by General Dynamics/Convair which took into account a conservative 50% relaxation of the winding pretension.[43] This analysis predicted that the jacketed coil would not buckle when the coil-form adapter strongback was removed. The analyses also predicted a displacement of about 0.9 in. at the large-radius symmetry plane which is within the allowable range for structural case assembly.

These, as well as earlier analyses, were very conservative and highly dependent on an accurate prediction of superconductor pretensile load retention. A program of strain measurement was undertaken to experimentally determine actual winding load on the coil form. Permanent strain gauges, meant to be read during magnet operation, were read during coil winding. Additional temporary coil-form strain gauges were applied to complement the permanent installations.[44] All of these gauges were also read during coil demounting and transfer. Preliminary results from these efforts confirmed the conservative nature of the analytical assumptions.

SUPERCONDUCTOR STRESS AND STRAIN

The analytical prediction of superconductor stress and strain in the MFTF magnet evolved from early hand analyses to sophisticated finite element analyses and parametric studies. Hand calculations were performed using simplifying assumptions such as no relative motion of conductors with respect to other conductors and the supporting case,[45] or of uniform stress or solenoid-like behavior.[24] When a relationship between superconductor winding tightness and strain was shown,[44] tests were initiated to determine the actual stress-strain response

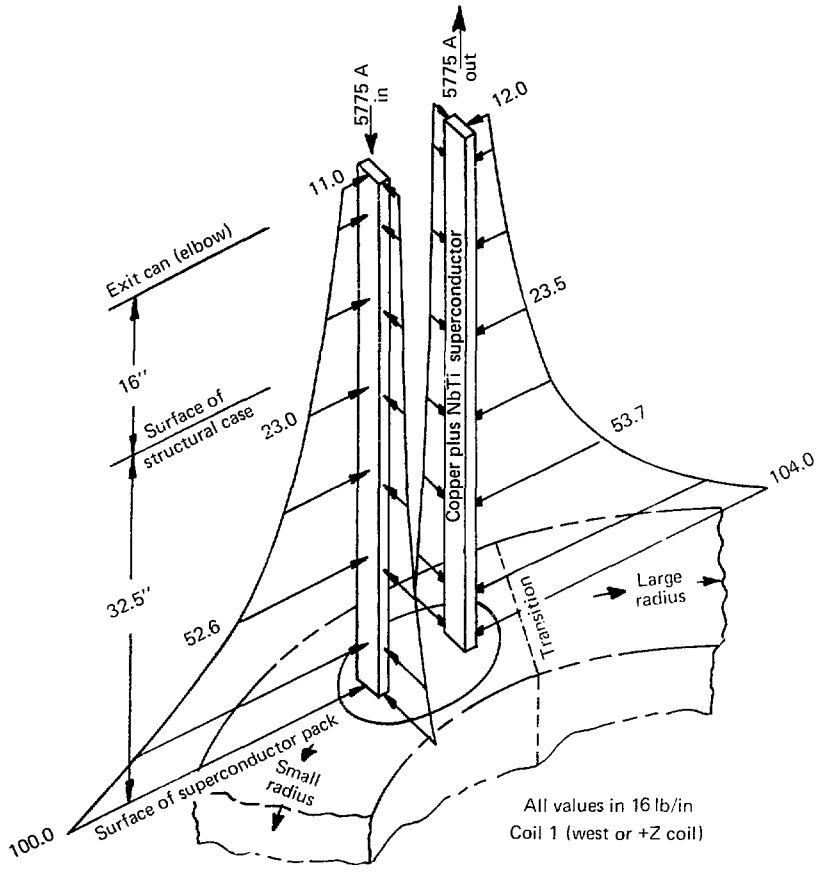

FIG. 21. Electromagnetic forces on MFTF superconductor leads.

of the wound coil pack for inclusion in analytical models.

The stress analysis of the MFTF magnet structural case[10,46] led to improved methods of predicting the effects of case deflection on superconductor strain.[44] This early work, however, did not address the effects of winding tightness and coil-pack motion which tend to redistribute stresses across the pack, as Fig. 22 shows.

The effects of winding tightness on conductor stress and strain were investigated by General Dynamics/Convair.[47] A parametric study was conducted to measure the degree of coupling between coil-pack modulus and conductor stress. Using three different simulated coil-pack moduli to address winding gaps of 0, 5, and 10 mils per conductor, it was found that although the coil motion increased with larger gap size, superconductor stress

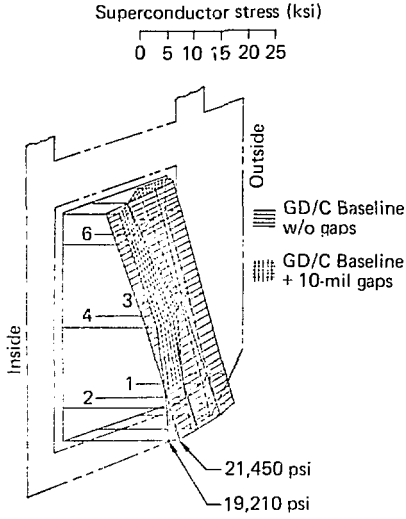

FIG. 22. MFTF superconductor stress distribution.

tended to redistribute itself with a slight reduction in the peak from a value of 22 ksi with no gaps to about 19 ksi with 10-mil gaps. Figure 22 graphically illustrates the change in superconductor stress distribution.

The analyses have indicated a new conductor stress of about 22 ksi when the magnet is at its maximum operating current of 5775 A. Due to nonlinear superconductor behavior and hysteresis, the superconductor strain can reach a peak of 0.25% during the first energizing. This number is reached by neglecting any radial support of the coil pack in the small radius. However, of this 0.25%, 0.15% is nonreversible permanent set and 0.10% is elastic strain with little variation in the hysteresis loop for subsequent load/unload cycles.

The wrapped superconductor and reinforced joint assemblies were successfully pulled in liquid helium to about three times the expected axial load levels. Of greater concern was the possible reduction in the critical-current value of the superconductor and degradation of the residual resistivity ratio of the copper stabilizer due to static and cyclical straining.

A comparison of MFTF operating strains with current literature on strain effects revealed no measurable degradation of the critical-current value for a peak strain of 0.25% or for repeated strainings to the same level, even to the point of fatigue failure of the specimen. A 3% reduction in the copper stabilizer residual resistivity ratio was predicted for a single strain of 0.25%. However, no further degradation could be found for subsequent cyclical straining to 0.10%.[48]

COIL PACK MOTION

Superconductor motion was considered when designing the internal components of the coil pack such as lead-outs, joint and ramp designs, slip planes, helium-bubble plenum details, and various fillers and supports. The motion of the MFTF coil pack with respect to the jacket and structural case was predicted by postprocessing finite element computer output provided by General Dynamics/Convair.[22,47] The diagram in Fig. 23 depicts the coil pack with exaggerated displacements to emphasize the directions of motion. Displacement value will vary due to actual as-wound conditions.

The slip plane previously discussed allows the magnet to safely accommodate several times the coil motion that is anticipated. An analysis of the design requirements of the slip plane depicted in Fig. 14 showed that a coefficient of friction of 0.9 or less would prevent damage to the slotted NEMA G-11 interlayer insulation. This was because 95% of the conductor motion occurs before 40% of the peak magnetic field is reached and when electromagnetic loads are relatively small. Tests of several slip-plane designs showed two sheets of 0.007-in.-thick Mylar to be more than adequate, with a coefficient of friction of 0.17 or less at cryogenic temperatures.

Conductor stress and motion analyses revealed that a reduction in normal load on the slip plane in the small radius and a more favorable mechanical environment for conductor lead-outs and coil diagnostics would occur if radial motion in the small radius was allowed. In the small radius region, General Dynamics/Convair analyses indicated a tendency of the conductor pack to self-support or lightly bear on the jacket wall if radial motion was not heavily restrained. As a result, the radial inside surface of the coil jacket in the small radius was designed to include a layer of highly compliant felt padding in addition to the Mylar-on-Mylar slip plane. This reduced or eliminated damaging radial loads in the end regions where internal anomalies

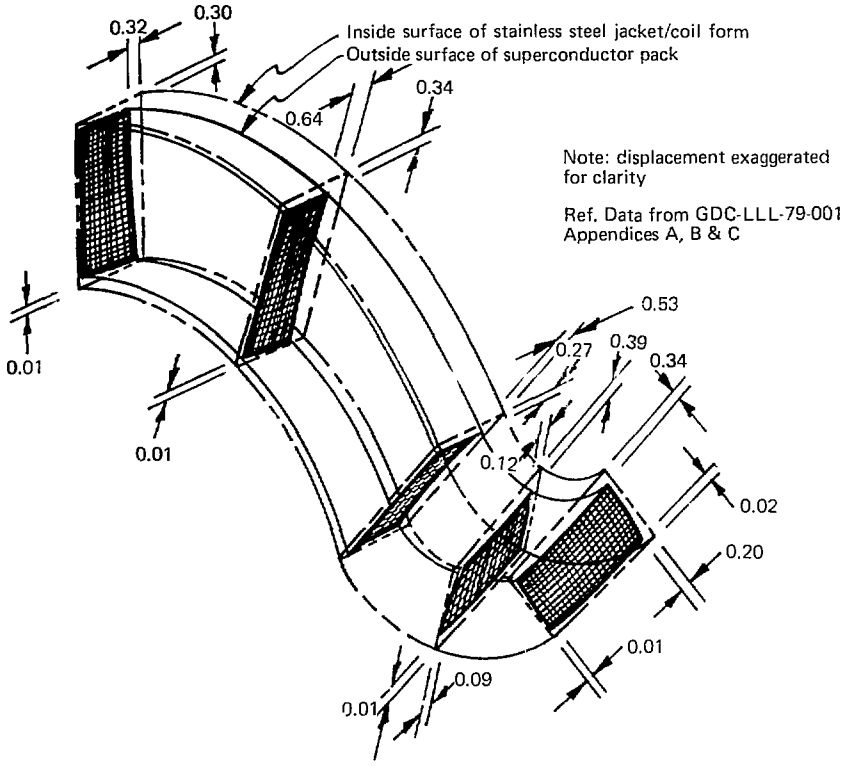

FIG. 23. MFTF average superconductor pack motion (inches).

such as lead-outs and permanent clamps must be installed.

Predicted coil motion also impacted the design of penetrations in the NEMA G-11 sheets where the superconductor must ramp up from one layer to the next. The possibility of a short circuit due to relative motion of adjacent layers was eliminated by surrounding the conductor penetrations with NEMA G-11 blocks. This arrangement safely allows over 3/8 in. of relative interlayer motion, 30 to 40 times the amount that is predicted by idealized analyses. Large excursions could occur if layers were to seize rather than slip. Even though this is highly unlikely, the conservative penetration design allows for these movements.

Several other details of coil internal design were influenced by predicted coil motion. Superconductor strain-gauge leads were routed and strain-relieved to allow for motion of the gauged region. Interturn button insulation was glued to a woven string and slots in the interlayer sheets were made too small for the buttons to pass through, in order to mechanically trap the buttons if they are scoured off of the superconductor. Coil lead-outs were positioned to allow coil pack motion to occur without mechanically loading the lead assemblies.

Glue blocks on the outer edge of the interlayer insulation provide a flat machined surface for slip-plane motion.

The MFTF coil pack mechanical behavior may best be summarized by two statements: Much effort was put into winding tight coils to minimize the coil pack motion that was predicted by analyses. Given the directions and relative magnitudes of the expected motion, coil internal details were designed to allow for several times the anticipated loads and motion without compromising magnet performance.

SECTION 4
COIL WINDING

INTRODUCTION

This section describes the basic criteria used in the winding of the MFTF yin-yang magnets. It also covers the equipment, special tooling, and materials necessary for the winding and enclosure of the coil in a 0.5-in.-thick stainless-steel jacket.

COIL GEOMETRY

The yin-yang magnet consists of two C-shaped coils that are enclosed in a structural case and attached roughly in the shape of a ball. Figure 24 depicts the geometry of one coil and Table 8 lists coil dimensions.

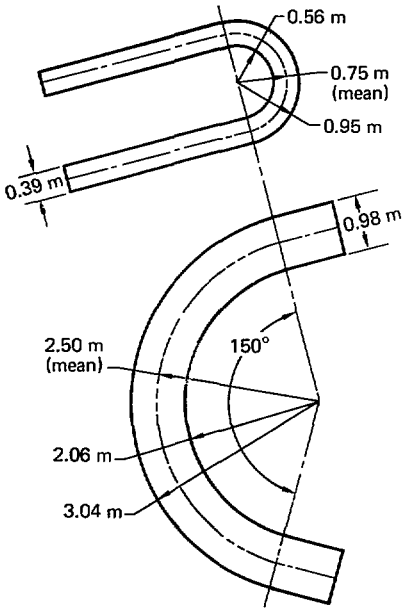

FIG. 24. MFTF coil geometry outline.

TABLE 8. C-coil dimensions.

Parameter	Value	
	Meters	Inches
Major radius	2.50	98.45
Minor radius	0.75	29.53
Cross section		
Height	0.98	38.58
Width	0.39	15.35

The coil is wound in pancake construction with superconducting conductor. There are 58 layers of 24 turns giving a total of 1,392 conductor turns.

The total length of superconductor used in each coil is 25,000 m (82,000 ft). A grand total of 50,000 m (164,000 ft or 31 mi) of superconductor is required to wind the pair of coils.

COIL WINDING EQUIPMENT

Before the MFTF coils could be wound it was necessary to design and develop the equipment required. The initial concepts provided by A. R. Harvey were based on experience winding the baseball coils and other similar coils. These concepts were pursued by R. C. Ling, R. E. Hinkle, and EG&G designers. The winding machine, reel support, conductor spools, button dispenser, and cold-welding process were the first to be developed.

MFTF Coil Winding Machine

The coil winder design was started in August 1976 and the initial design specification[49] was released in September 1976. Constructed by Teledyne Readco, York, PA, the winder in Fig. 25 was delivered to LLNL in September 1977.

The coil winder was designed with maximum versatility to allow for future changes in the coil geometry. It is capable of winding a two-axis coil with a major radius from 60 in. (1.5 m) to 130 in. (3.3 m) with 360° of rotation. The minor radius can vary from 12 in. (0.3 m) to 60 in. (1.5 m).

The design characteristics[50] of the coil winder are given in Table 9.

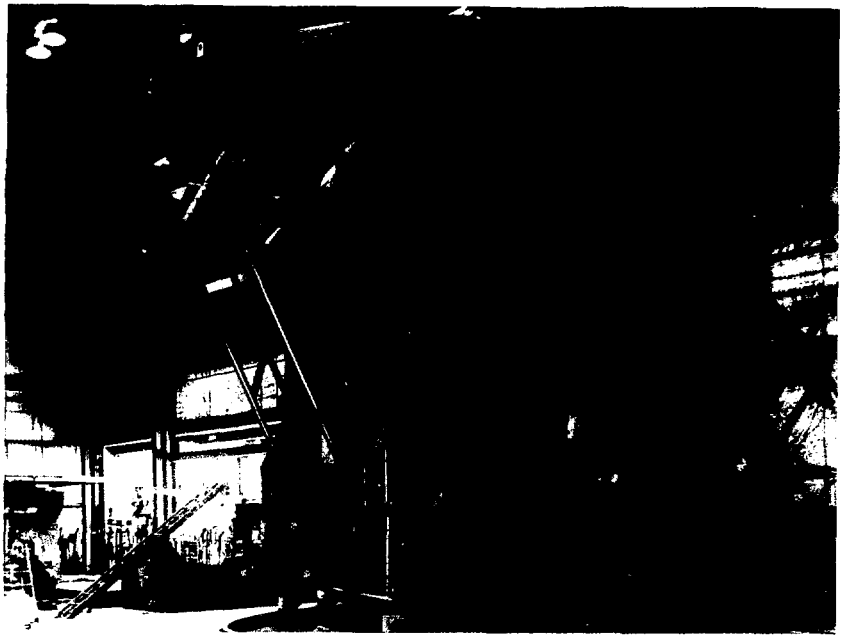

FIG. 25. MFTF coil winding machine.

Reel Support

The reel support (Fig. 26) was designed by EG&G designers under the direction of R. C. Ling[51] and fabricated by Hopper Manufacturing, Bakersfield, CA.

The reel support provides two basic functions. One is to support the 11-ft reel of superconductor during winding. The other is to provide constant tension for the conductor between 50 and 1,000 lb. A counter-balanced weight system is coupled to a torque motor with a center sending device that applies more or less torque to the reel to keep it balanced with the weights. This system was tested with a dynamometer and strain gauges and found to be accurate within ±50 lb. The entire upper assembly that supports the reel is floated on air bearings to provide a friction-free motion, and is capable of being elevated and pivoted to keep the conductor in an ideal winding position.

Other design characteristics[52] for the reel support are given in Table 10.

Button Dispenser

The button dispenser was initially designed and developed by the LLNL coil shop to apply the interturn insulation buttons to the MFTF test coil. It was redesigned by EG&G for MFTF winding and later modified by the winding technicians.

The dispenser (Fig. 27) was designed to apply the interturn insulation (buttons) to the conductor's side continuously while the conductor is being wound onto the coil form. The basic principle is to apply one drop of Loctite #414 super glue to each button, rotate the button, and hold it tightly against the conductor for a second while the glue sets. Loctite #414 was selected after extensive testing.[53]

Cold Welder

Figure 28 shows the cold-welding process adapted for the MFTF conductor after use on the MFTF test coil.[54] Purchased from the Heintz division of the Kelsey Hayes Co., Philadephia, PA, the

TABLE 9. MFTF magnet winder characteristics.

Parameter	Value
Design load, lb	172×10^3
Design torque, in.-lb	6×10^6
Operating torque:	
No load, in.-lb	5.2×10^6
Full load, in.-lb	5.1×10^6
Rotation:	
CW and CCW, both azimuth and elevation axes	Continuous
Drive speed:	
Azimuth axis, max., rpm	0.75
Elevation axis, rpm	0.20
Operating temperature, °F	32 to 110
Design life, yr	5
Survival seismic load, g	0.25
Power: 480 V, 3 phase, 60 Hz, 150 kW:	
Elevation drive, A	150
Azimuth drive, A	100
Dimensions:	
Height:	
No load, ft	23.17
With load, ft	30
Diameter:	
Service platform, ft	32
Base, ft	21
Weight:	
No load, lb	350×10^3
With load, lb	522×10^3

TABLE 10. Reel support characteristics.

Parameter	Value
Design load, lb	12,000
Design tension, lb	600
Verticle travel, ft	4.5
Verticle speed, in. · min^{-1}	3.6
Pivot travel, deg	±7.2
Pivot speed, deg · min^{-1}	2.4
Reel drive: bidirectional	Continuous-duty ac torque motor
Operating temperature, °F	32 to 110
Operating humidity, %	12 to 95
Operating life, yr	5
Seismic load, g	0.25
Dimensions:	
Length, ft	10
Width, ft	10
Height, ft	30
Weight: without reel, lb	21,000
Reel size:	
o.d., ft	11.17
Width, ft	2.33
Hub diameter, ft	10.5
Reel weight: with 9,000 ft of superconductor, lb	11,500

welder hydraulically presses the two ends of conductor together, causing a cold flow and molecular bonding of the copper. The Nb-Ti strands do not bond, but do intermesh. The resulting joint is stronger than copper, but not as strong as the composite.

TOOLING

Auxiliary tooling encompassed three major areas, adaptors for mounting the coil to the winder, clamping systems to maintain conductor tightness, and the miscellaneous tooling required for coil finishing. Where possible, initial designs and concepts were fabricated and tried during the construction of the MFTF test coil.

Adaptors

The need for two adaptors was apparent from the onset of the design: one for holding the coil form while winding and one for mounting the coil-form adaptor to the coil winder. Figure 25 shows the coil-form-to-coil-winder adaptor in place on the winder. This was designed at LLNL in conjunction with Teledyne Readco[55] during the winder construction.

The coil-mounting adaptor was designed by EG&G[56] and constructed by FMC Corporation, San Jose, CA, along with the coil form. The design was to support a dead weight of 60 tons and a winding torque of 5,000 ft-lb with a safety factor of 2.5. It had to be easily removable so that minimum strain would be placed on the finished coil during disassembly.

Clamping Systems

The need for quick-acting movable clamps for winding, and permanently fixed clamps for holding a layer after winding, was evident from experience with the baseball coil and the MFTF test coil.

The clamps were reduced to two types, end clamps[57] and side clamps.[58,59] Four end clamps, shown in Fig. 29, are mounted on each end of the

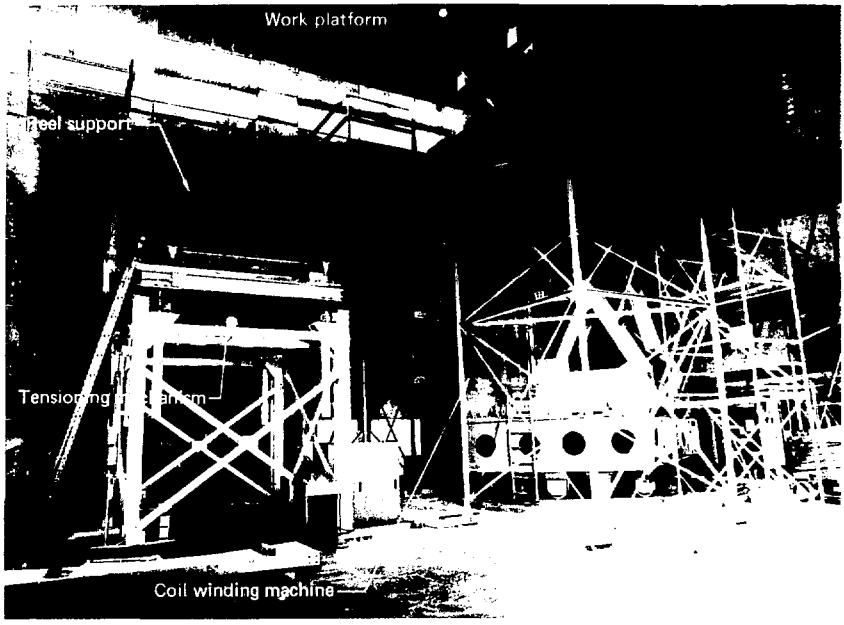

FIG. 26. MFTF reel support.

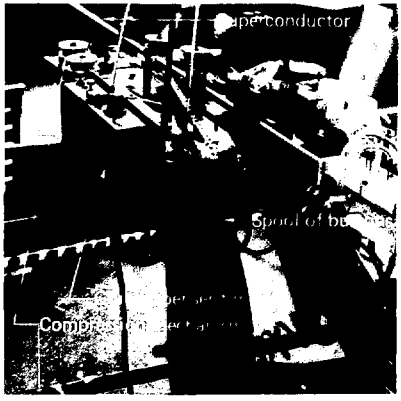

FIG. 27. MFTF winding button dispenser.

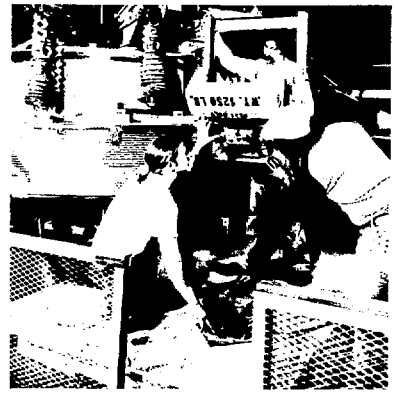

FIG. 28. Cold-welding process.

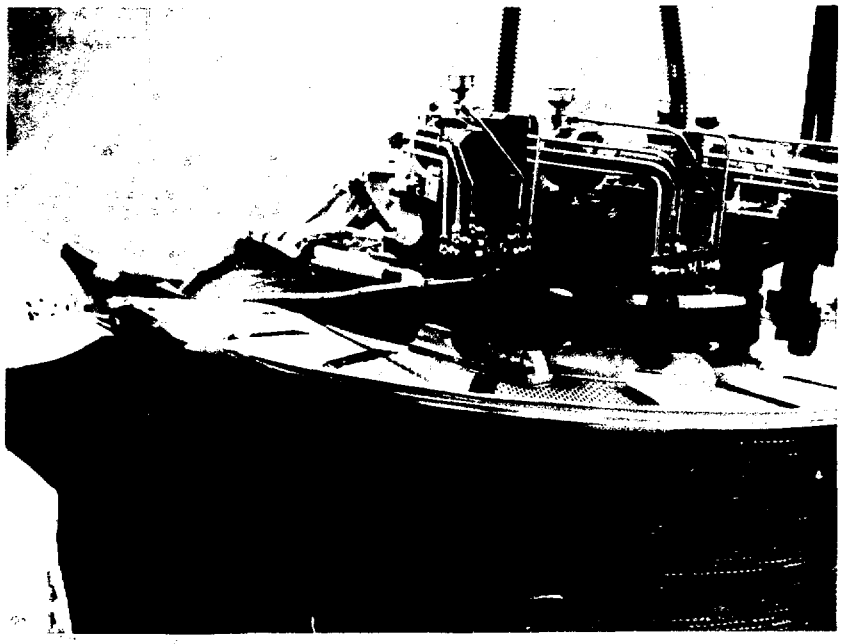

FIG. 29. End winding clamps.

coil-mounting adapter. Each clamp is pneumatically operated and capable of being swung out of the way. Each exerts an axial downward thrust of 1,500 to 2,500 lb.[60]

There are five sets of side clamps (see Fig. 30) on each side of the large radius of the coil form. They use a screw thread with a quick acting spring detent to produce fast lateral movement and telescope for verticle movement. The side clamps are designed to exert a lateral force of 500 lb[61] to hold each turn in position during the winding. Upon completion of the layer, the clamps are reset to hold the first turn of the next layer. To hold the previous layer in place fixed clamps were required.

The tower clamps shown in Fig. 31 were designed and constructed by EG&G to support the sides of the windings. They are stackable 1-in.-thick plates capable of exerting 500 lb of force in two places by the use of set screws.

Permanent end clamps in Fig. 32 were designed[62] to replace the end winding clamps. They are 1/2-in.-thick, 316L stainless-steel plates, held in place by 1/2-in.-diam bolts on the outside and by 3/8-in.-diam bolts on the inside. The inside bolts are part of the weld-backing bar. The entire system of bolts is torqued to 40 ft-lb each to replace the accumulated 6,000 lb of end-clamping force.

Tooling tables were designed and constructed by EG&G to provide a stable support for the tower clamps and side clamps. This can be seen in Fig. 30.

Miscellaneous tooling covers items that have been developed by the winding technicians and LLNL design team. The major item is the routing fixture (Fig. 33). It is constructed from two sets of linear ball bushings and shafts that are mounted to the coil form to support an air-operated router.[63] The prime purpose of this tool is to machine a smooth surface on the side of the NEMA G-11 filler blocks. This machined surface is further sanded to become a smooth load-bearing surface that transmits the electromagnet forces to the slip plane and subsequently to the structural steel case.

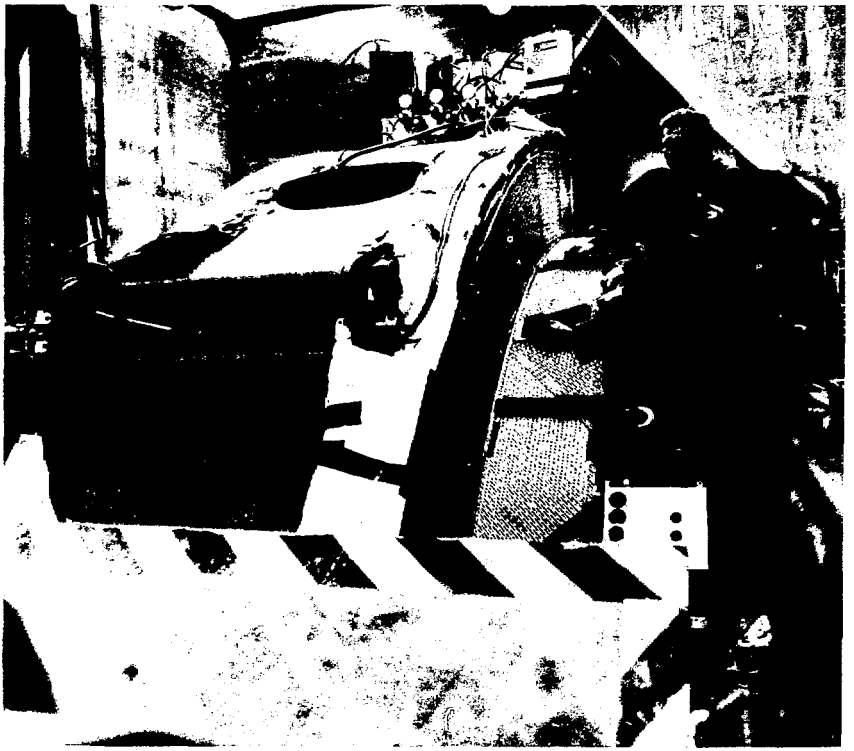

FIG. 30. Side winding clamps.

INSULATION

The insulation materials have been successfully used in previous coils. No new or unusual materials have been needed to meet the MFTF magnet insulating requirements in Table 11.

TABLE 11. MFTF magnet voltages.

Magnet area	Voltage
Ground plane, V(dc)	1000
Layer-to-layer, V(dc)	17.3
Turn-to-turn, V(dc)	0.7

The biggest insulation problem is to prevent arcing in gaseous helium as predicted by the Paschen curve in Fig. 34 for helium at 20°C and 1 atm.

Interturn Insulation (Buttons)

The design of the interturn insulation was taken from the Baseball II coil with improvements. The insulation must be capable of bending in two directions to conform to the coil geometry; it must also leave space for the liquid helium to circulate. The button approach that was developed for the Baseball II coil depended upon the glue bond to keep the buttons spaced along the conductor. The improved version (Fig. 35) added a Dacron string attached to the buttons for spacing.

FIG. 31. Tower clamps.

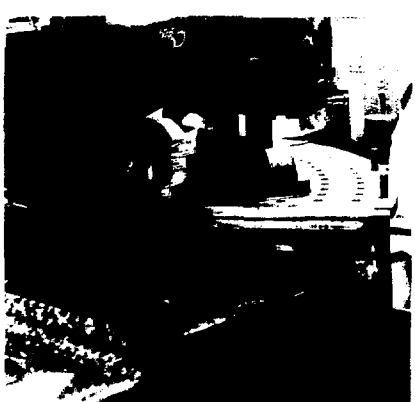

FIG. 32. Permanent end clamps.

The button is an octagonally shaped 0.040-in.-thick piece of NEMA G-11 with a groove in the center. Since the breakdown voltage[64] on the NEMA G-11 is 700 V·mil^{-3} at room temperature the interturn insulation requirements were easily met.

Because of poor vender performance LLNL was forced to undertake the job of designing the machine to produce the buttons at the rate of at least 1,500 ft/day. R. Leber (MFED) was responsible for the success of this task. The MFTF winding technicians now produce the interturn buttons on three machines in accordance with the manufacturing process as outlined:

Sheet Material. Sheet material of NEMA G-11 is procured by LLNL and surfaced to maintain a uniform 0.040 in. with a 0.002-in. flatness.

Strips. The sheets are sent to a second vendor to be sheared into strips 0.437-in. wide. A groove

FIG. 33. Router guide assembly.

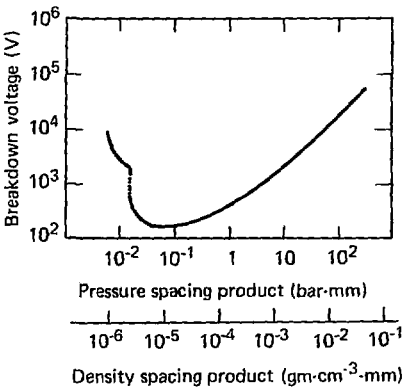

FIG. 34. Paschen curve for helium (20°C).

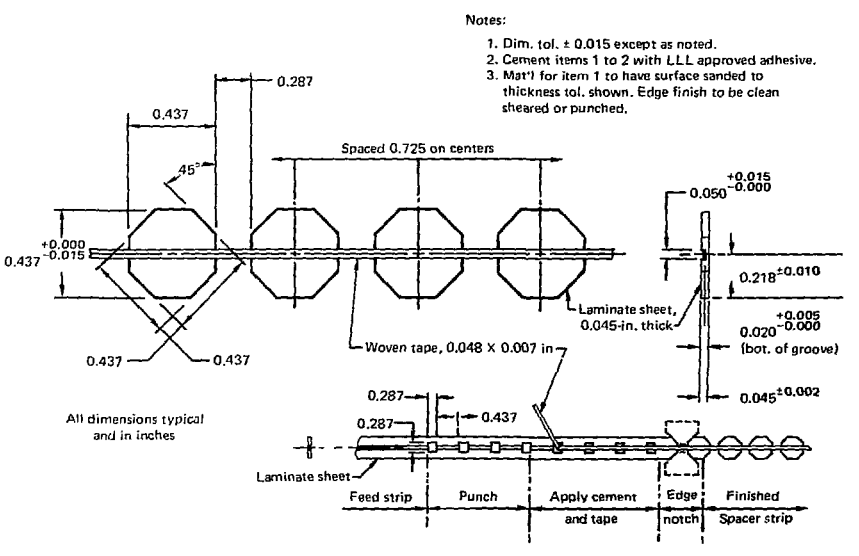

FIG. 35. MX coil interturn space strip.

0.050-in. wide and 0.025-in. deep is milled in the exact center of each strip, and the strips are sent to LLNL.

Square Punching. The strips are inspected for thickness and groove depth and then run through the machine in Fig. 36 to punch a square hole in an evenly spaced pattern.

Applying the String. The punched strips are fed into the string machine (Fig. 37) which feeds Dacron string into the milled groove and applies a single drop of Loctite #414 glue[53] to the joint. This newly formed ribbon of punched strips is wound onto a plastic spool.

Button Punching. The square-punched ribbon is run through a second punching operation which removes the remainder of the square hole and chamfers the edges of the remaining center piece. What remains is an octagonal-shaped button glued to the string. This is respooled onto a 400-ft-capacity spool with a ribbon of Mylar between each layer of buttons to prevent them from twisting. Figure 38 shows the button punch with some loose buttons being refastened to the string.

Interlayer Insulation

The interlayer insulation (Fig. 30) is fabricated in 36-in.-wide by 48-in.-long sheets 1/16-in. thick. LLNL drawing No. AAA78-110166 depicts the geometry of the perforations. Nominally the material is punched with a 3/16-in. wide × 1.5-in. long slot spaced 3/16-in. apart.

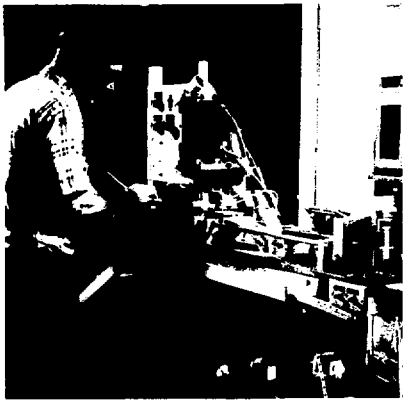

FIG. 36. Square-punching machine.

These sheets are sand blasted at LLNL and then cut to fit the coil form in such a manner that the slots are 45° off the vertical centerline of the conductor.

Ground Plane Insulation

The material selected for the ground plane insulation is Kapton. It was selected because of its excellent breakdown voltages of 3,600 $V \cdot mil^{-1}$ at room temperature, which increases to 10,800 $V \cdot mil^{-1}$ at −195°C.[65] Table 12 shows the mechanical properties of Kapton.

The Kapton is applied to the coil form in 2- and 4-in.-wide strips (see Fig. 39). Each strip is bonded with 3M #714 glue and placed so it overlaps the previous one by 50%. A second layer is placed over the first in the same manner with the overlapping being 50%. This process is continued for five layers to produce a type of baffled pathway that is at least 2-in. long for protection from arcing to ground.

Kapton exhibits an additional characteristic of being able to withstand 400°C which gives additional protection from damage during closure welding.

Plenum Chamber

When the magnet is operating the liquid helium coolant has bubbles of gas for which a path of escape must be provided. To accommodate the gas bubbles, 3 in. of space was left between the last layer of conductor and the coil jacket. It is this space that is referred to as the plenum chamber.

The 3-in. space has to be filled with a porous material that is capable of transmitting loads from the conductor pack to the jacket. The material selected was the interlayer insulating material previously described. The orientation of the perforations was studied to determine an optimum path for the bubbles. The selected scheme was to bond four sheets together with the perforations in line. These then were bonded to four sheets of similar construction except that the perforations were rotated 45–90°. This scheme of four sheets one way and then four the other was continued until the entire space was filled.

Slip Plane

The conductor motion analysis[22] shows that the conductor is going to compress until all the winding gaps are closed and then move out towards

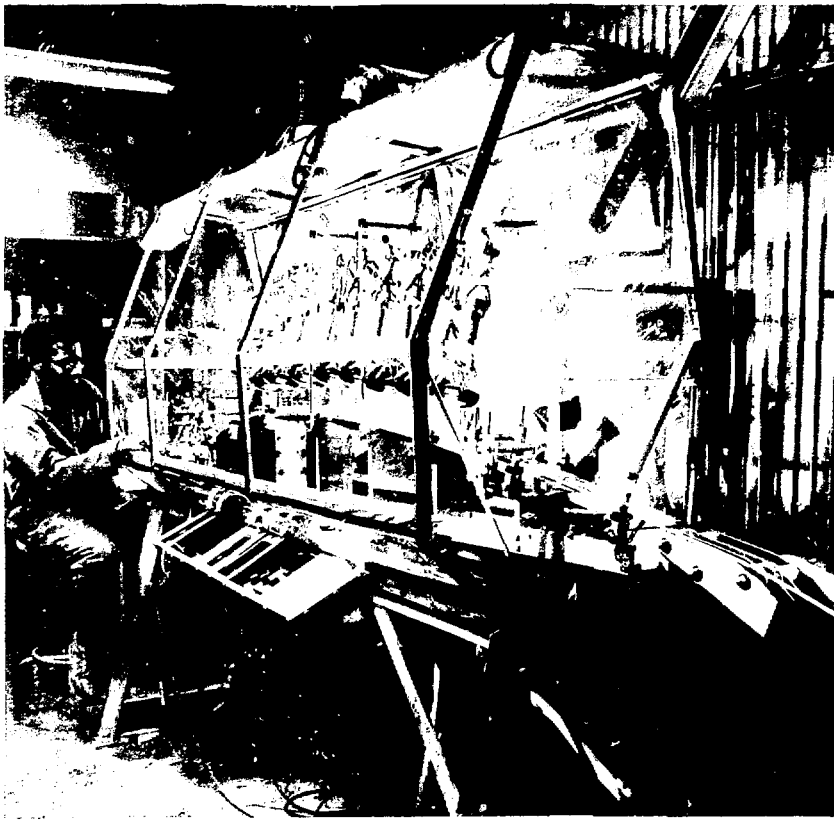

FIG. 37. String-application machine.

the 1/2-in. jacket. To accommodate this motion a slip plane has been provided to reduce the coefficient of friction and provide a sacrificial layer of material if local deformations are excessive.

Samples were produced that duplicated the edge construction of the NEMA G-11 glue blocks and tested in a special fixture at both room and liquid nitrogen temperature. They were placed against sample slip planes and loaded with a controlled force while a measured force was applied to start the materials slipping. Table 13 is a summary of the test results.

The Mylar-on-Mylar system was selected because it did not exhibit stick-slip behavior and avoided the uncertainties of the addition of the moly-disulfide power into the system.

Glue Blocks and Filler Blocks

The material selected to fill the inside of the coil from the conductor to the slip plane is NEMA G-11.

Glue Blocks. The glue blocks (Fig. 33) are fabricated with 1/2-in.-wide × 1/32-in.-thick × 40-in.-long strips of NEMA G-11. Each strip is

bonded, on a curved form, to the next strip using Epoxy 815 and versimide hardner. These strips are built up to approximately 0.45-in. thick.

The inside edges of the completed blocks are chamfered approximately 1/8-in. wide by 1/8-in. deep, and grooves are cut every inch to provide cooling along the surface of the conductor.

Once a glue block is bonded to the interlayer insulation it will provide 500 lb-in.$^{-1}$ of support, in shear, to hold the layer tight against the coil form. Once these permanent side clamps are installed they can hold the conductor in place and the Tower clamps are removed.

Filler Blocks. The filler blocks are of a similar design except they are machined to fit the outside of the conductor pack at the small radius. They provide a solid filler between the conductor and the jacket.

Felt Filler. To provide for the conductor pack motion previously discussed, it is necessary to allow

FIG. 38. Button-making machine.

FIG. 39. Coil form No. 1 ground plane installation.

TABLE 12. Properties of Kapton-type H.[75]

Property	Typical values, 1 mil film			Test method
	−195°C	25°C	200°C	
Physical				
Ultimate tensile strength, psi[a]	35,000	25,000	17,000	ASTM D-882-64T
Yield point, psi at 3%[a]		10,000	6,000	ASTM D-882-64T
Stress to produce 5% elongation, psi[a]		13,000	8,500	ASTM D-882-64T
Ultimate elongation, %[a]	2	70	90	ASTM D-882-64T
Tensile modulus, psi[a]	510,000	430,000	260,000	ASTM D-882-64T
Impact strength, $Kg \cdot cm \cdot mil^{-1}$		6		Pneumatic inpact test[b]
Folding endurance, cycles[c]		10,000		ASTM D-2176-63T
Tear strength-propagating, $g \cdot mil^{-1}$[d]		8		ASTM D-1922-61T
Tear strength-initial, $g \cdot mil^{-1}$[e]		510		ASTM D-1004-61
Tear strength-initial, $lb \cdot in^{-1}$[e]		1100		ASTM D-1004-61
Bursting test, psi[f]		75		ASTM D-774-63T
Density, $g \cdot cm^{-3}$		1.42		ASTM D-1505-63T
Kinetic coefficient of friction (film-to-film)		0.42		ASTM D-1894-63
Refractive index[g]		1.78		Encyclopedic dictionary of Physics, Vol. 1

		Test condition	
Thermal			
Melting point	None		
Zero-strength temperature, °C	815	20 psi load for 5 s	Hot bar[b]
Cut-through temperature, °C	435	1 mil *2 to 5 mil*	Weighted probe on *heated film*[b]
Coefficient of thermal expansion, in./in./°C	2.0×10^{-5}	−14 to +38°C	ASTM D-696-44
Coefficient of thermal conductivity, $Cal \cdot cm \cdot cm^{-2} \cdot s \cdot °C$	3.72×10^{-4}	25°C	Model TC-1000 twin heatmeter
	3.89×10^{-4}	75°C	
	4.26×10^{-4}	200°C	
	4.51×10^{-4}	300°C	
Flammability	Self extinguishing when flame is removed		
Heat sealable	No		
Specific heat, $cal \cdot gm^{-1} \cdot °C$	0.261	40°C	Differential calorimetry

	250°C	275°C	300°C	400°C		
Shrinkage, %	0.3		0.5	3.0	30 min	ASTM D-1204
Heat aging (in air)	8 yr	1 yr	3 mo	12 h	Circulating air oven	Time to reach 1% elongation

[a]MD
[b]Dupont
[c]MIT
[d]Elmendorf
[e]Graves
[f]Mullen
[g]Becke line

TABLE 13. Coefficient of static friction test summary.

Material	Room temperature	LN temperature
G-11 on G-11	0.3 to 0.35	0.3 to 0.35
Mylar/moly/Mylar	0.13 to 0.16	0.13 to 0.16[a]
Mylar-on-Mylar	0.13 to 0.16	0.13 to 0.16

[a]Coefficient of sliding friction dropped to 0.99 with moly coating.

the conductor at the small radius to move radially outward. This motion is permitted by placing 3/8 in. of felt between the Kapton and the filler blocks. The felt will compress allowing the conductor to displace about 0.120 in.[22]

Filler Material

Upon completion of the coil winding the coil is built up with the glue blocks, slip plane, Kapton and NEMA G-11 sheets. The jacket, 1/2-in.-thick 316L stainless steel, is fitted to the exterior of the coil pack. Nominally there is 1/4-in. of clearance. This volume is filled with Epon 815 with chopped fibers and versimide hardener. Figure 40 shows the top filler on the end of the first coil. When this filler is cured the jacket is welded into place. The filler provides a tight load transmitting media to the jacket from the conductor pack.

A washer test was made using the Epon 815 and glass-fiber compound A large steel washer was imbedded into a sample of the material and then thermal cycled 10 times in liquid nitrogen. No cracking was observed from expansion and contraction. Compression tests were made in the LLNL Test Laboratory using the same composition. The results were 10,000 psi to failure in compression, corresponding to a safety factor of 4 compared to the 2500-psi maximum load predicted by analysis.[66]

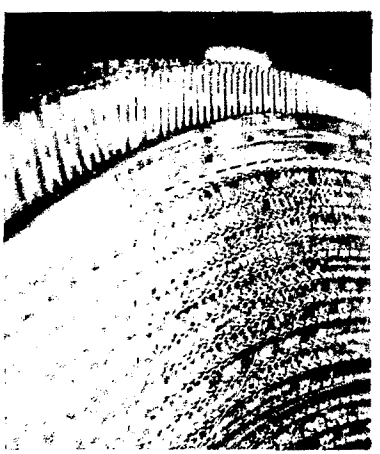

FIG. 40. External joint.

WINDING TECHNIQUES

Prior to the commencement of winding the first MFTF coil a practice coil form was built and 10,000 ft of 1/2-in.-square copper wire was wound to debug the winding equipment and tooling. From this effort a detailed winding procedure[25] was prepared which is a living document that is maintained by the engineer in charge of winding.

The first MFTF coil winding was started in February 1979 and completed six months later, September 1979. This included unwinding the first six layers, delays due to slivers in the conductor wrapping process, and several weeks of delay due to conductor shortages. Winding rates of four layers per week were achieved during the last part of winding when the material logistics were corrected.

CONDUCTOR JOINING

Joining two pieces of Nb-Ti superconductor together has been a subject of extensive study over the past years. Several methods were tested including soft soldering, silver soldering, and cold welding. As mentioned earlier, the cold welding process was the most satisfactory one. It was used successfully for the MFTF test coil although the joint is not as strong as the parent material. It was decided to increase the cold-weld strength and redundancy by adding additional stabilizing copper to the sides of the core.[67] The result of this change was a machined joint tray into which the core is soldered after it has been cold welded. Figure 40 shows an external joint completed in the first coil.

The joint is made by stripping back and removing a section of the copper stabilizer, and then cold welding[54] the ends of the core together. The cold-welded joint is then soldered into the copper joint

tray that provides the mechanical strength as well as the electrical path to assure that there is continuity even if the cold weld were to break. Extensive tensile testing has been done[24] to verify the design concept. The joined conductor is stronger than the parent material, even when no cold weld was made in the core.

A detailed operating procedure[68] as well as detailed check lists have been prepared for joints. The finished coil has a total of 58 joints. Twenty-six are internal joints (against the coil form) and 26 are external joints as shown in Fig. 40.

CURRENT LEADS

Two current leads are required to hook the coil to the external power supply. Both leads have been designed[69] to meet the worst case conditions; i.e., when the full current is carried in gaseous helium, if the superconductor goes normal.

Internal Lead

The lead that connects the end of the first layer and travels vertically across all 58 layers at the center of the small radius and along the top of layer 58 and finally out the helium exhaust port is called the internal lead. This lead is constructed of three massive pieces of copper or bus bars.

External Lead

The external lead is the one that carries the end of the last turn of the last layer on through the helium exhaust port. It too is constructed of a heavy piece of copper bus bar.

The joining of the conductor to the buses is done in a similar manner as the joint tray except there is no cold weld.

The copper bus bars have cooling channels for free helium flow and a piece of Nb-Ti superconducting core is soldered into a grove along the sides. The superconductor is continuous except for two places where joining the buses made it impractical. The joining of the copper bus bars was done using Handy and Harman "Easy Flow" silver solder. It has a melting temperature of 1160°F. The superconductor was soft soldered in the groves with a 50–50 soft solder after the silver-solder joints were made.

Figure 41 shows the current-lead installation for coil No. 1. LLNL drawings AAA79-107723, AAA79-107724 and AAA79-107743 describe the bus bars in detail. Drawing AAA79-107727 shows the assembly of the lead buses.

FIG. 41. Current lead installation for coil No. 1.

The leads are brought out through the helium exhaust port. Analysis[41] shows a magnetic attraction between the leads. They are separated by 2.5-in.-thick NEMA G-11 dividers that have been glued together. The divider is locked into place in the exhaust tube by means of welded guides. The leads are bolted to the divider in such a fashion that the bolts do not go through and are separated by a minimum 2-in. space.

COIL CLOSURE

Figure 42 shows a typical cross section of the coil at the large radius. The closure is done sequentially starting at the small radius ends and progressing towards the center.

The general sequence of events in closing the coil are as follows:

a. install all the NEMA G-11 glue blocks,
b. rout the glue block surface,
c. install the weld backing bars,
d. install the slip plane,
e. install the plenum chamber,
f. complete the ground-plane Kapton insulation,
g. fill the remaining volume to within 1/4-in. of the jacket with solid NEMA G-11 material.
h fill the remaining 1/4-in. with fiber-filled Epon 815,
i. install the jacket section and tack weld in place, and
j. continue the process working from the coil ends to the center.

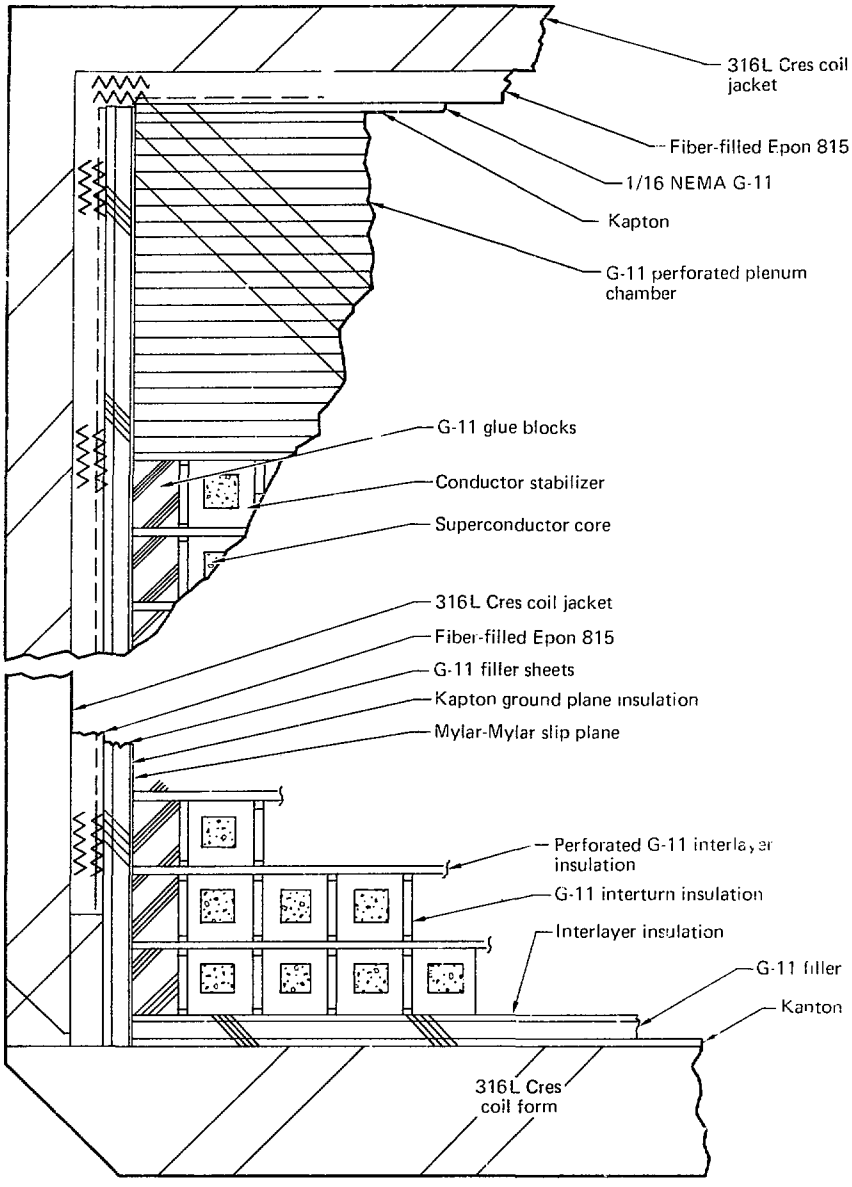

FIG. 42. Large radius—typical cross section.

INSTRUMENTATION

Strain gauges have been installed on the coil form prior to winding as part of the General Dynamics Instrumentation Plan.[70] Additional strain gauges were installed on conductors at layer 2 and 26 to monitor the conductor motions and strains.[47]

Other strain gauges were added to the underside of the coil form to monitor the coil form strains during winding. Voltage taps[71] were installed as part of the coil closure to monitor the voltages at various layers of the coil during operation. Additional voltage taps have been added to the current leads for similar reasons.

QUALITY ASSURANCE

The basic Quality Assurance program for winding is described in the Magnet System Quality Assurance Plan (M-078-06-01). This plan describes the type of records to maintain as well as responsibilities of individuals.

The detailed Quality Assurance requirements for the winding of the coils are given as part of the test of the MFTF Coil Winding Procedure (MEL-78-001432). This defines the responsibilities as well as the forms used to report the measurements and inspections made during the winding operation.

Several inspections are routinely made at the completion of winding a layer:

a. visual inspection for debris, flatness, and any protruding insulation;

b. electrical resistance and Hi-Pot measurements to detect any shorting or debris that may exist;

c. winding gap measurements at four points, measuring the stack height and width; and

d. joint inspection for cleanliness.

All anomalies are corrected before continuing to wind the next layer.

Check lists are used for each joint to assure that no detail is overlooked in the process. Each step of the procedure is signed off by the operator, and the final list is signed by the shift supervisor.

Operating procedures are specified for each operation. These are referenced in the coil winding procedure and all are available on the winding platform.

Shift log books and photographic records are maintained to record problems and progress. Each shift supervisor completes a new page each shift.

All of the data is reviewed daily by the engineer in charge of winding. Any discrepancies are recorded on a Nonconformance Report which is reviewed by a Materials Review Board that decides upon the corrective action or disposition of the discrepancy.

SECTION 5
THERMAL ANALYSIS

The cooldown and warmup thermal analyses of the Lawrence Livermore National Laboratory (LLNL) Mirror Fusion Test Facility (MFTF) magnet system included investigation of a broad range of flow rates and supply temperature schedules. At the onset of these studies there were several objectives or design goals: (1) to cool down and warm up the magnet system within three to five days; (2) to yield acceptable levels of thermally induced stresses resulting from transverse and longitudinal temperature differentials; and (3) to yield acceptable stress levels with or without flow imbalances in separate sections of the magnet. All of these analysis objectives were met.

Details of the initial studies are contained in Ref. 72. As the design evolved and the interplay between thermodynamic and structural analysis became better understood, an iteration of the detailed cooldown and warmup analyses was performed. This analysis particularly emphasized longitudinal temperature variations and is contained in Ref. 73. This document is a condensation and integration of the results of those two prior studies.

COOLDOWN AND WARMUP BASIC ASSUMPTIONS

Cooldown and warmup of the MFTF magnet is achieved by means of helium through-flow in two separate, parallel-flow passages: one through the conductor bundle, and the other through the guard vacuum. A mass flow fraction for each of the parallel flows was apportioned on the basis of the relative mass to be cooled or warmed, 19% of the total flow to the conductor, and 81% to the guard vacuum. The latter flow split was established early in the program and maintained throughout. Subsequent incorporation of additional mass to the magnet case in the form of stiffeners did not alter this recommendation.

The magnet assembly was modeled numerically (Fig. 43) in terms of successive arrays of block-type

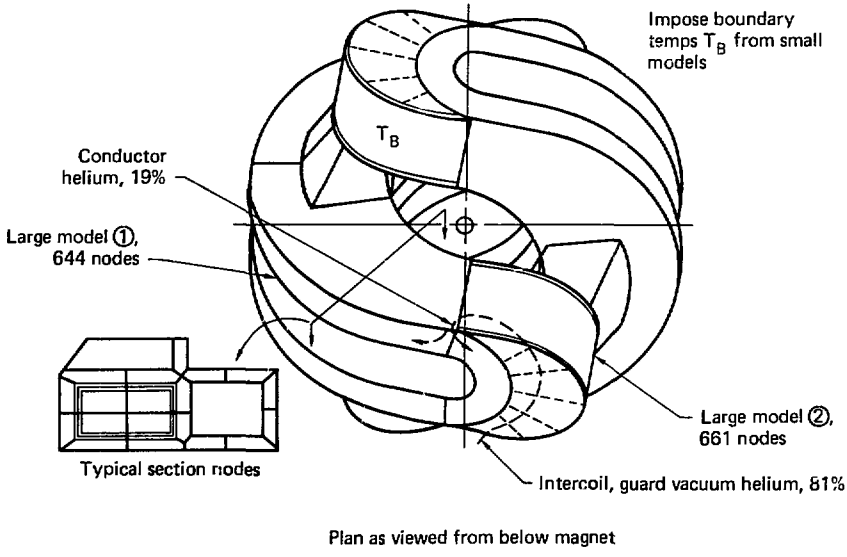

FIG. 43. Cooldown and warmup analysis large models (1) and (2) address transverse thermal gradients.

nodes (i.e., rectangular paralleiepipeds) representing elemental masses of conductor region, potting, jacket, case, coil-extension structure, and intercoil structure. The block-type nodes were provided with convective linkages to adjacent helium-flow nodes, which were ordered directionally to appropriately model the helium throughflow. Convective linkages between flow nodes and surfaces of conductor nodes were based on a laminar flow Nusselt number of 4.0, an effective hydraulic diam of 0.131 cm, and a surface area per conductor of 8.17 cm^2/cm. Each conductor region node contains 348 conduetors.

Guard-vacuum-space helium flow includes flow between the jacket and the case, and between the guard-vacuum baffle and the case. Flow passages of 1/8-in. depth in the jacket cavity and 1/4-in. depth in the baffled cavity cover 50% of the case inner surface, and a laminar Nusselt number of 4.0 was again assumed. Helium flow passes through the intercoil and coil extension structures prior to entering the guard-vacuum space. For the intercoil and coil extension surfaces, a turbulent-flow natural-convection Nusselt number was computed:

$$N_{Nu} = 0.13\,(GrPr)^{1/3} \quad . \qquad (1)$$

The flow rates employed in the cooldown and warmup analyses, up to 340 g/s, represented a preliminary value supplied by LLNL. Supply temperatures for flow schedules were assumed to be controlled on the basis of a measured case temperature located at the lower minor radius. Local flow rates contacting each convectively cooled or heated node were apportioned based on ratios of local-to-total cross-sectional flow area.

Effective properties of the conductor region nodes were computed by an independent analysis, in which mass-weighted average specific heats were generated as functions of temperature, and series/parallel conductive linkages were resolved into directional thermal conductivities, also as functions of temperature. Appropriate heat and conductivity data for 316 SS, 304 SS, and NEMA G-11 fiberglass epoxy were obtained from the exit near the topmost location of the coil jacket. These several flow paths and splits were simulated in both large and small analysis models. Figure 44 shows a worst-case flow-rate schedule where 340 g/s of helium enters the magnet during the time that return temperature is 300 K and varies linearly to 150 g/s with return temperature decreasing to 100 K and remains at 150 g/s for return temperatures decreasing to 4.5 K. The accompanying inlet temperature profile consisted of two steps: 80 K for return temperature >100 K and 4.5 K for return temperature <100 K.

Because the external case stiffeners of Large Model 1 do not have a direct convective linkage to the cooldown/warmup helium, it was anticipated that they would sustain the most severe transverse temperature differentials. Large Model 1 was therefore run with the severe cooldown flow schedule of 340 g/s and 136 g/s at 300 K return temperature to assess the effects of flow rate on transverse differentials. Large Model 2 was run only with the cooldown flow schedule with 136 g/s initial flow rate. The small model was run with these as well as several other cooldown and warmup flow schedules including constant flow rates.

ANALYSIS RESULTS

Figure 45 shows resulting transverse differentials and cooldown duration as a function of the flow rate with 300 K return temperature. This severe flow rate and inlet temperature profile is responsible for the large temperature differentials. Structural analysis of this maximum differential between the stiffener, which is not directly cooled, and the rest of the magnet which is "wetted" by cooldown helium gas, shows that the temperature differential up to 180 g/s yields acceptable stress levels. This corresponds to a minimum cooldown duration of 44 h.

Figure 46 shows the detailed temperature history data during cooldown with an initial flow rate of 136 g/s and two-step inlet temperature profiles. These data are for the cross section midway in the major radius section of the magnet where maximum transverse gradients occur. The "wetted" portions of the magnet exhibit temperatures in a narrow band during cooldown. The stiffener, which is not directly cooled, remains warmer than the case temperatures. In this case, the stiffener is about 95 K warmer (max) than the rest of the magnet and it has been determined that this condition is acceptable by structural analyses.

In contrast, Fig. 47 shows similar transverse gradient temperature histories for the two-temperature step cooldown with maximum initial

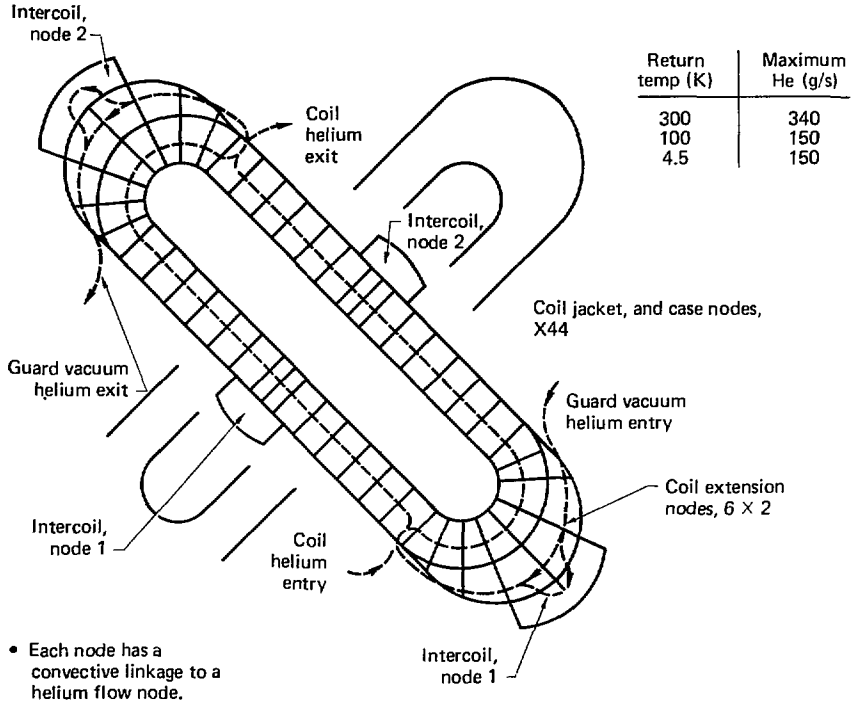

Return temp (K)	Maximum He (g/s)
300	340
100	150
4.5	150

FIG. 44. Cooldown and warmup analysis small model addresses longitudinal thermal gradients and cooldown/warmup durations.

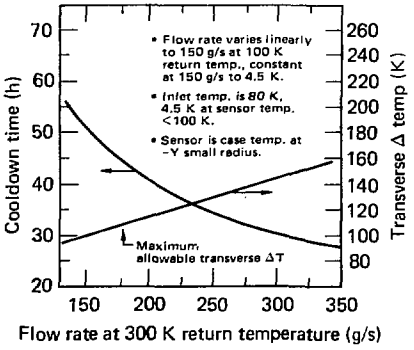

FIG. 45. Cooldown flow rate at 300 K return temperature must not exceed 180 g/s for allowable transverse gradient.

flow rate of 340 g/s. The wide and increasing departure of the stiffener temperature from the more uniformly cooling case temperatures is evident and is so large as to be unacceptable structurally. This is a symptom of the extremely rapid cooldown with this high flow rate.

Figure 48 shows the corresponding 340 g/s (high flow) longitudinal temperature gradients induced in the lower leg of the yin or yang magnet from the coolant inlet to the exit region. Duration into the cooldown is the time parameter. These data are from the literature. The latter data were employed in the cooldown/warmup model for the magnet jacket, case, and potting material, respectively. Data for oxygen-free high-conductivity (OFHC) copper was taken from Ref. 74. Reference 75 was employed for helium properties, and NEMA G-11 epoxy properties were taken from Ref. 76.

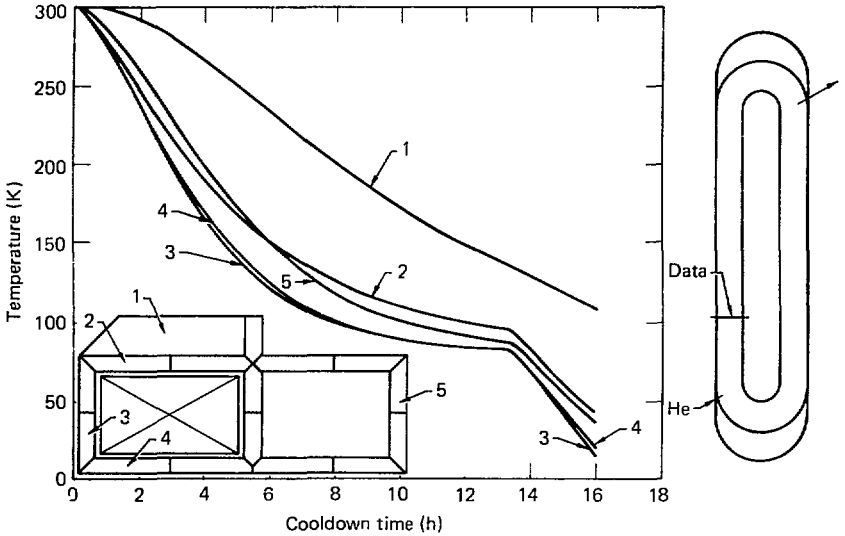

FIG. 46. Cooldown initial flow rate of 136 g/s results in acceptable transverse gradients.

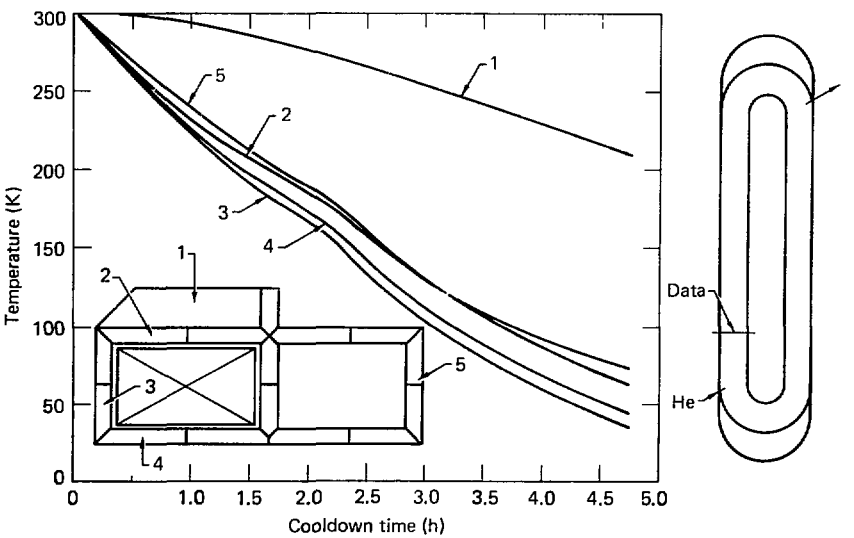

FIG. 47. Maximum cooldown flow rate (340 g/s) causes severe transverse temperature gradients.

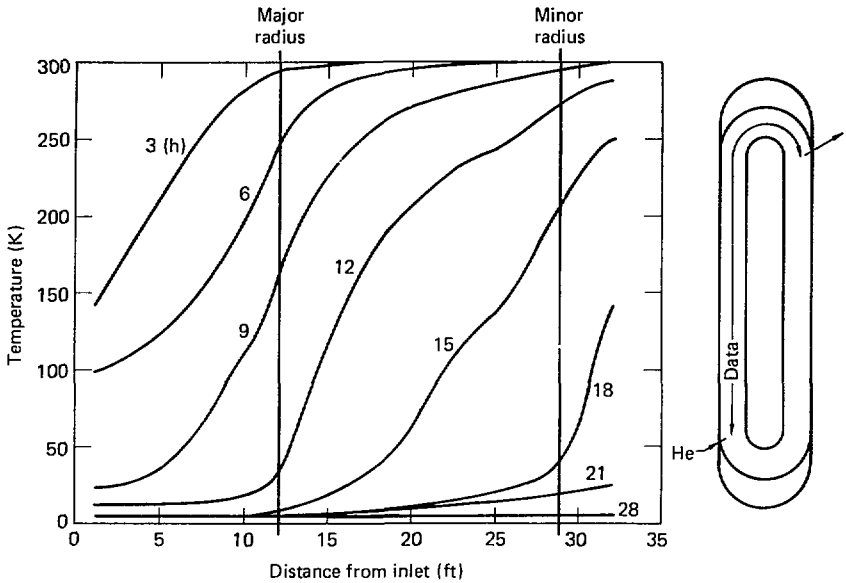

FIG. 48. Cooldown is 28 h with 340 g/s initial flow rate.

Properties of 304L and 316 SS were obtained from Refs. 77 and 78.

COOLDOWN AND WARMUP ANALYSIS MODELS

The cooldown and warmup thermal analysis models were formulated for an improved, unpublished version of the Convair thermal analyzer computer program; the original version is documented in Ref. 79. There are two program modifications affecting the analyses of this report: (1) provision for accepting "block-type" node representation, and (2) optional explicit, forward-marching solution of the heat balance equations. The latter option was employed in cooldown/warmup analysis. All analysis runs were executed on the National Magnet Fusion Energy Computer Center (NMFECC) at LLNL.

Two major models were used during the course of the magnet thermal analysis. A three-dimensional model (shown schematically in Fig. 43) was developed primarily to examine transverse gradients; this model also produced longitudinal gradients. This model was so large it was deemed economical to break it down into two models: Large Model 1 (644 nodes) in the major radius zone of the magnet, and Large Model 2 (661 nodes) in the minor radius, coil-extension zone of the magnet. For the large model, the cross section was nodalized in block-node form, as shown in the cross section in Fig. 43, so that transverse temperature differentials across the magnet cross section could be predicted.

A smaller, essentially one-dimensional model of a total yin or yang magnet (Fig. 44) provided longitudinal temperature distributions and boundary conditions to initiate and drive the large models of Fig. 43. All the transverse nodalization of the large models were collapsed mathematically into one transverse node at each station along the magnet resulting in 44 longitudinally-arrayed nodes around the entire magnet. This model, having much fewer nodes, (total of 119), in addition to providing the boundary conditions for the large model, provided an economical solution for longitudinal gradients, cooldown durations, and thermal effects of the unbalanced flow split into the two legs of the magnet.

Figures 43 and 44 show the guard-vacuum helium (81% of the total), entering the lower coil extension, flowing through it, and then entering the guard-vacuum cavities which surround the coil jacket. While flowing through the coil extension, 57% of the guard-vacuum helium is diverted by relative hole sizes into and out of the intercoil structure to condition its mass. At the top of the magnet the guard-vacuum helium similarly flows through the upper coil extension before exiting the magnet. The coil helium (19% of the total) enters the magnet near the low point and flows up each leg of the winding to join at the top outlet. Magnet cooldown was analysed using the small model with transverse nodes collapsed into a single node; thus at any station along the magnet, the node represents a weighted average temperature. With rapid cooldown in 28 h, very large longitudinal gradients and bottom-to-top differentials occurring at about 12 h (ΔT = 275 K) are evident. Because the longitudinal temperature differential could be driven to such a large value, effort was thereafter concentrated on reducing the longitudinal differential.

Since longitudinal differential was known to be less a function of flow rate than of severity of inlet temperature schedule, a mitigated four-step inlet temperature profile for cooldown was selected. Figure 49 shows the schedule, the cooldown duration, and the bottom-to-top longitudinal temperature differential as functions of constant flow

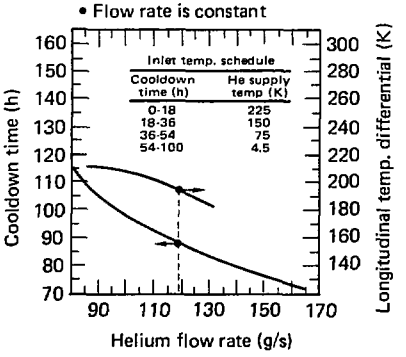

FIG. 49. Longitudinal temperature differences are acceptable for 3.6- to 5-day cooldown durations.

rates. The data confirms the longitudinal temperature differential to be relatively insensitive to flow rate and to decrease with higher flow rates.

The structural analysis was performed for a 119 g/s flow rate that corresponds to a 195 K longitudinal temperature difference and cooldown in 88 h and was certified as acceptable with moderate stresses. The longitudinal-temperature differentials can be accepted for 3.6- to 5-day cooldown durations with the four-step inlet temperature schedule. Figure 50 shows the corresponding detailed magnet longitudinal-temperature profiles from bottom-to-top with cooldown time as a parameter. The acceptable maximum longitudinal differential of 195 K occurs at about 63 h into the cooldown.

Figure 51 shows warmup time and magnet longitudinal-temperature differential as functions of constant warmup flow rate. Warmup is considered to be completed as an accesible condition at 285 K. Again, the four-step inlet temperature schedule was used and is defined in the figure. Because of the less effective use of the heat capacity of the helium by this warming profile relative to that of the cooling profile, this figure shows that the warmup is slower than the cooldown. The maximum longitudinal differentials are milder (and, again relatively insensitive to flow rate) and the transverse gradients would also be milder. The figure shows warmup can be achieved in 122 h (approximately 5 days) with a constant flow rate of 150 g/s. All of these mild longitudinal-temperature differentials during warmup have been deemed acceptable structurally by comparison to the larger differentials of cooldown.

Figure 52 shows the magnet temperatures versus distance from the conditioning flow inlet during warmup with 150 g/s flow and the four-step inlet temperature schedule. Time into the warmup is shown as the parameter. The maximum differential of 120 K occurs about 65 h into the warmup.

The effects on transverse gradients and longitudinal-temperature differentials of the yin or yang magnet, or between the two magnets, may be assessed structurally. The temperature data could be taken in detail from Refs. 89 and 90. However, the gradients in the two legs of a magnet or between magnets are essentially independent one to the other, depending only on the different flow rates in those individual paths. Therefore, Figs. 45, 49, and 51 indicate the differences in temperature gradient and differentials for different flow rates

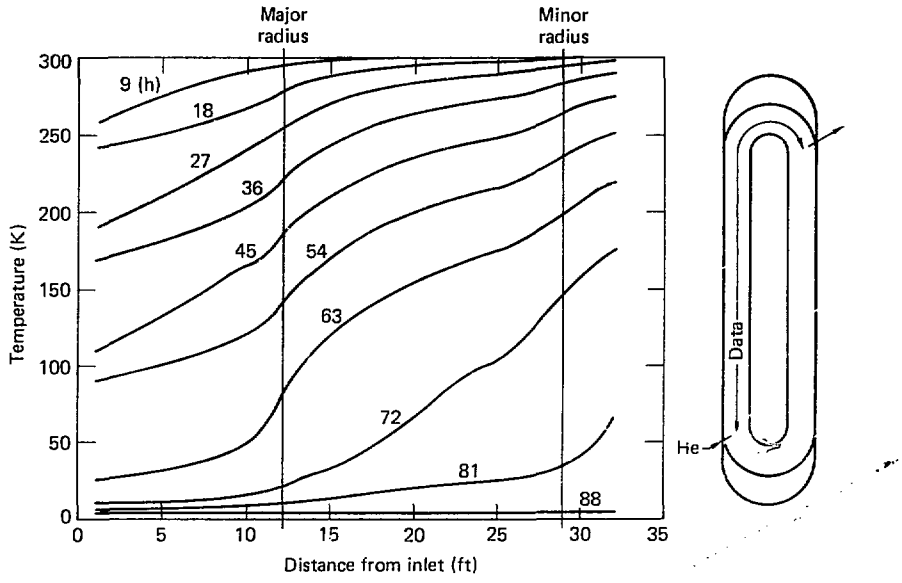

FIG. 50. Longitudinal temperature gradients for 119 g/s flow rate with 4-step cooldown inlet temperature schedule were structurally evaluated to be acceptable.

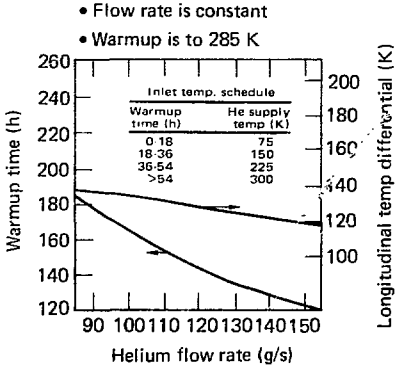

FIG. 51. Warmup in 3 to 5 days yields mild longitudinal gradients.

(unbalanced flow splits) into the different portions of the magnet system. Structural analysis for a severe flow imbalance in the separate legs of a single magnet in which the helium flow rate in one leg was 40% greater than that in the other leg results in mild and acceptable stresses.

CONCLUSIONS AND RECOMMENDATIONS

1. Cooldown analyses employing the large model (Fig. 43) yielded detailed temperature excursion and transverse temperature differential data. Resulting thermal stresses are acceptable to a maximum flow rate of 180 g/s at 80 K inlet and 300 K return temperatures. Resulting cooldown time is 44 h.

2. Longitudinal temperature differences employing the small model (Fig. 44) have been structurally certified acceptable at a 119 g/s flow rate

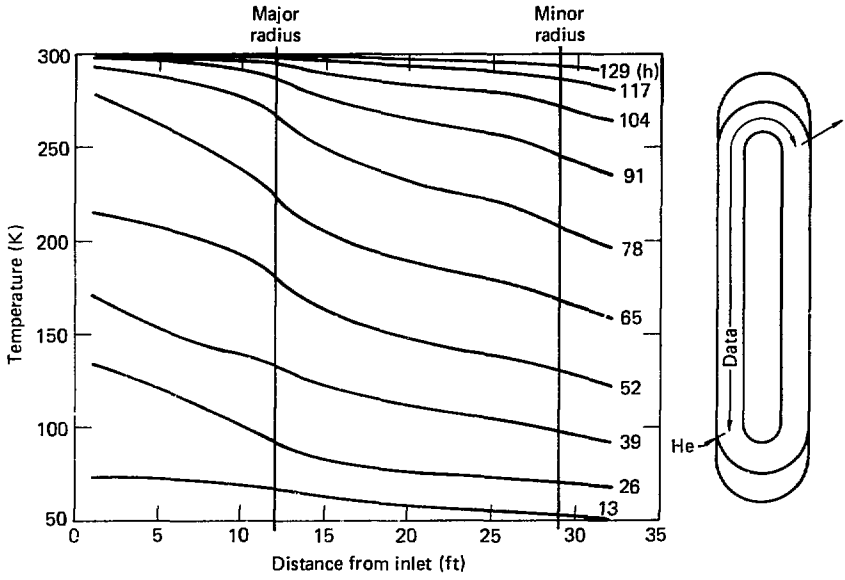

FIG. 52. Warmup to accessible conditions is achieved in 5 days with 150 g/s flow rate and 4-step inlet temperature.

with the four-step inlet temperature profile achieving cooldown in 88 h. Reduction of longitudinal gradients with higher flow rates also implies acceptability for higher flow rates.

3. *With the following four-step inlet temperature schedule:*

Cooldown time (h)	Helium supply temperature (K)
0 to 18	225
18 to 36	150
36 to 54	75
>54	4.5

Total flow rates to 119 g/s and cooldown in 3.6 to 5 days accommodate stress constraints and are acceptable.

4. Warmup with the following four-step supply temperature management schedule:

Warmup time (h)	Helium supply temperature (K)
0 to 18	75
18 to 36	150
36 to 54	225
>54	300

Total flow rate of 150 g/s yields mild and acceptable temperature gradients. Warmup time to 285 K is 122 h (approximately 5 days).

5. Since magnet gradients are influenced more by reduced severity of inlet temperature schedule than by flow rate, gradually decreasing (increasing) or finer step-wise decreasing (increasing) helium supply temperatures could permit even higher flow rates and faster cooldown (warmup). If deemed expedient these options would require further study and thermodynamic/structural analysis certification.

SECTION 6
CRYOGENIC SYSTEM

The cryogenic system for the MFTF magnet provides liquid helium to the magnet coils to maintain a superconducting state. Several interfaces and effects must be accounted for in the magnet system design to achieve this condition. Moreover, the magnet system must be able to survive numerous rapid discharge cycles without detrimental effects. These topics are reviewed in the following text.

INTERFACES

The magnet will be supplied with liquid helium through dedicated lines running between the vacuum vessel ports and the magnet. As illustrated in Fig. 53, each magnet coil has separate supply and return lines.

The magnet assembly will be supported by two hanger and five stabilizer struts. Heat conduction in these struts is minimized by liquid nitrogen-cooled barriers.

Liquid nitrogen-cooled heat shields will completely envelope the magnets for thermal radiation protection. Figure 54 shows these shields, with additional water-cooled shields in critical areas, to protect the nitrogen shields from beam and plasma heating.

Another interface with the magnet is the current leads penetrating the vacuum vessel wall, where the lead temperature must make a 5 to 300 K transition. Also, the temperature and strain sensors on the magnet will be a source of heat transfer to the liquid helium.

LIQUID HELIUM SYSTEM

The piping system for supplying liquid helium to the magnet is illustrated in Fig. 55. Each magnet coil has dedicated supply and return lines and valves except at the helium Dewar penetrations. Flow through the magnet is by natural convection with liquid entering the bottom of the magnet, splitting at the bottom of each coil, flowing up each half coil and rejoining before exiting out at the top. The principal reason that the yin-yang pair is oriented at 45° is so the helium will flow in this manner.

Important to the thermal control of the magnet is an adequate circulation of LHe. Forced pumping is not practical, so natural circulation was chosen, because it has been satisfactory in smaller magnet systems. A computer model of the LHe natural circulation was developed to estimate steady-state

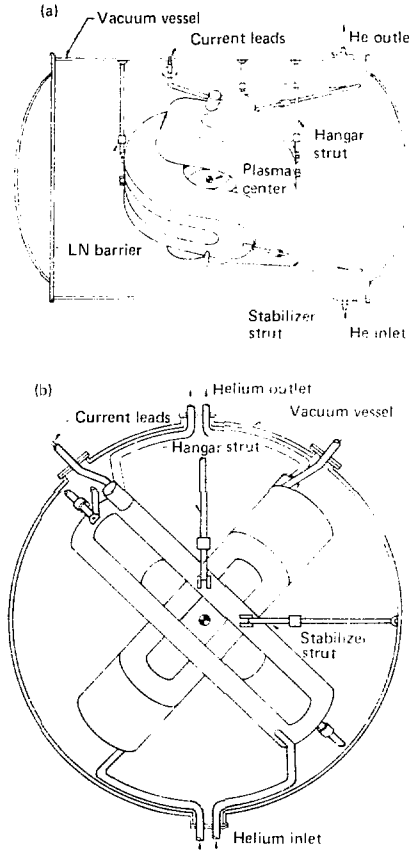

FIG. 53. Schematic of magnets in the vacuum vessel showing LHe lines, support struts, and current leads.

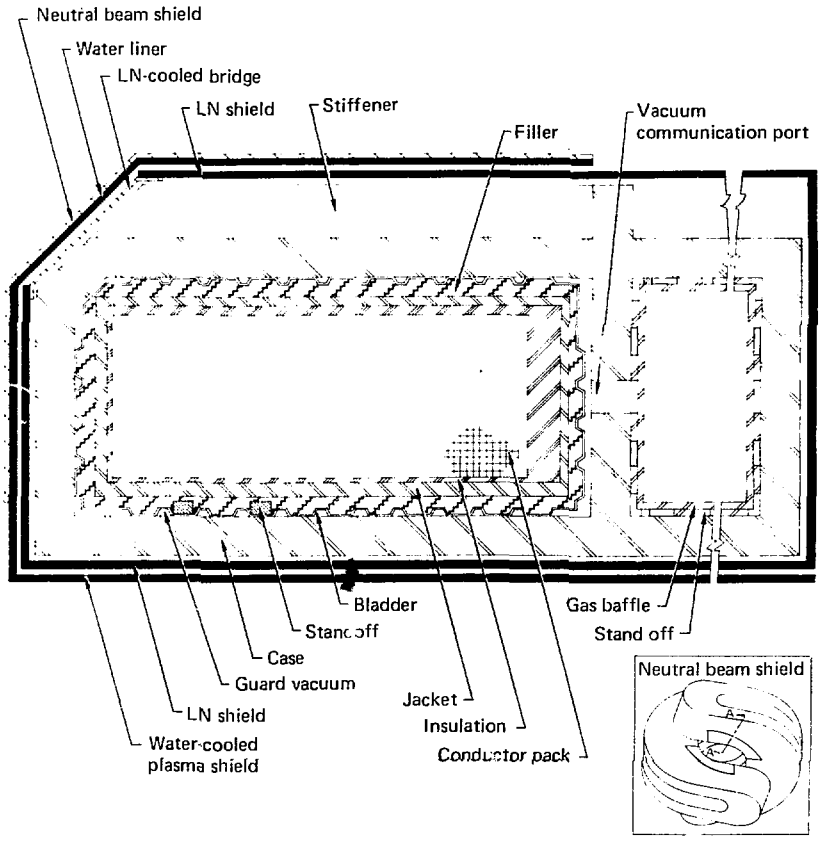

FIG. 54. Sectional ("A-A") view of the magnet showing its construction and thermal shields.

mass flow rate and vapor quality. Also, a sensitivity study was made to determine which parameters have the greatest influence and to estimate the range of uncertainty for LHe flow rate.

The principal requirement of the LHe system is to maintain quality with less than 10 vol% vapor in the magnet. Heat-transfer analyses indicate that significantly higher vapor qualities would probably reduce cryostability.

The conductor pack and magnet shape do not immediately lend themselves to a simple flow-modeling approach. Therefore, three approaches to modeling the magnet were considered: (1) the Blasius friction equation, (2) Darcy's porous media equation, and (3) a three-dimensional orifice model. In selecting an appropriate method, estimates of hydraulic diam, flow tortuosity, porosity, permeability, friction factor, and effective orifice dimensions were made, and the three approaches were compared by means of their respective pressure drops. The porous media approach resulted in the smallest pressure drop, the Blasius approach yielded a pressure drop 10 times greater, and the orifice approach gave a pressure drop that

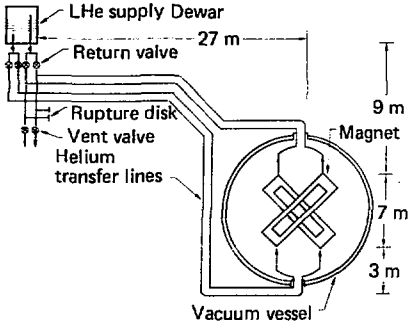

FIG. 55. Schematic of the piping systems for supplying LHe to the magnets.

was 1000 times greater. We rejected the orifice assumption as unrealistic, and chose the Blasius friction method over the porous media approach because it was more conservative. Thus, the magnet pressure loss ΔP was estimated with a modified Blasius friction equation in the following form:

$$\Delta P = f L_m \eta d_h M^2 / 2 \tau A_p^2 \phi^2 \quad . \qquad (2)$$

Flow in the magnet is expected to be laminar by the Reynolds number definition, so that the friction factor (f) is given as:

$$f = 64 \mu A_p \phi / \eta M d_h \quad . \qquad (3)$$

Pressure losses in the piping system were simply modeled using loss coefficients for bends, valves, entrance-exit regions, and other effects. These were calculated as functions of the friction factor f. The effect of two-phase flow was also included by using the Lockhart and Martenelli correlation: flow in the piping system was assumed turbulent.

Helium flow rates were estimated by an iterative computing method. Using an assigned heat load for selected flow model elements and an assumed flow rate, helium properties were determined by each element node using NBS data. The resulting pressure imbalance in the flow circuit due to cumulative contributions of friction, momentum, and gravity was computed. The flow rate was readjusted and the calculations repeated until the pressure imbalance was acceptably small. This procedure provided a means for determining the effect of heat load on flow rate (Fig. 56a). Also, vapor quality was determined and appears as a function of heat load in Fig. 56b.

Because the modeling procedure entails some uncertainties, we were interested in how sensitive the results were to changes in certain variables. Table 14 shows the maximum expected range in these flow parameters, and Table 15 shows our estimate for the total LHe-system heat input. The results of the sensitivity study are reflected in Figs. 56a and 56b by the uncertainty range curves.

The effects of two-phase flow are significant for helium mass qualities as low as only 1% and flows near 300 g/s. Surprisingly, the static head inside the LHe Dewar is the most significant parameter affecting mass flow rate because of the relatively low fluid-flow resistance of LHe. Also, pipe friction is far more influential on flow than either magnet friction or heat input.

On the basis of this calculation we selected a pipe with a 6-in. (15-cm) inside diameter for the LHe supply and return lines. This pipe size and our estimated system heat load of 510 W yields an equilibrium mass flow rate of approximately 750 g/s. Vapor quality at the top of the magnet is less than 5 vol% (0.7% by mass), and it is less than 25 vol% at the top of the return line. These results imply that an adequate safety margin has been provided in the thermal control of the magnet.

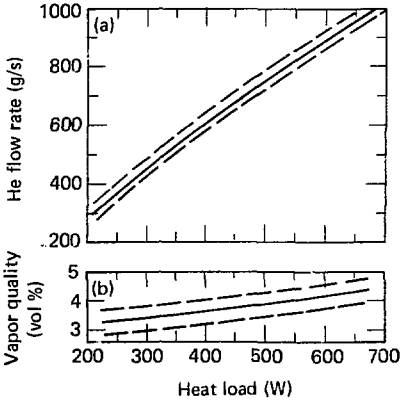

FIG. 56. Steady-state LHe natural circulation through the magnets.

TABLE 14. Uncertainty range of flow parameters.

Parameter	Range
Friction factor, f	0.014 to 0.018
Tortuosity factor, η	1.5 to 2.0
Porosity, ϕ	0.30 to 0.35
LHe Dewar head, m	0.5 to 1.0
Hydraulic diameter (d_h), cm	0.15 to 0.35
Piping heat leakage, W	30 to 80
Length of piping, m	80 to 100

TABLE 15. Liquid-helium-system heat sources.

Parameter	Heat input, W
LN shield radiation	160
LN shield conduction	90
Magnet hanger rods	60
Conductor joints	45
Instrumentation leads	70
Helium ducts	85
Total	510
Current leads, max. vent rate	1.6 g/s

A plenum space is included at the top and bottom of each coil near the supply and outlet ports, as illustrated in Fig. 57. These plenums are 6-cm thick and constructed of 6.5-mm-thick layers of NEMA G-11 having 5- by 37-mm slots alternately oriented 90° to each other. They provide a 50% bearing surface for the conductor and a 0.5 porosity for helium flow. Both plenums distribute flow entering and leaving the coil, and the top plenum also provides a space for vapor to flow outside the coil so the conductor will always be liquid-cooled.

A detail of the helium outlet from the conductor pack is shown in Fig. 58. Current leads contained in these ducts are wrapped with Kapton to prevent voltage breakdown to the conductor pack and surrounding structure. The supply duct at the bottom of each coil is identical except for the absence of the current leads.

Outermost turns of the conductor in the outside flat areas in the large-radius regions of each coil are supported by beveled NEMA G-11 backing blocks. These blocks support magnetic pressures of nearly 20 MPa (2900 psi) and are beveled, as illustrated in Fig. 59, so that vapor can migrate upwards through the channels to the plenum.

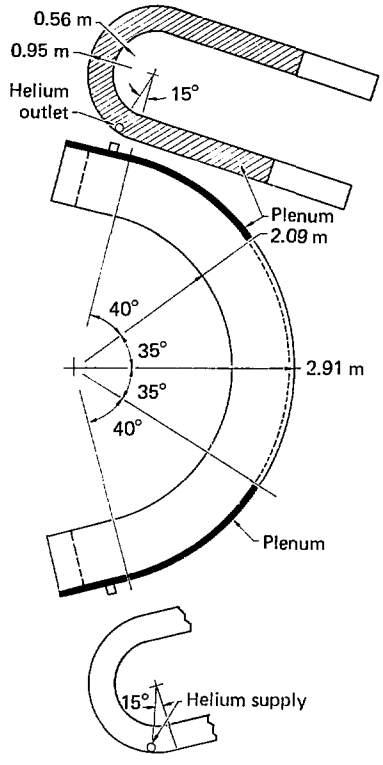

FIG. 57. Jacket around coil showing dimensions and locations of helium plenums.

CRYOSTABILITY

The MFTF superconductor is cryostable from experimental and analytical studies. The High Field Test Facility (HFTF) at LLNL has demonstrated the conductor will recover if driven to a normal state in a horizontal solenoid configuration at the MFTF peak field and current conditions. Convair/General Dynamics and General Atomic made analytical studies of conductor cryostability and concluded there is sufficient heat transfer for the conductor to recover in the peak field and current condition.

A comparison of calculated surface heat flux on the conductor when in a normal condition to experimentally measured heat flux is shown in Fig. 60.

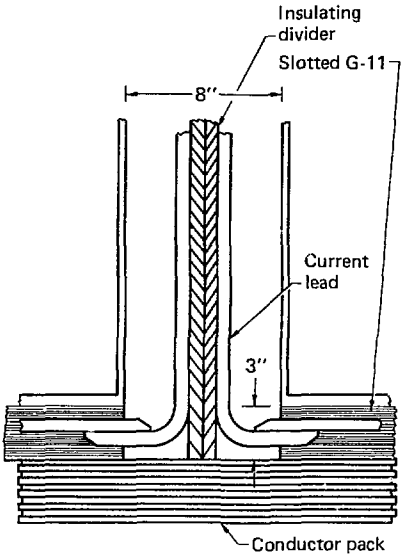

FIG. 58. Helium outlet for magnet.

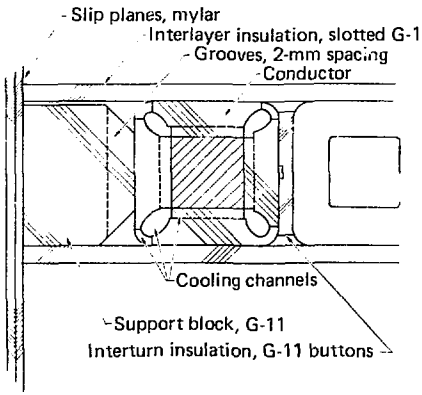

FIG. 59. Conductor and support blocks in outside layer of large-radius region of magnet coil showing channels for helium flow.

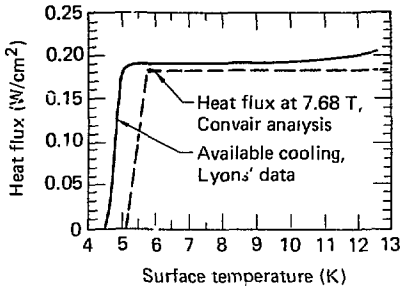

FIG. 60. Conductor heat flux.

The available cooling exceeds the surface heat flux by approximately 5%, resulting in a small margin for uncertainties or flaws. Moreover, a calculation by Convair of the effect of solder flaws on cryostability indicated that a worst case had practically no effect. (A worst-case solder flaw is defined as no more than 27 flaws of 40% contact or less per 1.5 m of conductor, or less than 13 flaws per 7 cm, or less than 8 consecutive flaws on one side.)

Plenums and flow channels are provided in the magnet to inhibit vapor accumulation, as described in the foregoing section, and thus help assure cryostability.

CURRENT LEADS

A pair of copper bus conductors with superconductors will carry current from the vacuum vessel wall to each magnet. These conductors will normally be in liquid helium, but they are designed to be superconducting in vapor flow. If the liquid level in the current lead pipes should be depressed, the leads will be cooled by cold-end conduction and by controlled vapor flow. A heat transfer analysis of these leads has provided a design that should guarantee cryostability for all operating conditions. By using 2.5- by 7.5-cm (1- by 3-in.) OFHC copper conductors having a residual resistivity ratio greater than 150, a Nb_3Sn superconductor with a 0.4-g/s vapor flow per lead, the vapor-cooled length operating at 6,000 A can be over 4 m, which is more than sufficient. A section view of these conductors is shown in Fig. 61.

The portion of the leads penetrating the vacuum vessel wall will have a temperature transition from approximately 5 K in the current lead

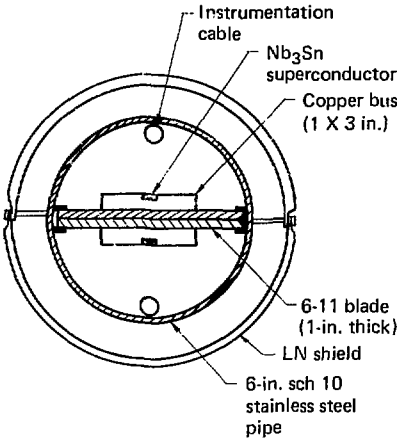

FIG. 61. Helium-cooled current bus.

pipe to 300 K outside the vessel. They are designed to use near-optimum helium flow and to have a sufficient amount of thermal mass for safe operation by using concentric copper and stainless steel tubes. The leads will be constructed of approximately 60 copper tubes 0.25-in. o.d. (6.35 mm) by 0.025-in. wall (9.65 mm) by 60-in. long (1.5 m). Each copper tube is encased in an 0.31-in.-o.d. (8 mm) stainless steel tube. This design gives a mass ratio of stainless steel to copper of about 2:1 and should permit approximately 20 min of adiabatic operation at 6000 A before a fast discharge of the magnets must be initiated.

The effect of the stainless steel on the lead electrical resistance is small as can be shown by analysis. Equating joule heating in the lead to convective cooling gives an expression for the lead length in the following form:

$$\ell = \frac{\dot{m}\Delta e A_c \dfrac{A_s}{A_c}\dfrac{\bar{\rho}_c}{\bar{\rho}_s} + I}{I^2 \bar{\rho}_c} \quad , \tag{4}$$

where $\dot{m}$ is the helium mass flow rate, Δe is the helium enthalpy change, I is the lead current, A_c and A_s are copper and stainless steel cross-section areas and ρ is the electrical resistivity integral over the dimensionless length x/ℓ.

$$\bar{\rho} = \int_0^1 \rho \, d\left(\frac{x}{\ell}\right) \quad . \tag{5}$$

Flow circuitry for these leads is shown in Fig. 62. A by-pass open-close valve is included to maintain flow in the event of a failure of the flow-control valve. Helium flow will ordinarily be regulated proportional to lead current with a controller using the lead voltage drop as the input signal. A 2.5-cm vent line will be connected to the helium duct, as shown in Fig. 62, to prevent the liquid level from being depressed too far.

QUENCH

In the event of a quench, the magnet will automatically be put into a fast-dump mode by a quench detection computer. Voltage taps on the coil bundle and current leads will be used to detect normal conduction zones. The contained energy will be dissipated in an external discharge resistor that will be sized to limit both voltage and maximum conductor temperature.

A conservative method for estimating the maximum conductor temperature T, in time τ with current I and resistance R, is to compute an adiabatic temperature rise of each element, including the mass m_i, length L, and heat capacity c_i.

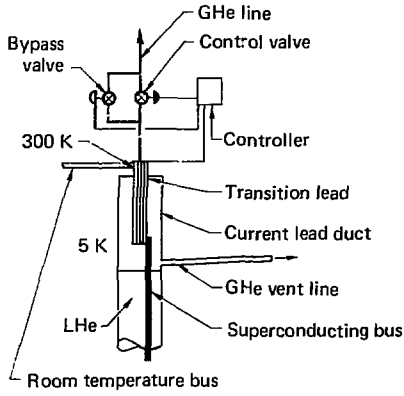

FIG. 62. Transition lead.

$$\int_0^{\infty} R\,d\tau = \sum_i Lm_i \int_{T_0}^{T_{max}} c_i\,dT \quad . \quad (6)$$

Instantaneous thermal communication between the conductor and adjoining materials is assumed. The participating materials are the superconductor, copper, interlayer and interturn insulation, and helium gas.

The current history is defined according to the delay time τ_d.

$$I = \begin{cases} I_0, 0 < \tau < \tau_d \\ I_0 \exp(-\tau/\tau_0), \tau > \tau_d \end{cases} \quad . \quad (7)$$

Since R can be expressed in terms of resistance length and area, $\rho L/A$, Eq. (5) can be restated in the following form:

$$\frac{I_0^2 \tau_0}{A}\left(\frac{\tau_d}{\tau_0} + \frac{1}{2}\right) = \sum_i m_i \int_{T_0}^{T_{max}} (c_i/\rho)dT \quad . \quad (8)$$

Solution of Eq. (8) yields the maximum temperature as a function of delay until a discharge is initiated. This decay constant corresponds to a peak voltage of 1000 V across a 0.17-Ω quench resistor, with a 12-H inductance in the magnet (i.e., $\tau_0 = HI_0/V_{max}$). Copper properties assumed in Eq. (8) are those of OFHC copper having a residual resistivity ratio equal to 150 and a 7.76-T magnetic field.

Figure 63 shows that a maximum temperature of 200 K is reached if a 10-s delay in initiating discharge is allowed. Longer decay time constants (i.e., lower quench voltages) result in higher temperatures. This temperature is considered permissible since it is a conservative estimate and is limited to a small region of the coil where both initial transition to normal conduction and peak field could occur. A 200 K temperature rise from 5 K should result in less than 0.1% thermal expansion of the conductor. Also, 10 s is adequate time to initiate a discharge with an automatic quench detecting system.

Magnet structural materials can also develop resistive heating during a fast discharge by a transformer coupling effect between the magnet coil and surrounding structure. Because of its properties, a copper guard-vacuum bladder would show the greatest temperature increase from this source. Assuming adiabatic conditions, resistive and sensible heating of the copper can be equated.

For a 1392:1 turn ratio, a peak coil voltage (V) of 1000 V, and a current-decay time constant (τ_0) of 69 s, the temperature (T) can be found by Eq. (9).

$$\frac{0.26\,\tau_0}{VL_e^2} = \int_{T_0}^{T_{max}} \rho c\,dT \quad . \quad (9)$$

where L_e is the effective length and ρc is the product of resistivity and specific heat.

Solution of this equation yields a maximum temperature of 5 K for the copper bladder; it is much less for a stainless steel bladder.

A similar analysis of the stainless-steel case yields a temperature of 10 K. Total energy dissipation in the case, bladder and coil jacket is approximately 6 MJ, or less than 1.5% of the energy contained by the magnet before discharge.

Heat transfer to the helium occurs at a much slower rate than the inductive heating and has no effect on conductor stability because any appreciable amount of vapor is formed long after the current has decayed to a low value.

Rupture discs in the vent lines will limit vapor pressures during a quench to approximately 80 psi. The gaseous helium recovery system can accept up to 16,000 g/s, which will be adequate.

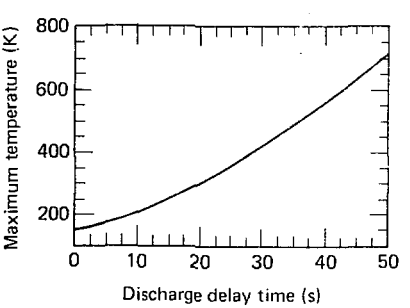

FIG. 63. Maximum conductor temperature during a quench.

REGENERATION

All liquid helium cooled surfaces of the magnet system must be warmed periodically to more than 15 K for boil-off of condensed hydrogen. This is to be accomplished by radiating heat to the magnet case and piping from the nitrogen shields. However, the shields must first be filled with a warm gas and the magnet must be discharged. Helium vapor generation in the magnet system will be used to depress the liquid helium level to the bottom of the vacuum vessel and pump liquid into the storage system. After regeneration, the nitrogen and helium systems will be returned to their normal states as soon as possible.

SECTION 7
POWER SUPPLY SYSTEM

The power supply system for the yin-yang superconducting magnet provides controlled power and protection in case of quench or other potentially destructive conditions. Principal requirements for the power supply system are: provide a controlled current of 0-6000 A in each coil with an offset of up to 1200 A between coil currents; provide a means to energize and deenergize the magnet within 4 hours; provide detection of quench or other abnormal condition in the magnet; and deenergize the magnet, either in a slow or rapid mode, upon detection of an abnormal condition. Two identical power circuits are used for each of the superconducting coils (Fig. 64). Control and coordination of the two power circuits and detection of an abnormal condition in the power supply system or the magnet is done locally in the power supply and magnet protection controller.

SYSTEM DESCRIPTION

The power circuit for each coil consists of a 0-12 V, 0-6000 A(dc) power supply for energizing the coil and maintaining the current during steady state, a 0.0015-ohm resistor in parallel with a pneumatic controlled switch for slow de-energizing of the coil, and two 6000-A, 750-V(dc) circuit breakers with a center tapped 200-MJ resistor for fast de-energizing of the coil. The dc power supply is a conventional thyristor phase-controlled rectifier with a freewheeling diode path rated for full current. A pneumatic switch is in parallel with the power supply to bypass the supply if its cooling water fails. The slow de-energizing resistor and pneumatic switch are used to insert resistance in series with the magnet coil during operator controlled turndown or an equipment failure of a noncritical magnitude. Two fast de-energizing dc circuit breakers are used to interrupt the current from the power supply and transfer it to the 200-MJ resistor if a critical condition in the magnet is detected, such as a propagating normal zone or overheated current lead. The 200-MJ resistor is a passively cooled resistor of the natural air convection type. It is center tapped with a soft ground to limit the coil voltage to 500 V or less from ground.

The power supply and magnet protection controller interfaces with the MFTF computer system besides being a complete local system which can operate independently. Its most significant function is to: monitor key signals such as voltage taps in the coils, current lead voltages, helium level and pressure, and failure indicators in the cryogenic system; process the information to determine if an abnormal condition exists and its severity; and then initiate a hold on the current rise, a slow de-energizing command, or a fast de-energizing command.

An uninterruptable power system is used to ensure operation of the magnet protection components during a power outage. A 120-V(dc) battery supplies control power to the circuit breakers and input power to an inverter which powers the power supply and magnet protection controller. The ac building power is used as a backup in case of inverter failure.

ENERGIZING AND DE-ENERGIZING CHARACTERISTICS

Figure 65 shows the energizing and slow de-energizing characteristics of the power supply system. With 12 V from the power supply and an inductance of 12 H in series with the cable resistance of 0.5 mΩ, the current increases at nearly 1 $A \cdot s^{-1}$. Actual energizing characteristics will be slower and will use the full 4 hours allotted. This is to minimize probability of rate-induced normal zones developing in the magnet at high current. With the power supply turned off and with 2 mΩ in series with the 12-H inductance, the magnet current decays completely in 3 hours. A slower rate of decay can be obtained by leaving the power supply on; however, it is not anticipated that this will be needed.

The fast de-energizing characteristic is not shown in the figure. It would be an exponential decay with a time constant of approximately 70 s.

POWER COMPONENTS

The major power components are the power supplies, pneumatically controlled switches, 1.5-mΩ resistors, dc circuit breakers, 6-kA bus, the 200-MJ fast de-energizing resistors, and the battery/inverter

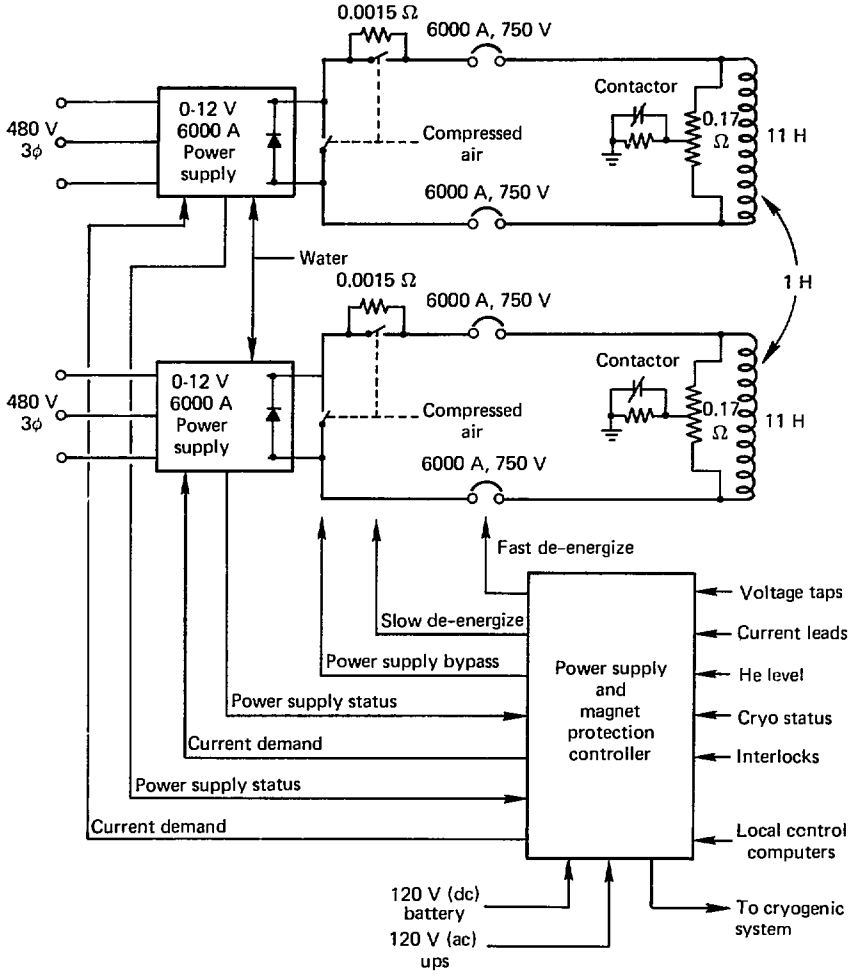

FIG. 64. Magnet power-supply system.

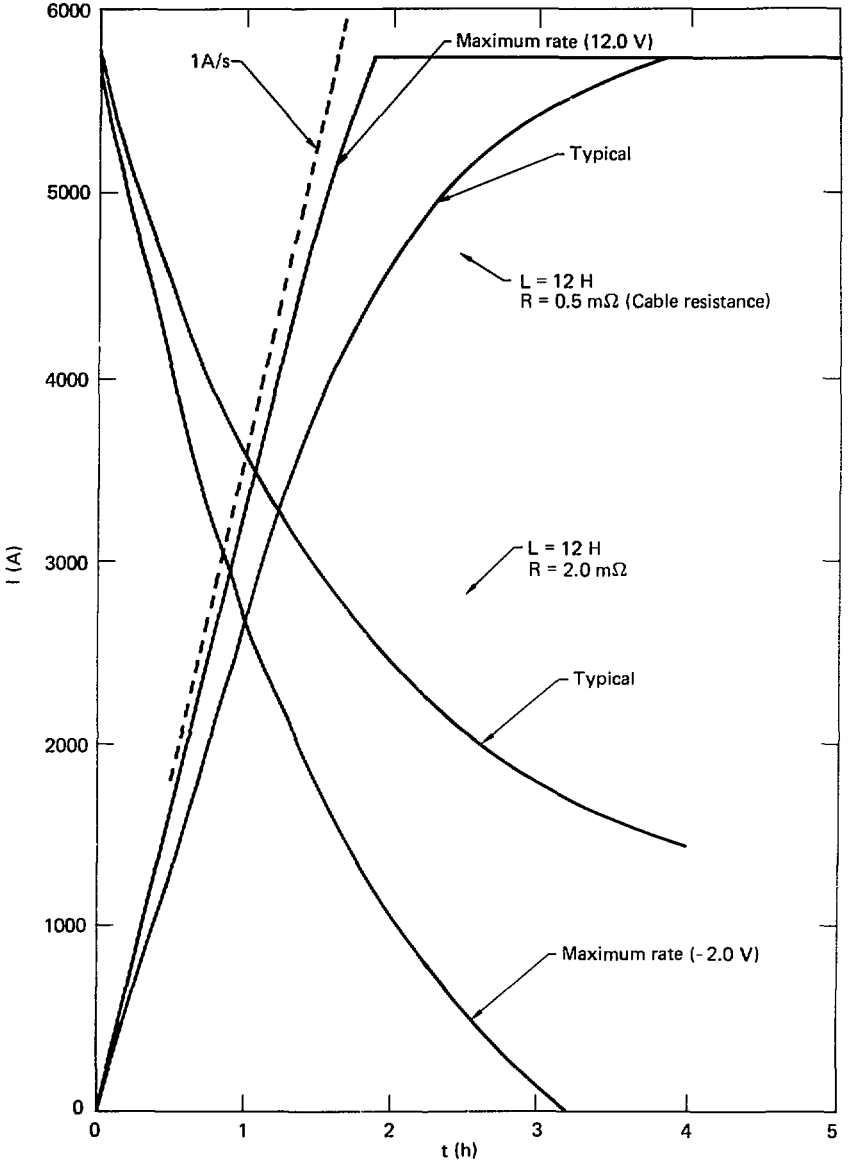

FIG. 65. Energizing and de-energizing characteristics.

system. With the exception of the fast de-energizing resistors and the 6-kA bus, all the power components are located on the third floor, northeast end of Bldg. 431. The fast-dump resistors are located on top of the southeast vessel support pillar.

Power Supplies

Each power supply will be built to EE Department Specification LES 22249. The supplies will produce 0-12 V, 0-6000 A with a series connected load of 12 H and 0.5-2.0 mΩ. The 0.5 mΩ is the cable resistance and the 2.0 mΩ is the cable resistance plus 1.5 mΩ of the slow de-energizing resistor. A continuously rated free-wheeling diode path will be provided so that the magnet current will not be interrupted if the power supply or the input ac line voltage fails.

The power supply is required to produce full output with 480 V ± 5% input. It will operate continuously at reduced output voltage down to 416 V and for 0.2 s down to 330 V. This latter voltage occurs during starting of motors in the cryosystem.

The power supplies will operate either in a local or remote mode, but local mode is only for operation of the power supplies into a dummy load during initial checkout and maintenance. The remote mode is used during operation of the magnet and corresponds to operation of the supplies from the power supply and magnet protection controller. Power supply current and voltage demands will be four 20-mA analog signals provided from the controller, while digital inputs and outputs of zero and 24 V will be for on/off, local mode inhibit, and power supply diagnostic indicators. The power supplies will be capable of both current and voltage regulation with automatic crossover, but the magnet will be primarily operated in current regulation with the voltage regulator serving as a voltage limit. The maximum absolute errors are ±60 A and ±0.5 V with maximum repeatability errors of ±30 A and ±0.5 V.

The power supply output terminals are isolated by ±1000 V(dc) from the power supply enclosure, ac input terminals, and control ground. This is to prevent a ground fault during the fast de-energizing mode where ±500 V exist between each magnet terminal and ground.

No filtering is required in the power supplies because of the high magnet inductance. A ripple frequency of 350 Hz or greater was specified with special precautions for minimizing lower frequency harmonics.

Pneumatically Controlled Switches

The switches which parallel the power supply outputs and the 1.5 mΩ slow de-energizing resistors are Square D type DB or equivalent. These switches are capable of continuous operation at 6000 A and can interrupt 6000 A up to 20 V. They are mounted in series with the interconnecting bus bars which are used in the magnet power supply area.

Control of the switches is with a conventional pneumatic control system employing an air-cylinder operator, a four-way solenoid valve, and a pressure regulator. An accumulator will be used with a check valve to provide a backup source of air to allow operation with loss of building air. The four-way solenoid valve is connected to the switch using polypropylene tubing to separate the switch and the controls by ±1000 V(dc).

The switches which parallel the power supply outputs are normally open and close automatically when commanded by the power supply water flow and overtemperature monitors. The switches which parallel the 1.5-mΩ resistors are normally closed and open when commanded by the power supply and magnet protection controller. All of the switches have limit switches for monitoring by the controller.

1.5 Milliohm Resistors

The 1.5-mΩ resistors are used for slow de-energizing of the magnet. They are rated at 54 kW and are natural-convection air cooled.

dc Circuit Breakers

Two dc circuit breakers per EE Department Specification LES 22250 are used for each magnet coil for redundancy, and will be mounted on open frames in the power supply area. They are capable of operating at 6000 A(dc) continuously and will interrupt up to 300 kJ of stored energy in the inductance of the cables and the fast discharge resistors. Although rated to operate in a 750-V(dc) circuit, they actually can operate up to their arc voltage of 2200 V.

The control circuit of each circuit breaker will be powered from a 120-V battery. Each breaker will have an undervoltage release which will automatically open the breaker if the control circuit

voltage falls below 70 V. The primary means of opening the circuit breakers is the shunt trip coil, which will be controlled from the power supply and magnet protection controller. Individual driver circuits are used for each breaker. The breaker position auxiliary switches are used for monitoring by the controller and also for interconnecting the breakers to ensure opening of all four breakers simultaneously (Fig. 66).

6-kA Cable Bus

The cable bus runs from the power supply area to the magnet lead exit ports are approximately 100-ft long. Cable bus will be used which is similar to cable tray but with maintained spacing between conductors for sufficient cooling to allow the cables to be sized as single conductors in free air. The advantages of cable bus over rigid bus are: continuous cable runs without needing expansion joints; and redundant personnel safety due to having insulated cables in an enclosed, grounded duct. Details of the cable bus design will be done by the manufacturer.

200-MJ Fast-Dump Resistors

During a fast de-energized condition, the magnet energy is dissipated in the fast dump resistors. The resistors will be passively cooled using natural air convection. The resistors will have several parallel paths to provide redundancy.

A cable independent of the 6-kA bus will be used to connect the magnet leads at the top of the vessel to the dump resistors which are located on top of the southeast vessel support pillar. Independent cable is used to ensure that the dump resistors are connected in case of damage to the 6-kA bus. These cables are sized for short time ratings and will not operate at 6-kA continuously.

Battery and Inverter System

A 120-V, 100-A-h battery, 25-A charger, and a 2.5-kVA inverter comprise the uninterruptable power supply system (Fig. 67). The battery is of lead-calcium construction with a translucent jar for high reliability and ease in maintenance. The battery is composed of 20 separate units mounted in a seismic, two step rack. The inverter operates from the battery and supplies power to the power supply and magnet protection controller. It has an electromechanical transfer switch which transfers the power source from the inverter to the building ac power in case of inverter failure. The estimated mean time between failure for the combined power source is more than 100,000 h. As shown in the figure, several conditions in both the charger and inverter are monitored by the controller.

POWER SUPPLY AND MAGNET PROTECTION CONTROLLER

The power supply and magnet protection controller is a local control system which can operate in conjunction with the MFTF computer system or independently. It will be located in the power supply area in the northeast corner of Bldg. 431.

Functions

The controller has a means for selecting local or remote operation using a keylock switch, checking out components prior to application of power to the magnet, monitoring of component failures, and selecting a hold, slow, or fast de-energizing command. It also communicates to the Local Control Computers in Bldg. 439 through a CAMAC crate. Based on digital commands from the local control computers it provides analog current and voltage demands to the power supplies, generates the energizing trajectory, controls insertion of the 1.5-mΩ resistors, and controls on/off commands to the power supplies.

The most critical controller function is to provide magnet protection. It monitors: voltage taps in the magnet for detection of a normal zone (quench), voltage taps across the current leads for detection of overtemperature, helium level and pressure in the helium supply Dewar for detection of quench or near quench conditions, and failures in the cryogenic and vacuum systems to anticipate a potential loss in cooling of the magnet, or large heat influx. Based on the severity of an abnormal condition, the controller selects a hold, slow, or fast de-energizing command.

Required Features

Because of the critical nature of magnet protection, the following features will be included in the controller. The quench detection and current lead voltage monitoring will have fully redundant systems. Self-checking will be used in low reliability components such as microcomputers. Checkout of key components prior to operation will be done automatically where possible. Checkout will continue during early stages of energizing the magnet.

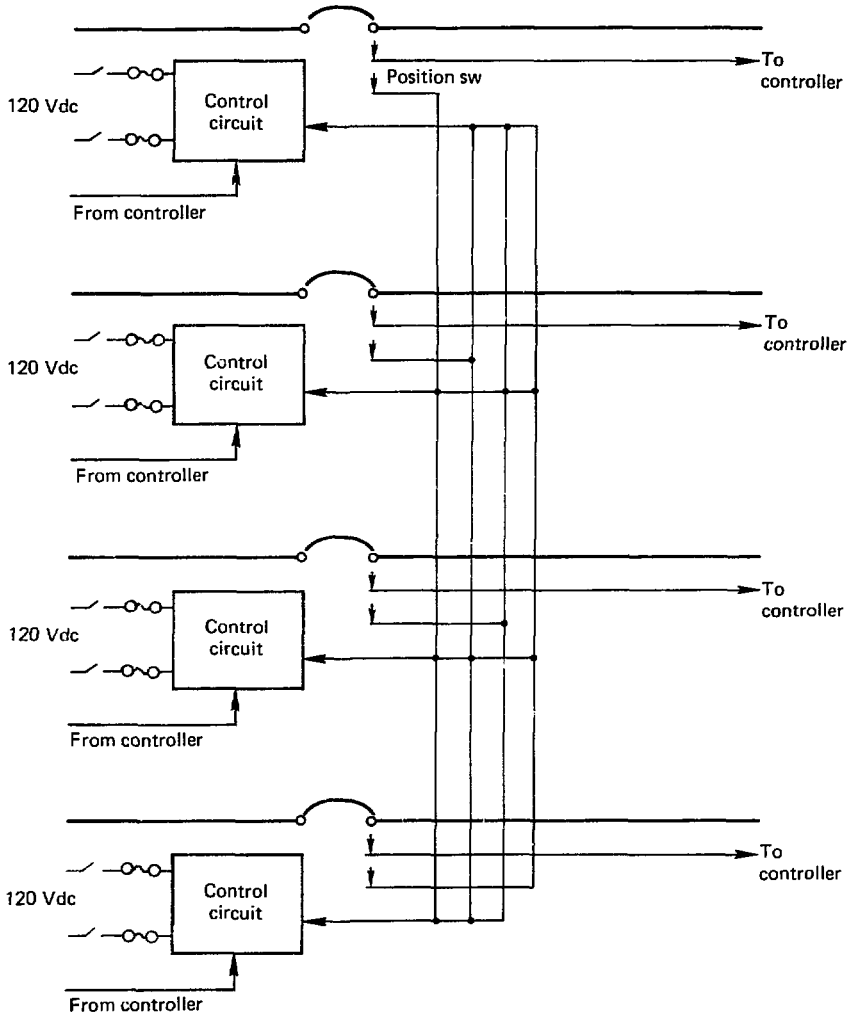

FIG. 66. Circuit breaker interconnections.

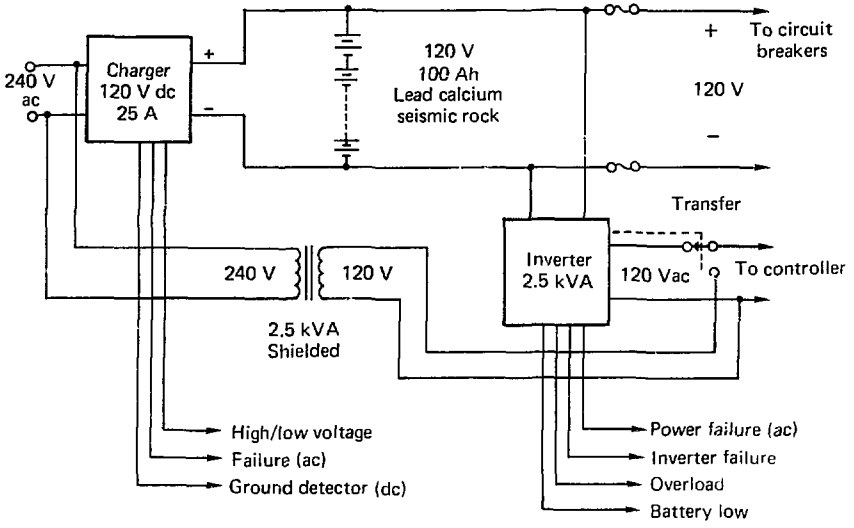

FIG. 67. Battery and inverter system.

De-energize Modes

As stated earlier, there are three modes of operation if an abnormal condition in the power supply system or the magnet occur: hold, slow de-energize, and fast de-energize. The hold mode stops the increase in current during energizing. The slow de-energize mode turns the power supplies off and inserts 1.5 mΩ in series with each magnet coil. The fast de-energize mode opens all four dc circuit breakers and sends a signal to the cryogenic system to close the supply valves from the Dewar and open the valves to the helium recovery system.

Table 16 shows the main failure conditions and the appropriate action which will be initiated. The basis for this table is the failure modes, effects, and criticality analysis performed by Intermagnetics General Corporation (IGC).[80] This table also reflects the use of the fast de-energize mode as the last line of protection. This is to minimize disruption to the MFTF operation and to minimize probability of voltage failures in the magnet.

Quench Detection

Detection of a normal zone in the magnet will be done by monitoring the voltage taps in both coils and by monitoring helium pressure in the helium supply Dewar. Use of the voltage taps enables detection of normal zones as short as 1 m, identification of their approximate location in the coils, and their growth behavior. Use of the helium pressure enables detection of normal regions in the coil but not their location or growth characteristics. It is used to cover potential blind spots in the electrical quench detector, and because it is a completely different type of detector and would not have a fault mode in common with the electrical detector.

Based on temperature rise calculations and experimental normal zone propagation rates of approximately 1 m/s, the magnet will enter the fast de-energize mode at a normal zone length of approximately 10 m. To detect small stable normal zones and to monitor growth rates it is required to detect a normal zone as small as 1 m. Detection of growth rates is required to discriminate against fast signals which occur due to conductor motion and electromagnetic interference.

Detection of a 1-m length requires detection of 26 mV of resistive voltage (at 6000 A) in the presence of ±12 V of inductive voltage during energizing or de-energizing. A well known method for quench detection with a single coil is the balanced

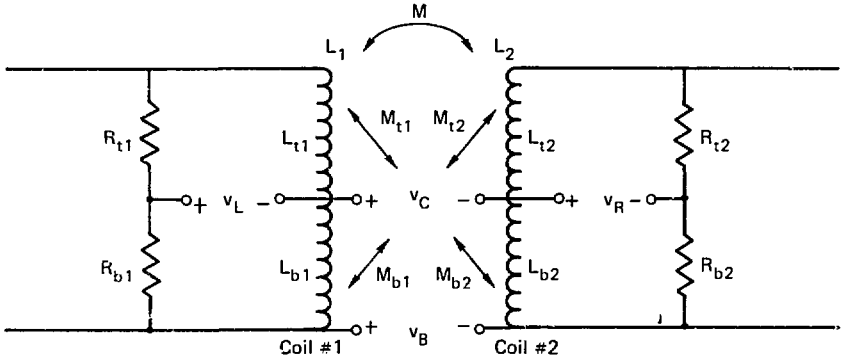

Detector equation: $v_o = K_1 (v_C - v_B) + K_2 (v_L - v_R)$

For similar coils:

$$\left.\begin{aligned} L_{t1} &= L_{t2} = L_t \\ L_{b1} &= L_{b2} = L_b \end{aligned}\right\} \; L = L_t + L_b = L_1 = L_2$$

$$\left.\begin{aligned} M_{t1} &= M_{t2} = M_t \\ M_{b1} &= M_{b2} = M_b \end{aligned}\right\} \; M = M_t + M_b$$

$$K_1 = \frac{M_b}{L_b}\left(\frac{1 - \dfrac{L_b M}{L M_b}}{1 - \dfrac{M_t}{L} - \dfrac{L_b}{L}}\right)$$

$$K_2 = \frac{1 - \dfrac{M_b}{L_b}}{1 - \dfrac{M_t}{L} - \dfrac{L_b}{L}}$$

For MFTF:

$$\left.\begin{aligned} L_t &= 5.79\text{H} \\ L_b &= 5.32\text{H} \end{aligned}\right\} \; L = 11.11\text{H}$$

$$\left.\begin{aligned} M_t &= 0.532\text{H} \\ M_b &= 0.617\text{H} \end{aligned}\right\} \; M = 1.149\text{H}$$

$$v_o = 0.0265 (v_C - v_B) + 1.869 (v_L - v_R)$$

FIG. 68. Quench detection method.

TABLE 16. Failure conditions and appropriate action.[a]

Condition	Appropriate action		
	Fast	Slow	Hold
Growing normal zone, (>10 m)	X		
Stable normal zone (<10 m)		X	
Current lead overheating			
Voltage alarm, level 1		X	
Voltage alarm, level 2	X		
Low helium level in Dewar		X	
High helium pressure in Dewar			
Pressure alarm, level 1		X	
Pressure alarm, level 2	X		
Valve from helium Dewar closes		X	
Main vacuum failure, major		X	
Guard vacuum failure, major		X	
LN system failure			X
Helium refrigeration failure			X
Magnet-protection controller failure[b]		X	
MFTF computer failure			X
dc power supply failure		X	
Battery charger failure		X	
Inverter failure		X	
120-V(ac) power failure		X	
Inverter and 120-V(ac) power failure	X		
120 V(ac) to circuit breaker failure	X		

[a]Based on failure modes, effects, and criticality analysis performed by Intermagnetics General Corporation.

[b]Quench detector, current-lead voltage alarms, and helium pressure alarm have backup systems.

self-inductance bridge method. Because MFTF has two coils which are coupled together with a coupling coefficient of approximately 0.1, and because the large dimensions of the coil cross-section result in varying coupling depending on voltage tap location, the self-inductance bridge method cannot be used in the conventional manner Based on calculations using the EFFI code, approximately 70 mV result in the bridge due to mutual inductance imbalance. IGC in their quench detection and magnet protection study[80] proposed using current rate indicators to compensate for the mutual inductance imbalance.

An analysis done by LLNL resulted in a quench detection method which successfully compensates for mutual inductance imbalance without requiring current rate sensors.[81,82] Two voltages between coils are used in addition to the self-inductance bridges to form a detector equation (Fig. 68). The gains K_1 and K_2 are functions of the partial mutual and self inductances in the two coils.

HARDWARE IMPLEMENTATION

Detailed design of the hardware for the power supply and magnet protection controller has not been completed. One implementation was described in the IGC study.[80] The selected design uses a programmable controller with an analog backup for quench detection and current lead monitoring.

SECTION 8
STRUCTURAL ANALYSIS

INTRODUCTION

A baseline structural analysis was performed in support of the preparation of the MFTF design drawings. This analysis demonstrated the basic structural integrity of the MFTF structure using the best available loads and material data. Subsequent to the completion of the MFTF design, additional analyses were performed. These refined the finite element analysis in the critical stress region, and interpreted the finite element results in light of the latest material properties and actual structural effects such as stress concentrations. Also investigated were the potential effects of assumed structural faults in critical magnet structure. These analysis tasks are summarized in separate sections. The following discussion summarizes the structural requirements analysis methods and results from the baseline structural analysis documented in Ref. 10.

STRUCTURAL REQUIREMENTS

Materials

The structural case material for the MFTF magnet is 304LN CRES steel with a nitrogen content of 0.14% (minimum). The weld metal is E316L. The coil-jacket plate material is 316 CRES steel as is the jacket weld metal. Design stresses for the MFTF case and weldments were based on anticipated yield strengths of 120 ksi at 4 K and on the expectation of adequate fracture toughness and flaw growth rates. The preliminary plate and weld mechanical properties were obtained from the National Bureau of Standards (NBS) for use in the case design (Table 17), along with properties for the other structural materials in the magnet.

Factors of Safety

The basic requirement imposed on the magnet case structure was that there should be a factor of safety of 1.5 on an anticipated 120-ksi yield strength for the operating magnetic and thermal loads. The factors of safety on the remainder of the magnet structure are consistent with the ASME code as in Table 18.

Design Load Conditions

The MFTF magnet must withstand both operating and fault conditions. Design loading conditions include cooldown, warmup, and normal operating conditions, operating and fault magnetic conditions, and seismic inertia conditions. In addition to these conditions, the magnet is also designed to a 2.0 g handling condition.

TABLE 17. Structural material mechanical properties.

Material	Usage	Temp, K	Ultimate strength, ksi	Yield strength, ksi	Elastic modulus, 10^6 psi	Source
304L	Support struts	RT	100	40	28.5	LLL
		4.5	245	70	29.5	
304LN	Magnet case and intercoil	4.5	244.6	111.8[a]	29.7	NBS
E316L $\Delta Fe = 4.5$	Case weld metal	4.5	193	116[a]	31.9	NBS
$\Delta Fe = 9.2$		4.5	187	128[a]	31.9	
316L	Jacket	RT	80	40	29.5	
		4.5	200	80	31.9	
EPON 828/Versamid 125 with chopped glass fiber	Conductor shimming	20	~14700	-	-	GDC EMS 0-0096-51
CPR Upjohn Polycast 1009-78	Jacket-to-case	RT	~13250	-	0.387	Mfgr Data
A286	Support bolts	RT	140	95	29.1	AMS 5737H

[a]120 ksi was used for design pending determination of final allowables.

TABLE 18. Magnet structural safety factors.

Structure or condition	Factor of safety: Yield strength	Factor of safety: Ultimate strength	Factor
Case, jacket, intercoil	1.5	-	4.0
Support structure	1.5	3.0[a,b]	4.0
Shields, shield supports	1.5	3.0[a]	-
Seismic safety factor	1.25	2.5[c]	-

[a]Based on ASME codes requirements.

[b]Ultimate strength safety factor is 2.0 in welds.

[c]ASME codes allow an increase in allowable working stress for seismic conditions of 120%.

Magnet loads were determined for both normal operating (both coils 100% energized) and fault conditions (one coil 100% energized, one coil inoperative). The case plate magnetic pressures for the more critical normal operating condition are shown in Fig. 69. Also defined were the ground accelerations for the seismic inertia conditions. Magnet accelerations and support system loads are a function of both magnet system and fusion chamber and were determined by a dynamic analysis. Magnet case loads for seismic condition were calculated by General Dynamics Corp. (GDC) based on assumed 1.0 g vertical and 0.75 g horizontal accelerations. Thermal loads in the magnet due to longitudinal and transverse thermal gradients during cooldown were calculated using finite element structural analyses thermal distribution.

ANALYSIS METHODS

The stress analysis of the MFTF magnet and its support system is based on data from three separate finite element analyses: a large 7000-degree-of-freedom GDSAP analysis of one-quarter of the magnet, detailed MSC/NASTRAN models of typical case cross-sections, and a simple beam-element model of the complete magnet and its supports. The large GDSAP model determined the overall stresses and deflections for the magnetic loads, quench pressure loads, and the normal operating 4.5 K temperature condition. MSC/NASTRAN models were used to refine the local case bending stresses for the magnetic load conditions, and a GDSAP beam element model was used to determine the overall magnet loads for the unsymmetric seismic and cooldown thermal conditions. These models are discussed below and are documented in Ref. 10.

The 7000-degree-of-freedom plate model of the MFTF magnet is shown in Fig. 70, representing one quarter of each magnet and the interconnecting load-block structure.

The coil jacket, case structure, and intercoil structure are represented by linear-strain thin-plate elements, which simulate the axial and bending stiffnesses of the plate structure. The conductors are represented by six continuous rod elements that represent the lumped axial stiffness of the pack. These elements are connected to the surrounding case and jacket structure by other rod elements that simulate the transverse stiffness of the conductor pack including the conductor, insulation, and effective gaps.

The loading conditions for the GDSAP plate model are all quarter symmetric. Magnetic loads for both the normal and fault conditions were calculated for an idealized (5 × 12) conductor grid used in an EFFI analysis. The loads on the EFFI grid were lumped together at the GDSAP conductor nodes and applied to the finite element model. Loads for the normal operating condition assume 100% operating current in both magnets, while loads for the EFFI fault condition are based on 100% current in one magnet and no current in the other. A quench pressure condition consisted of a uniform 700 psi bursting pressure applied to the case plates surrounding the conductor pack. The normal operating 4.5 K temperature condition was analyzed to determine the residual stresses in the magnet caused by the differences in thermal contraction between the case and the conductor.

The output from this analysis consisted of the overall stresses and deflection in the magnet conductors, jacket, and case. However, the element mesh in this model was too coarse to provide a detailed definition of the local bending stress distributions in the magnet case plates. Therefore, a detailed MSC/NASTRAN model of the case cross section was created to refine the overall GDSAP analysis results. This NASTRAN model refined the local case bending stresses as illustrated in Fig. 71 and documented in Ref. 10.

The NASTRAN model was used to analyze three typical sections in the magnet's major radius. Models of the case at $\theta = 24°$, 48°, and 72° were

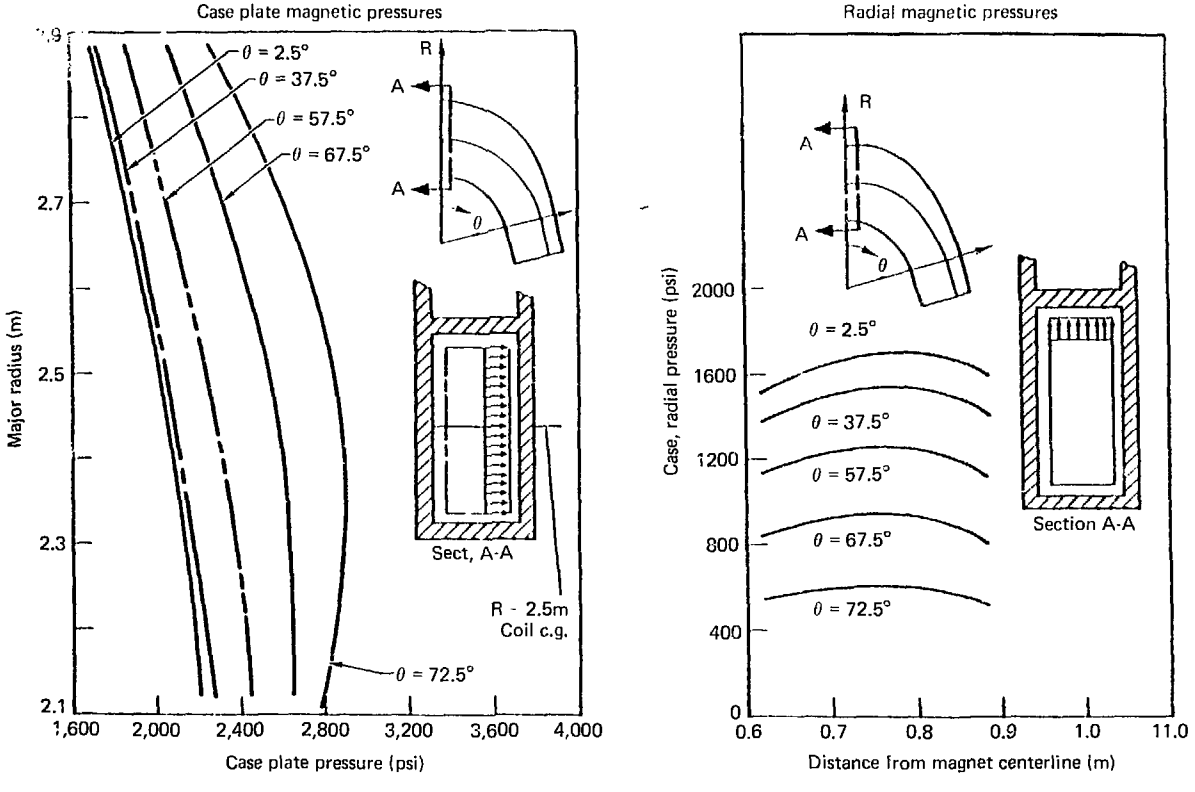

FIG. 69. The conductor pack exerts high pressures on the magnet case.

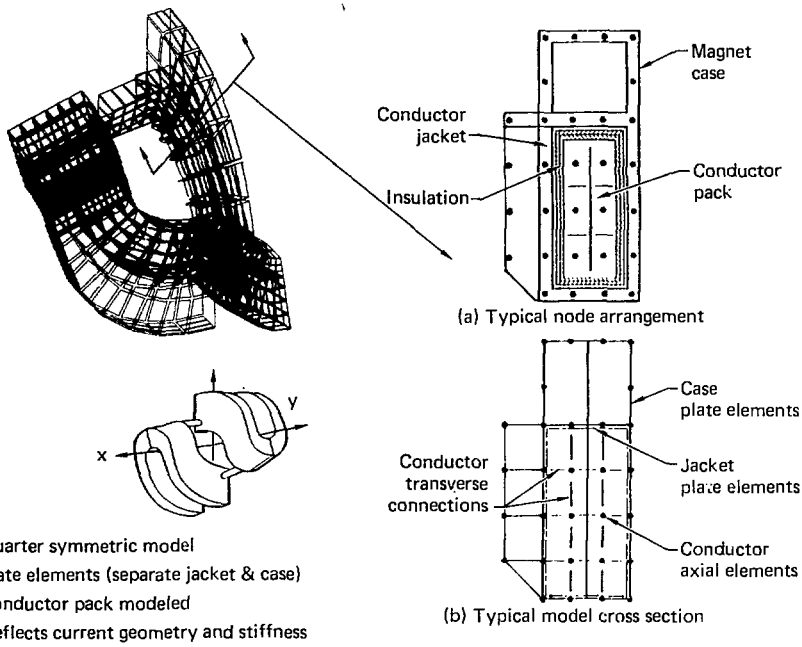

FIG. 70. The GDSAP finite element model accurately represents the MFTF structure.

created with the only differences between the models being the thickness of the side plate stiffener, the depth h of the guard-vacuum section of the case, and the applied loads.

The magnetic loads are applied directly to the NASTRAN model case plates as distributed pressure loads, shown in Fig. 69. Additional pressure loads were applied to the NASTRAN model to simulate the effective radial pressures created by the axial stresses existing in the curved crossover plates. These pressures were calculated from the longitudinal stresses obtained from the GDSAP analysis. By assuming that a longitudinal stress f_L in the curved plate with radius R and thickness t would create an effective radial (normal to the plate) pressure $P = f_L t/R$ in addition to the pressure loading, forced displacements were applied to the NASTRAN model to ensure deflection compatibility with the overall GDSAP analysis.

The GDSAP beam element model illustrated in Fig. 72 was created to determine the overall magnet and support loads for the unsymmetric inertia and thermal condition and is also documented in Ref. 10. Because the inertia and thermal stresses were expected to be small, the simple beam element model was considered adequate to confirm that the seismic and cooldown conditions were not critical. The model grid points, which are shown in Fig. 72, are located at the centroid of the conductor pack. The mass and axial stiffness of the coil are represented by rod elements connected to the model grid and the axial and bending stiffnesses of the magnet case are represented by beam elements whose centroids are offset from the conductor thermal conditions. The cooldown thermal conditions addresses temperature gradients due to three symmetric and three unsymmetric helium flow distributions during cooldown. Temperature distributions for these

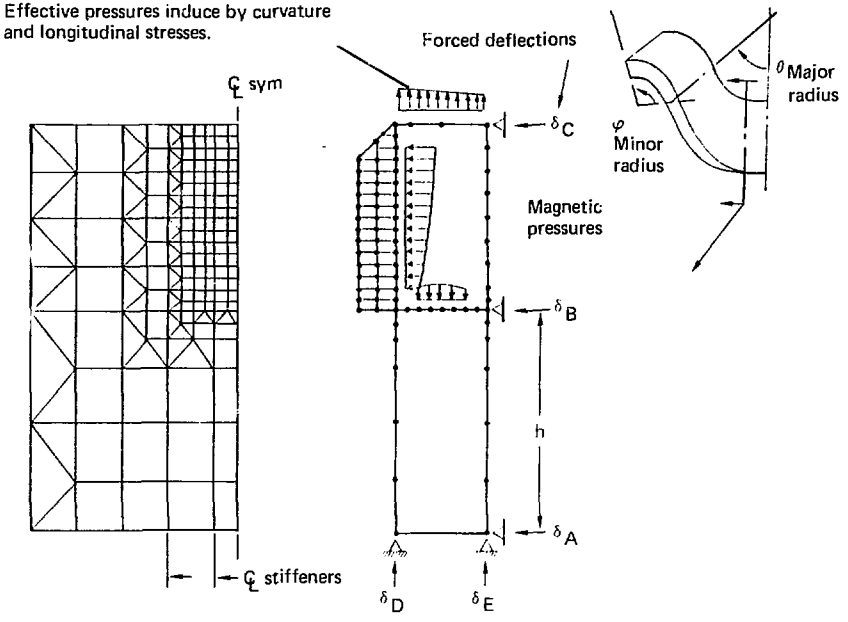

FIG. 71. The NASTRAN finite element model refines the case bending moments.

various flow distributions are documented in Ref. 72.

ANALYSIS RESULTS

Case Stress Analysis

The case stress analysis can be broken into two categories: the analysis of the major radius, and the analysis of the minor radius. In the major radius, the primary in-plane (membrane) stresses are caused by the C-clamp action of the magnet. The secondary bending moments are caused primarily by redistribution of the magnetic pressure loads applied to the side plates as shown in Fig. 73. In the minor radius, the in-plane stresses are caused primarily by the spreading or opening up action of the major radius lobes. The secondary bending moments are caused by redistribution of the seven million pound intercoil load and by the effects of the high in-plane stresses acting in the curved minor radius plates, also shown in Fig. 73.

Major Radius Analysis

The critical in-plane stresses in the major radius case plates were determined entirely by the GDSAP plate model finite element analysis. The plate secondary bending moments were determined by the same analysis but were also refined by the Nastran analysis of typical case cross sections. In the center crossover plate where the Nastran and GDSAP moments differed because of the manner in which the magnetic pressures were applied. the structure was analyzed for the worst combination of moment and in-plane loads. Fig. 74 shows the combined primary and secondary stresses at several locations in the case. All principal stresses were less than 80 ksi.

Peak stresses in the magnet case during cooldown are caused by the temperature gradients between the case side plates and the external stiffeners. The curvature produced in the stiffener by the temperature gradients causes high bending stresses in the case plate adjacent to the stiffener as

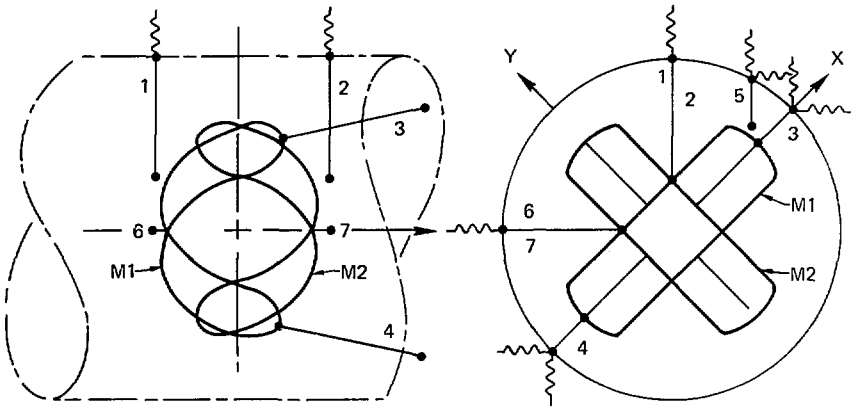

FIG. 72. GDSAP beam element model determines overall magnet stresses for seismic and cooldown thermal conditions.

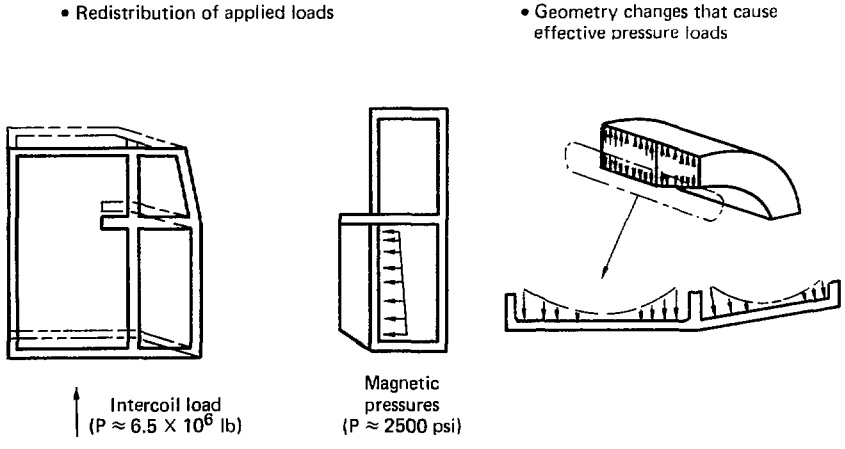

FIG. 73. Critical case stresses are caused by secondary bending moments.

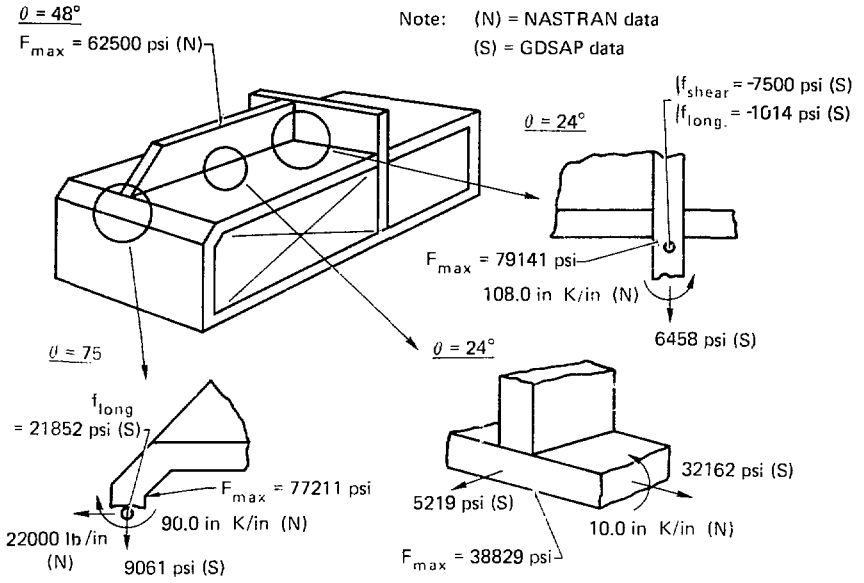

FIG. 74. The major radius stresses are less than 80 ksi.

shown in Fig. 75. However, these stresses do not exceed the yield strength of the structure at the temperature at which the stress occurs. The case stresses caused by the longitudinal thermal gradients did not exceed 12 ksi.

Minor Radius Analysis

The stresses in the minor radius are determined primarily by the GDSAP plate model. Membrane stresses are caused by the opening up of the minor radius due to magnetic loads, but 4.5 K operating thermal loads subtract slightly from these stresses. The secondary bending moments are due to redistribution of the intercoil load and to effective pressures caused by the case plate curvature as shown in Fig. 73.

Figure 76 shows the stresses at several locations in the case minor radius. The stresses were taken directly from the finite element analysis except for the secondary moments in the chamferred surface of the inner case plates. The secondary bending moment in that location was modified to account for inaccuracies in the finite element analysis caused by the constant strain triangular elements used in that portion of the model. The peak principal stresses predicted by the baseline analysis exceeded the intended 80-ksi design stress by 2 to 6% in both the inner and center crossover plates as shown in Fig. 76. However, an evaluation of several known inadequacies in the GDSAP analysis indicated that the predicted stresses would be reduced by a refined analysis of this area. The analysis refinement task

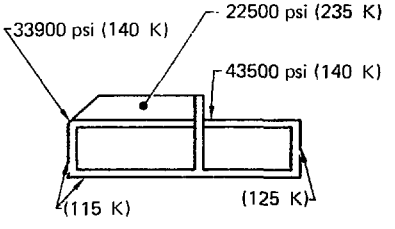

FIG. 75. Cooldown temperature gradients create significant stresses.

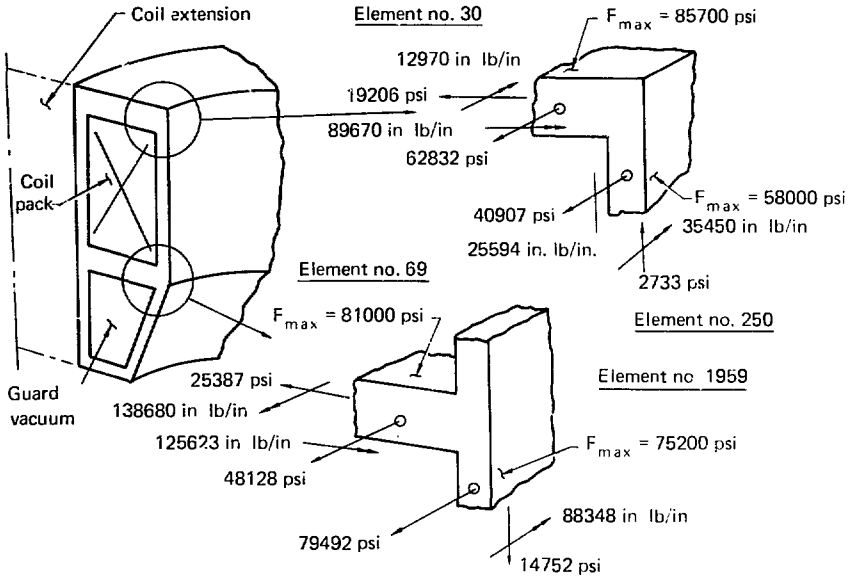

FIG. 76. The peak magnet stresses occur in the minor radius.

was accomplished and is discussed in a separate section of this report, and documented in Ref. 83.

Intercoil Structure Analysis

The intercoil structure connects the major lobe of one magnet with the minor radius of the other magnet. The primary stresses in the intercoil structure are caused by the normal operating magnetic loads that create a seven million pound compression load in the intercoil member. Additional low stresses are produced in the intercoil structure by thermal and inertia conditions.

Design loads for this structure were obtained from the large GDSAP plate model and from the smaller GDSAP beam model. Figure 77 shows the membrane stresses in the intercoil structure for the normal operating condition. Stresses for the normal operating thermal condition are less than 500 psi everywhere except in the inner plate near the major radius lobe where the values are shown in Fig. 77. Overall intercoil loads due to cooldown and inertia conditions obtained from the GDSAP beam model are superimposed on these stresses. It should be noted that the stresses should be multiplied by 1.25 to account for the difference between the 2.5-in. thickness used in the analysis and the 2.0-in. thickness used in the final design.

Support Structure Analysis

The support structure consists of two support rods (1,2) that support the weight of the magnet and five stabilizer rods (3–7) that react horizontal seismic loads as shown in Fig. 78. The struts and the lugs attaching the struts to the magnet were analyzed by hand to the loads shown in Table 19. Also shown in Table 19 are the margins of safety for various components in each support strut. The margins of safety are based on the following expression:

$$M.S. = \frac{F_{ALLOW}}{F_{APPLIED}} - 1 \quad , \qquad (a)$$

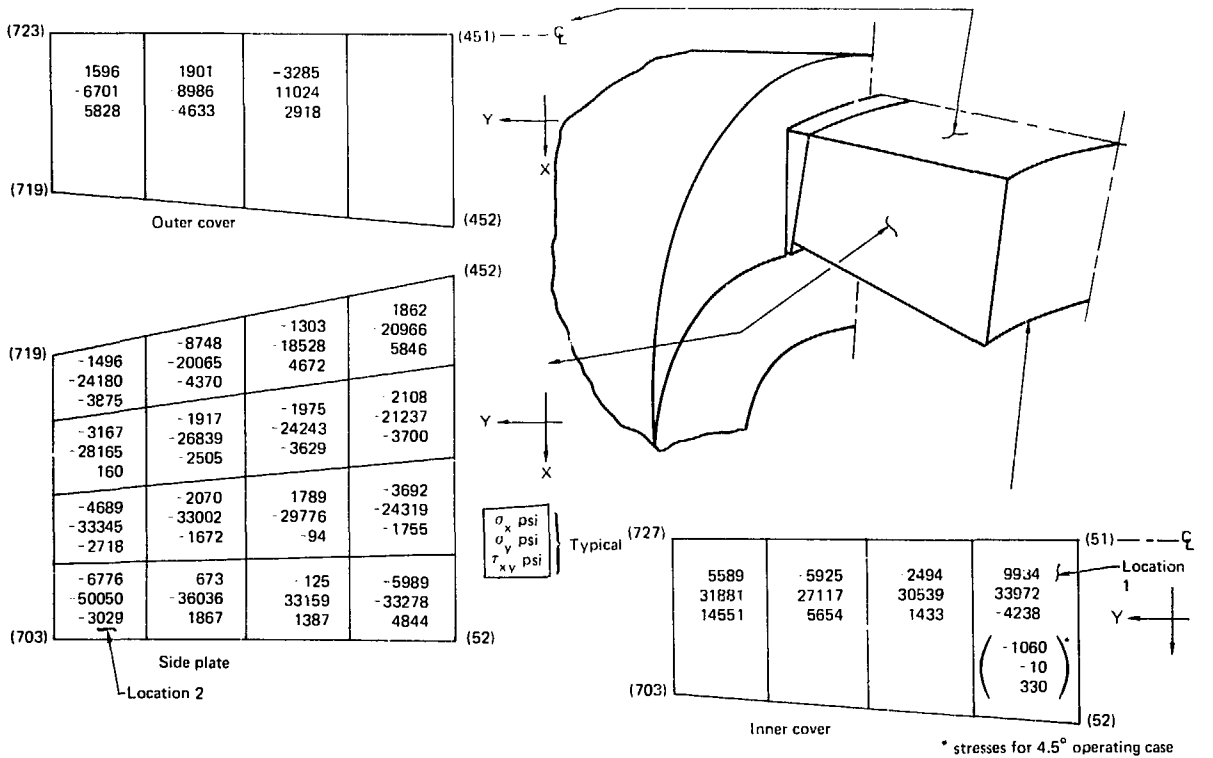

FIG. 77. The stresses in the intercoil structure are acceptable.

TABLE 19. Support struts have adequate margins of safety.

Rod No.	LLNL[a] load	Design load	Strut tension	Strut compression	Bearing capacity	Strut end lug	Clevis pin	Clevis lug
1	+687	+800						
	-	-375	+0.09	+0.95	+0.15	+0.10	+0.28	+0.52
2	+724	+800						
	-368	-375						
3	+518	+520						
	-237	-275	+0.68	+1.64	+0.17	+0.34	+0.99	+0.15
4	+424	+520						
	-263	-275						
5	+310	+375	+1.33	+0.95	+0.12	+0.33	+0.76	+0.15
	-183							
6	+359	+520	+0.68	+0.39	+0.17	+0.34	+0.99	+0.15
7	+242	+520						
	-505							

[a]Reference Telecon MFTF-5100-M-105 of 17 October 1978.

where

F_{ALLOW} is the lesser of

$$(F_{ty}/3) \times 1.2 = F_{tu}/2.5 \text{ and} \qquad (b)$$

$$(F_{ty}/1.5) \times 1.2 = F_{ty}/1.25 \quad . \qquad (c)$$

The lugs were checked for tension and shear-bearing failures using an industry-wide standard lug analysis documented in Lockheed Stress Memo No. 1. Bolts were checked for shear and bending failures. The struts themselves were checked for tension and for beam column compression loads. In compression, an initial bow of 1 in. was assumed in all rods.

FRACTURE ANALYSIS

A fracture analysis was performed in support of the MFTF design to confirm the selection of 304LN for the structural case material and to demonstrate adequate life at the 80-ksi design stress level.

A linear elastic fracture analysis of the 304LN plate and 316L weld filler was documented in Ref. 10. The analysis was based primarily on fracture toughness and flaw growth rate data obtained from NBS. Where data was not available, the analysis used material properties estimated from data for similar materials obtained from literature sources. The analysis was performed using the FLAGRO II analysis program, a linear elastic fracture mechanics program developed by Rockwell International Corporation.

The case parent material was analyzed for a typical surface flaw (0.150-in. long × 0.075-in deep) and for a typical corner flaw (0.050 × 0.050) at the edge of a penetration hole. A parametric study with various stress levels was made for both flaw configurations using NBS material data and the FLAGRO II analysis program. The analysis indicated that the required four design lives could be obtained with a stress level of 90 ksi in the basic plate material and with a stress level of 43 ksi at typical penetrations.

The 316L weld material was analyzed for typical surface flaws that were 0.150-in. long and 0.075-in. deep. However, during the baseline analysis, there was no flaw growth data available for this material. As it was felt that the characteristics of E310 filler would be very similar to those of 316L, the analysis was performed using E310 filler flaw-growth data. An analysis using 304LN flaw-growth data was also performed, resulting in design life stress of 90 ksi with 304LN flaw-growth data and 100 ksi with E310 data.

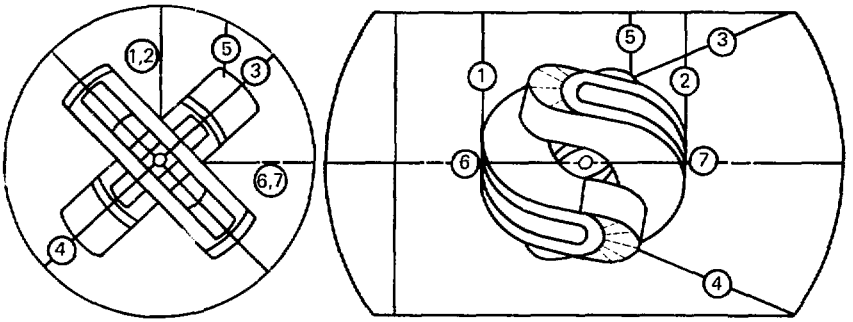

FIG. 78. MFTF supports are designed for magnetic, thermal, and seismic loads. (Rod Nos. 1 and 2 are support rods. Nos. 3–7 are stabilizer rods.)

CONCLUSIONS

The MFTF baseline analysis confirmed the basic structural integrity of magnet, and that the support system met ASME factor of safety criteria. Cooldown thermal stresses were acceptable for the cooldown time of 3.6 days which met design objectives. Fracture analyses showed acceptable magnet life at the design stress level of 80 ksi. Analysis showed that stress levels in the magnet were within the 80-ksi design limit everywhere except for several locations in the minor radius where peak stresses reached 86 ksi. A subsequent refinement of the finite analysis which is discussed elsewhere in this report and is documented in Ref. 83 reduced the calculated peak stress levels to less than 80 ksi.

SECTION 9
STRUCTURAL FINITE ELEMENT ANALYSIS REFINEMENT

SUMMARY

The baseline structural analysis of the MFTF magnet confirmed the structural integrity of the magnet. However, the peak stresses at several locations in the magnet mirror radius exceeded the allowable design limits of 80 ksi by 2 to 6%. These stresses were determined by a GDSAP finite element analysis and are documented in Ref. 10. It was recognized at the completion of the baseline analysis that a refined analysis of the critical stress region using the NASTRAN program would probably reduce the calculated peak stresses. Therefore, a revised finite element analysis of the MFTF magnet was conducted and documented in Ref. 83. This analysis incorporated a refined mesh, updated material thicknesses and a NASTRAN plate element that accounts for the out of plane shear flexibility not represented in the GDSAP analysis.

MODEL DESCRIPTION

For this analysis the case, jacket, and intercoil structure were modeled by isoparametric, quadrilateral, plate elements (Fig. 79). The conductor pack was modeled by "lumping" the stiffness of the individual conductor strands into six equivalent, continuous, axial rod elements. Rod elements in the

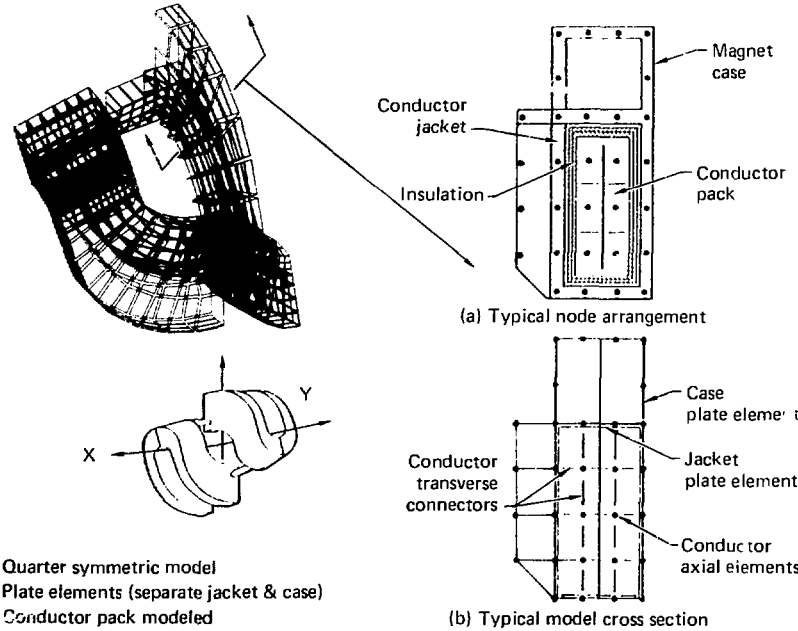

FIG. 79. Finite element model—typical cross section.

transverse directions were also included to model the conductor pack stiffness in those directions (Fig. 80).

The loading conditions analyzed included those loads due to electromagnetic forces, the residual thermal loads after cooldown to 4 K, the internal pressure load resulting from a quench, and the critical combination of normal operating electromagnetic loads and residual thermal cooldown loads. The electromagnetic load distribution was determined by LLNL and was proportioned according to the nodes of the conductor pack.

The structural analysis was accomplished in two steps. First, the baseline analysis (Ref. 79), using the GDSAP finite element program, identified those areas where peak stresses exceeded the 80-ksi allowable stress level. This allowable stress level accounts for a factor of safety of 1.5 on yield strength (120 ksi) for the 304LN case material. Regions of critical stress were found in the inner and intermediate crossover plates in the minor radius section.

The model refinements included: increasing the number of elements in the minor radius region, changing the case plate thickness from 3.00 in. to 3.20 in. (to account for the actual thickness of the received case material), and modeling the offset of the mid-surfaces at the transition from 3.20-in. to 5.00-in. crossover plate (at the transition from major to minor radius) (Figs. 81 and 82). Also, in addition to a GDSAP analysis, the model was analysed using the NASTRAN finite element program. NASTRAN accounts for transverse shear stiffness in plates and also utilizes some higher order elements. The refined model has fewer triangular elements than the baseline model and no highly distorted quadrilateral elements.

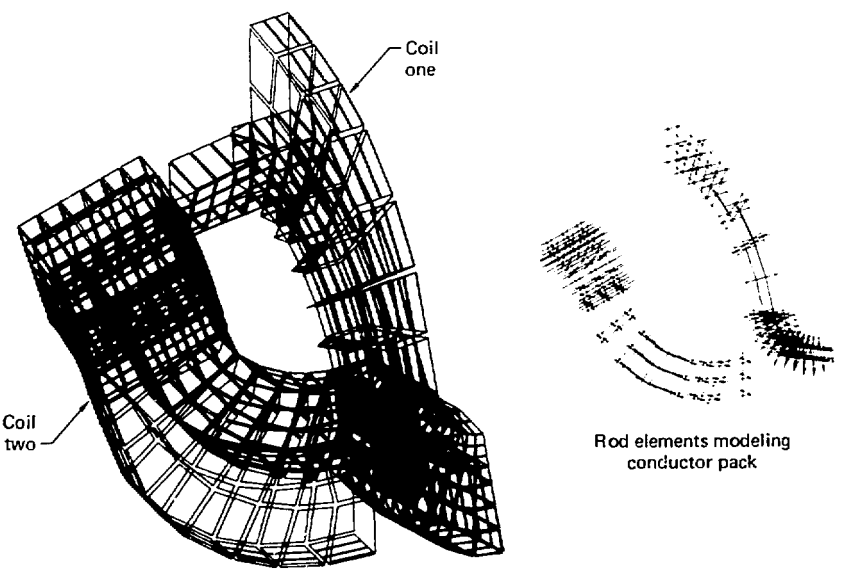

FIG. 80. Refined finite element model—case structure and conductor pack.

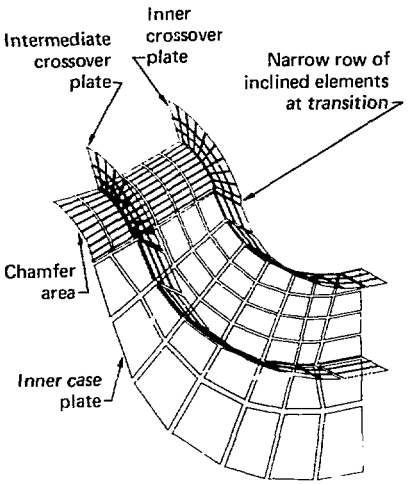

FIG. 81. Refined model accounts for nonalignment of neutral surfaces at transition from 3.2-in.-thick plate to 5.0-in.-thick plate.

ANALYSIS RESULTS

The maximum principal stresses predicted in the critical regions of the minor radius showed reductions of 3% to 8% for NASTRAN and 0% to 7% for GDSAP from those predicted by the baseline model. The largest stresses occurred with electromagnetic loading applied by itself.

For this loading the NASTRAN analysis found the peak principal stress of 81.5 ksi occurring at 45° from the axis of symmetry in the inner crossover plate of the minor radius (Fig. 83). This was the only location showing a stress larger than the 80-ksi allowable stress level for the NASTRAN analysis. The GDSAP analysis found stresses above 80 ksi over a 25° span with a peak stress of 83.4 ksi (Fig. 83). These stresses represent reductions of 7% by NASTRAN and 5% by GDSAP from the previously predicted peak principal stress of 88 ksi. GDSAP stresses also exceeded the 80 ksi level slightly for the intermediate crossover plate over a 10° span at the axis of symmetry with a peak stress of 81.5 ksi (Fig. 84). NASTRAN predicted all stresses below 80 ksi in this area.

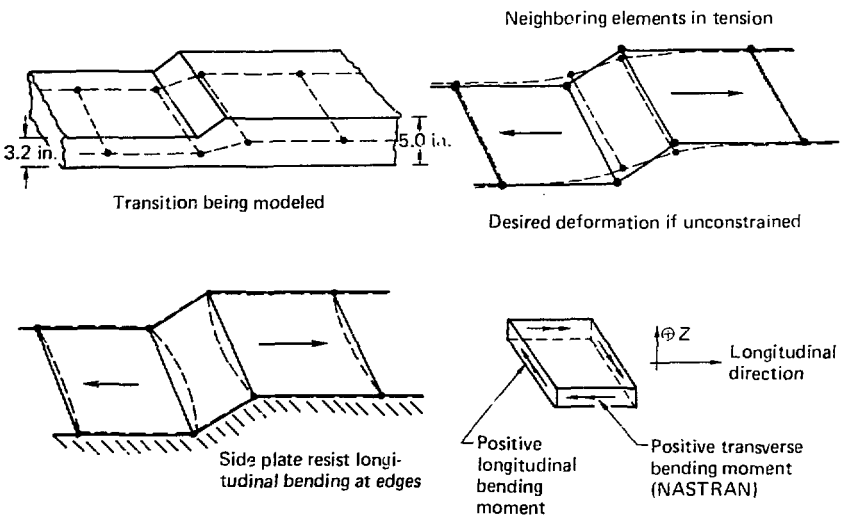

FIG. 82. Schematic of behavior at transition from 3.2-in. to 5.0-in. crossover plate.

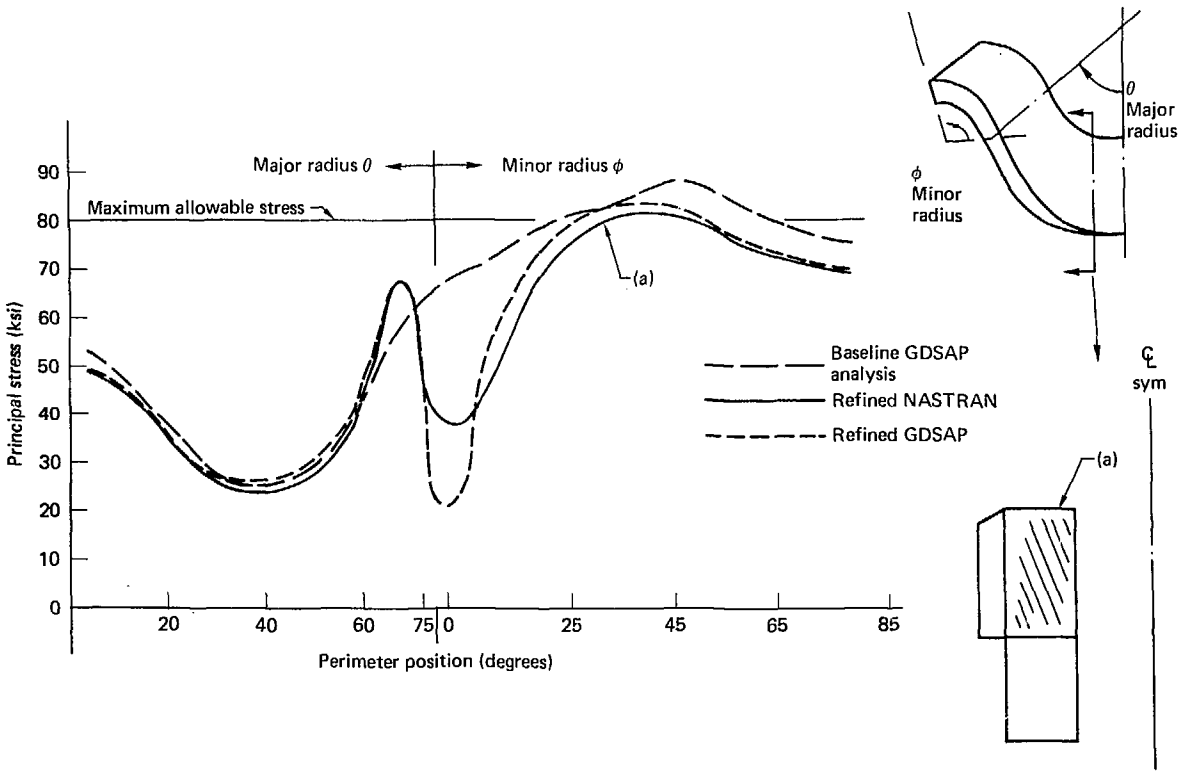

FIG. 83. Principal stress distribution—inner crossover plate—electromagnetic load only.

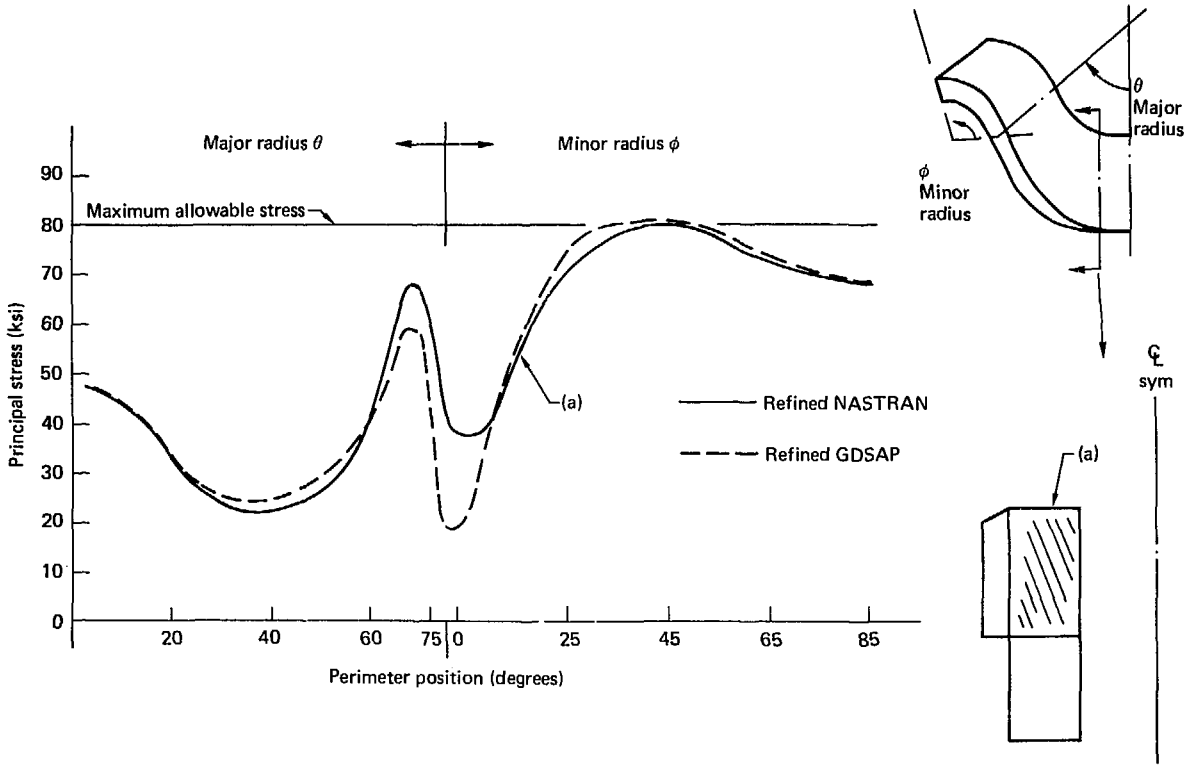

FIG. 84. Principal stress distribution—inner crossover plate—combined electromagnetic and residual thermal loads.

When the residual thermal loads due to the cooldown from room temperature to 4.5 K operating temperature are superimposed on the electromagnetic loads, a slight reduction of stresses is obtained (Figs. 85 and 86). It is important to note for this load combination that NASTRAN showed all stresses in the magnet to be below the 80-ksi design allowable stress level. GDSAP predicted a peak principal stress of 81.2 ksi, with a span of 10° in the inner crossover plate at stresses over 80 ksi (Fig. 85). The intermediate crossover plate, for this load combination, showed a peak principal stress of 80.6 ksi at the axis of symmetry (Fig. 86).

Discontinuities are evident in the stress distributions predicted with the refined model at the transition from 3.20-in.- to 5.00-in.-thick crossover plate material. These discontinuities had not shown up in the baseline analysis. The cause of the discontinuities was that the refined model accounted for the offset of the midsurfaces at the transition from 3.20-in. to 5.00-in. plate material. This offset, induces both longitudinal and transverse bending moments as is shown schematically in Fig. 82. These discontinuities, which are discussed in more detail in Ref. 83, were found to not have any critical effect on the stresses.

CONCLUSIONS

The refined finite element analysis verified the structural integrity of the MFTF magnet system with a factor of safety of 1.5 on yield stress for the 304LN case material. This verification is based on the NASTRAN finite element program for the worst compatible load case (normal operating condition) of electromagnetic plus residual thermal loading.

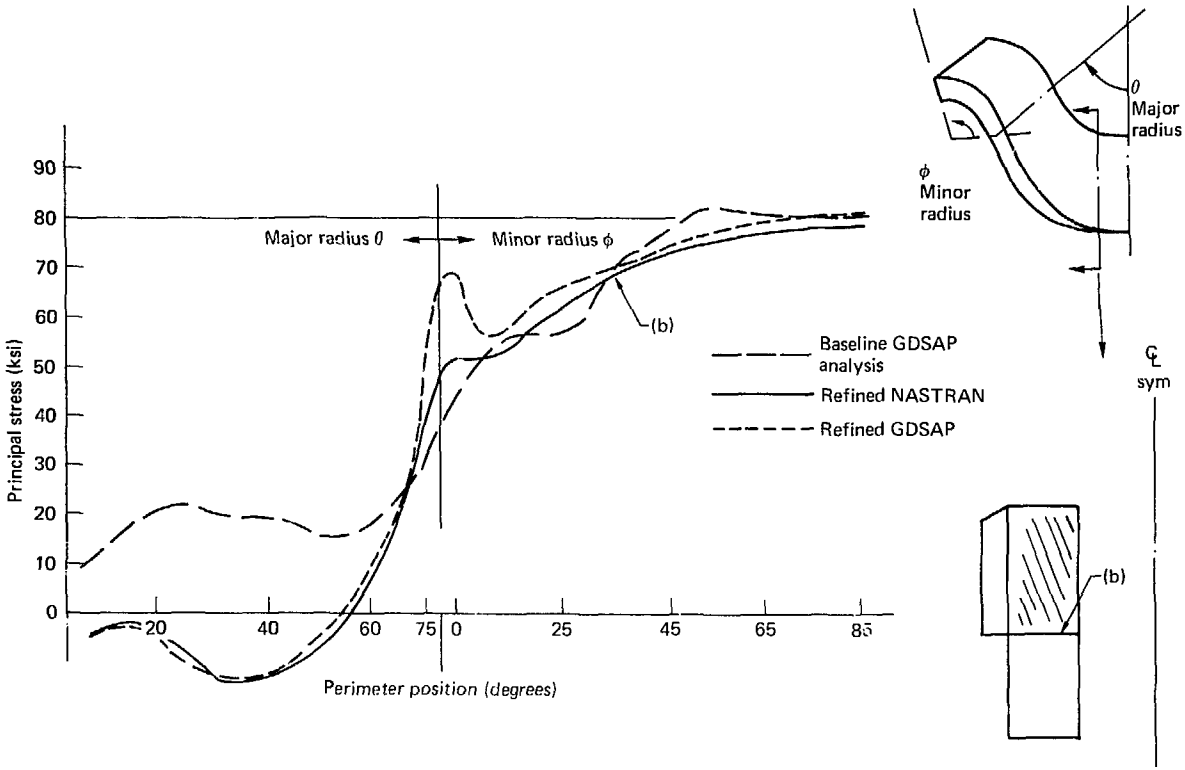

FIG. 85. Principal stress distribution on intermediate crossover plate--electromagnetic load only.

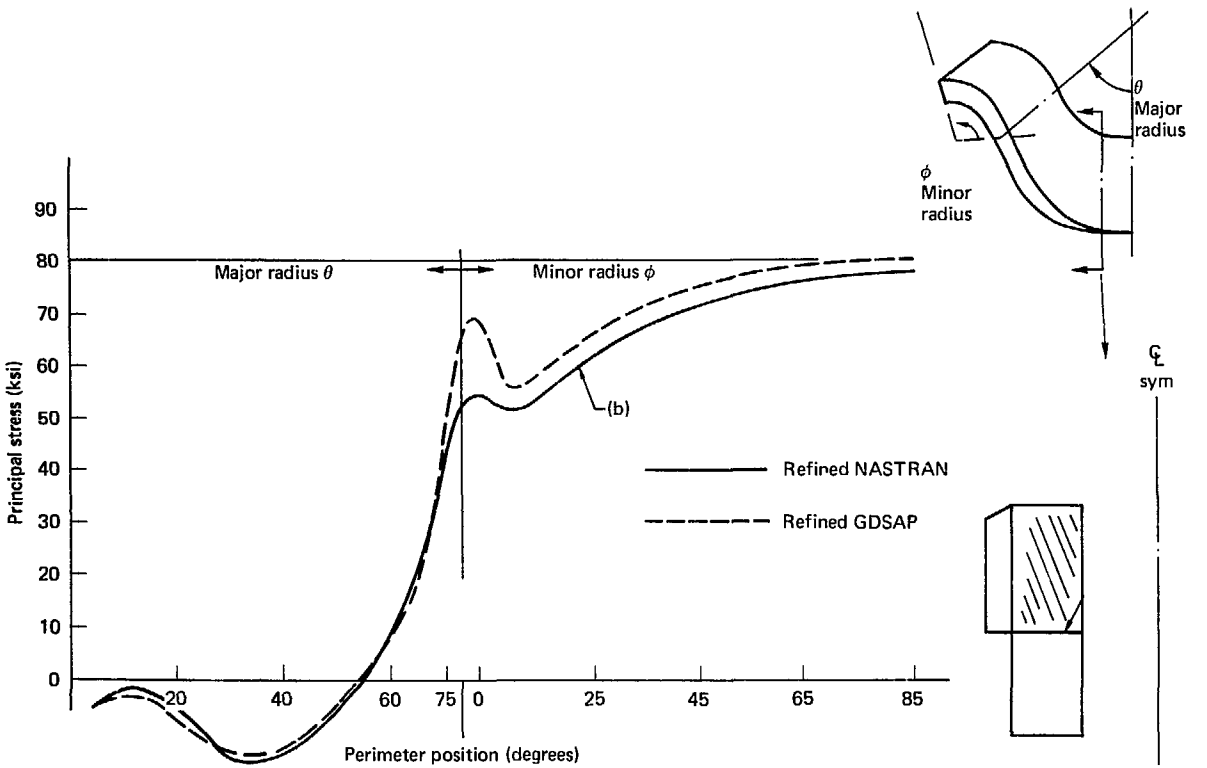

FIG. 86. Principal stress distribution on intermediate crossover plate—combined electromagnetic and residual thermal loads.

SECTION 10
STRUCTURAL CASE FAULT ANALYSIS

INTRODUCTION

A case fault analysis documented in Ref. 84 was performed to assess the criticality of selected failures in the magnet case, jacket and intercoil structure. The locations of the five failures selected for analysis were determined on the basis of the manufacturing processes, structural geometry and local stress levels at these locations and, ultimately, on the possible consequences of the failures. Since this task followed the program to confirm the structural integrity of the MFTF magnet case, jacket and shield system (Ref. 10), every effort was made to utilize analysis methods and tools developed earlier. The large, 7000-degree-of-freedom GDSAP model developed during that program was used extensively throughout this analysis task to determine the overall stresses and deflections in the vicinity of assumed faults. Subsequent to the finite element analyses, hand analyses were used to determine the stresses normal to the approaching fault front. Using this stress data a Mode I linear elastic fracture analysis was performed to quantify the criticality of each fault.

ANALYSIS METHODS

A common methodology was used to analyze each of the five selected faults. The analysis used the 7000-degree-of-freedom GDSAP model to determine the overall changes in stresses and deflections caused by the assumed faults. Data from this analysis was then used to determine the local stresses normal to the fault front and a simple Mode I linear elastic fracture analysis quantified the criticality of the faults.

The 7000-degree-of-freedom finite element model used in the fault analysis is basically the same as the model used in the original MFTF analysis and documented in Ref. 10. However, several minor changes that are documented in Ref. 84 were made to the model prior to the start of the fault analysis. The faults were simulated in the GDSAP analysis by additional nodes coincidental to existing nodes in the baseline finite element model and changing fault boundary plate connectivities. No attempt was made to refine the finite element mesh adjacent to the fault boundaries subsequent to the analysis. Model deflection data was used to calculate the local stresses normal to the assumed fault front.

A simple Mode I fracture analysis was performed using the stresses calculated from the finite element data to determine the criticality of the fault. The fracture analysis used the stress intensity solutions for a finite crack in an infinite plate and for a 0.5-in. edge crack in an infinite plate to approximate the stress intensities resulting from the faults. The expressions for the stress intensities in these cases are:

$K_I = \sigma\sqrt{\pi a}$ finite crack in infinite plate (Ref. 85)

$K_I = 1.1215\sigma\sqrt{\pi a}$ 0.5-in. edge crack in infinite plate (Ref. 85)

where σ = nominal stress, normal to fault, and
a = half-crack length.

The stress intensities resulting from the analysis were compared to the plane-strain fracture toughness (K_{IC}) data used in the original MFTF fracture analysis. This data is shown in Table 20.

ANALYSIS RESULTS

A total of five fault conditions were analyzed during this study. Isometric sketches, selection rationale, and analysis results are summarized below for each of the following faults:

1. Minor radius intermediate 3- to 5-in. plate intersection in the chamfer region at center line of symmetry.
2. Conductor pack jacket close-out weld in the major-to-minor radius transition.
3. Intercoil member shear transfer weld, bottom closure plate to side plate corner weld.
4. The 3-in. close-out weld at the center line of symmetry in the minor radius at the bottom of the 9 section.
5. The 3- to 5-in. transition butt weld joint at the major to minor radius transition on the conductor case top plate.

Fault number 1 is shown in Fig. 87 along with the rationale for selecting it for analysis. In the finite

TABLE 20. Fault fracture analyses were based on preliminary material data used during the MFTF design.

Material	Case-material fracture-analysis properties			
	Temp., K	F_{ty}, ksi	K_{IC}, ksi $\sqrt{in.}$	da/dn flow growth rate, in./cycle
304LN (0.12% N)[a]	4.5	111.8	203	$1.054 \times 10^{-4} (\Delta K)^{3.59}$
E316L weld filler				
ΔFe = 4.5[a]	4.5	116	110	Not available
ΔFe = 9.2[a]	4.5	128	95	Not available
E 310-16 weld filler[b] (AISI 310S, SMAW)	4.2	120	106	$4.98 \times 10^{-8} (\Delta K)^{5.15}$

[a]Source: see Ref. 86.

[b]Source: see Ref. 87.

element analysis, coincident grid points were installed at the chamfer region. Continuous connectivity was provided for in the 3-in. plate, while connectivity in the 5 in. was interrupted throughout a 20° arc (approximately 6.82 in.).

Analysis of the 5-in.-plate deflection data indicates that the stress field normal to the approaching fault front is approximately 25,880 psi, neglecting bending. Assuming an infinite plate with a finite crack,

$$K_I = 25880\sqrt{6.82\pi} \text{ psi}\sqrt{\text{in.}} \quad . \qquad (10)$$

Based on the baseline analysis reported K_{IC} value for E 316 weld filler ($\Delta Fe = 9.2$) at 4.5°K of 95 ksi $\sqrt{in.}$, a comparison of calculated and critical stress intensity values indicates that this fault would continue to propagate under static loading until a lower stress field is encountered or a crack arrest mechanism is encountered. However, current NBS testing predicts a minimum fracture toughness in the weld metal of 140 ksi $\sqrt{in.}$ Based on this data, the assumed fault would not propagate under static loading but would continue to grow under cyclic loads until failure.

Fault number 2 and its selected rationale are shown in Fig. 88. For the analysis of fault number 2, coincident grid points were installed in the model along the entire 0.5-in. plate "L" section. It was assumed that the transition from 0.5-in. to 1.0-in. jacket plating would act as a crack arrest mechanism. Continuity was provided for an all case plating while continuity of the 0.5-in. jacket plate was interrupted at the plane in question.

Evaluation of the finite element analysis results indicates that the peak tension stress normal to the assumed fault occurs at the bottom of the "L" section where the stress is 40,200 psi. This stress results in a Mode I stress intensity of:

$$K_I = 50 \text{ ksi}\sqrt{\text{in.}}$$

Because this stress intensity is less than the predicted K_{IC} for the 316 plate material, this fault would not propagate statically. The fault would propagate to failure under cyclic loading. But, the analysis indicates that a total failure of the jacket plate would have little effect on the overall structural case stresses.

Fault number 3 is illustrated in Fig. 89. For the analysis of this fault, the finite element model was modified by installing coincident grid points along the intercoil member fault corner. The plate connectivity was altered so there could be no load transfer between the bottom and side plate locally along the fault perimeter.

The analysis results indicate very little redistribution of stress as a result of the assumed failure. Because the stresses were primarily compression, however, the failure mode of concern was not Mode I fracture. The primary concern was the precipitation of an instability failure in the large plates. However, an updated stability analysis of the intercoil plates with revised boundary conditions to simulate the cracked weld predicted buckling failure stresses in excess of the peak intercoil stresses. Based on this analysis, there were no significant effects due to the assumed fault.

Selection rationale

- Weld joint
  - Complex unbalanced weld-on-weld joint
  - Heat sink gradient
- Joint geometry
  - Chamfer region increases welding difficulty but has no significant effect on gross stress distribution
- Stress
  - Plate membrane stresses parallel to this weld joint approach 80 ksi
  - Principal stresses in the 5-in. plate approach 80 ksi
- Concern
  - Loss of the 5- to 3-inch joint (basically a shear transfer member) may result in excessive case deflection and subsequent conductor pack crushing

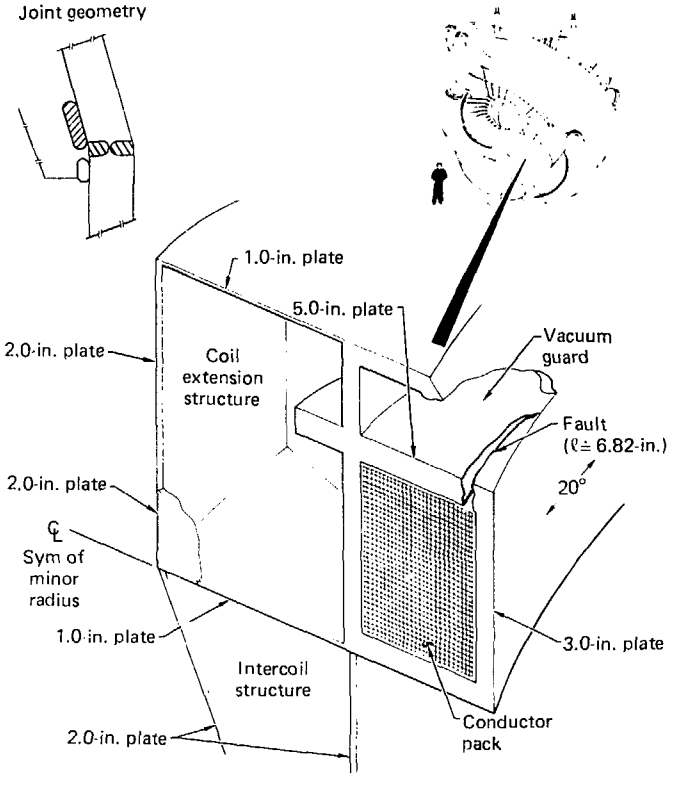

FIG. 87. Fault No. 1: minor radius intermediate 3- to 5-in. plate intersection in the chamfer region at the centerline of symmetry.

Selection rationale

- Weld joint
  - Close-out weld increases weld inspection difficulty
- Joint geometry
  - Joint oriented normal to significant plate membrane stresses
- Stresses
  - Principal stresses in the area of the joint approach 50 ksi
- Concern
  - Decreased weld inspectability increases probability of potentially critical flaw existing
  - Previous stress analysis assumed that the jacket plating contributed to the case stiffness. Jacket failure will increase the primary case plate stresses

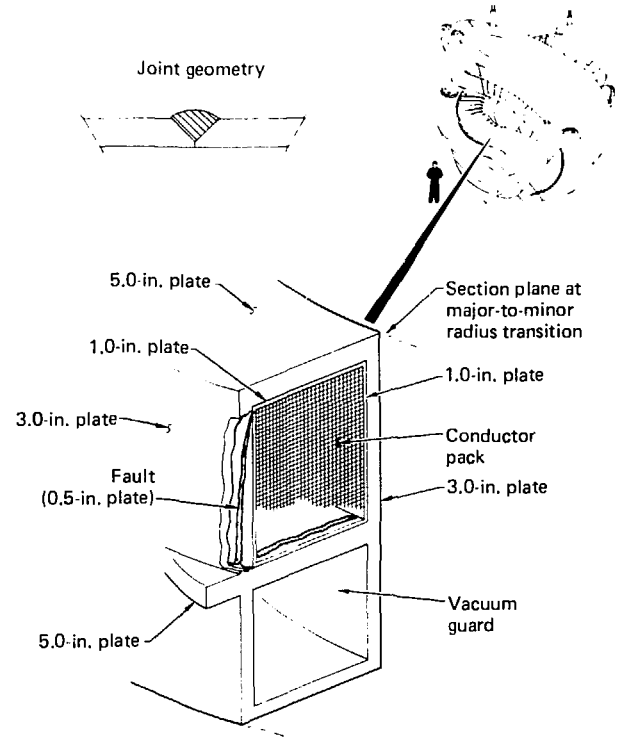

FIG. 88. Fault No. 2: conductor pack jacket close-out weld in the major-to-minor radius transition.

Selection rationale

- Weld joint
  - Joint geometry - no significant effect
- Stress
  - Compressive only
- Concern
  - Loss of joint may cause intercoil member instability and system catastrophic failure

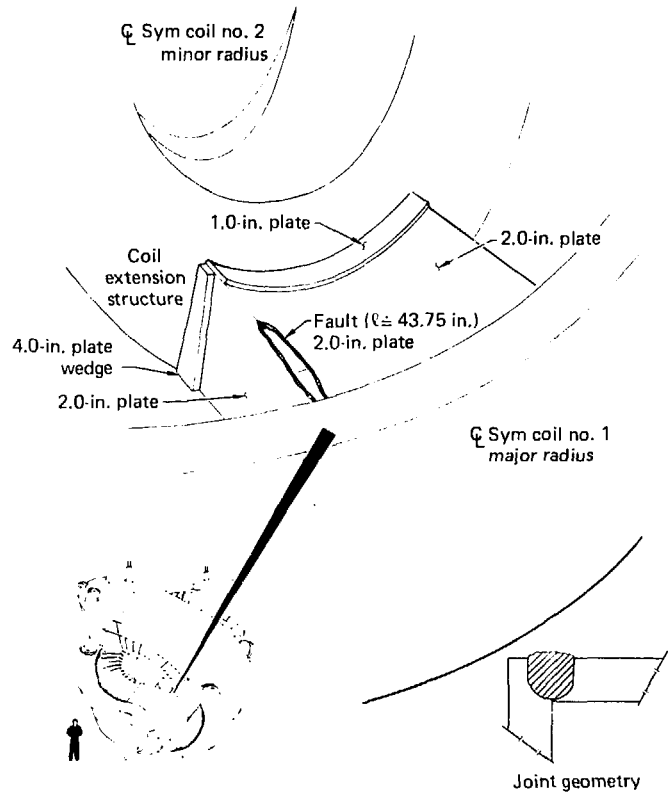

FIG. 89. Fault No. 3: intercoil member shear transfer weld, bottom closure plate to side plate corner weld.

Fault number 4, which is shown in Fig. 90, was assumed to extend from the minor radius center line of symmetry through a 20° arc (half length = 6.82 in.). Coincident grid points were installed in the baseline model along existing fault line grid points. Continuity of the 3- to 5-in.-plate joint was interrupted by redefining existing CQUAD element grid point connectivities.

Deflection data near the approaching fault front was extracted from the computer output for use in a Mode I fracture analysis. From this deflection data the local plate membrane stress was determined to be approximately 5,667 psi. From linear plastic mechanics theory, for an infinite plate with a finite center crack,

$$K_I = 5667\sqrt{6.82\pi} = 26.23 \text{ ksi}\sqrt{\text{in.}} \qquad (11)$$

This stress indicates that although this crack is not catastrophic, it will continue to propagate under cyclic loading until failure or a crack arrest mechanism is encountered.

Fault number 5 was the most critical of the five failures that were analyzed. The fault, which is shown in Fig. 91, caused a significant reduction in the overall bending strength of the magnet case in the minor radius and a resulting increase in stress. The finite element results indicated a significant increase in stresses approached 99,300 psi. At this stress level, the stress intensity for a 5-in. edge crack in an infinite plate is:

$$K_I = 1.22 \times 99300\sqrt{2.5\pi} = 340 \text{ ksi}\sqrt{\text{in.}} \qquad (12)$$

This K_I reflects a catastrophic failure when compared to the critical stress intensities for 304LN and 316L welds.

CONCLUSIONS

Results of this study are summarized in Table 21. Of the five conditions analyzed, one is considered to have structurally catastrophic effects; catastrophic meaning these faults would be reflected by sudden and violent changes in the geometry of the structure. The fault considered structurally catastrophic (Mode I analysis) was Fault No. 5 (the 3- to 5-in. transition butt weld joint at the major-to-minor radius transition on the conductor case top plate).

Fault number 4, the 3-in.-plate close-out weld at the center line of symmetry in the minor radius at the bottom of the 9 section, is considered to be

TABLE 21. Case fault analysis summary.

Fault	Fault description	Calculated	Discussion
1	Minor radius intermediate 3- to 5-in.-plate intersection in the chamfer region at the center line of symmetry	120 ksi $\sqrt{\text{in.}}$	K_I equals K_{IC}. Fault will be self propagating. Catastrophic failure assumed.[a]
2	Conductor pack jacket close-out weld in the major-to-minor radius transition	50 ksi $\sqrt{\text{in.}}$	K_I lower than K_{IC}. Fault will propagate under cyclic loading. Overall system integrity not significantly affected.
3	Intercoil member shear transfer weld, bottom closure plate to side plate corner weld	M.S. = 1.17	M.S. calculated assuming compressive-yield allowable of 120 ksi.
4	3-in.-plate close-out weld at the center line of symmetry in the minor radius at the bottom of the 9 section	26 ksi $\sqrt{\text{in.}}$	K_I lower than K_{IC}. Fault will propagate under cyclic loading.
5	3- to 5-in.-transition butt weld joint at the major to minor radius transition on the conductor case top plate	441 ksi $\sqrt{\text{in.}}$	K_I higher than K_{IC}. Fault will be self-propagating. Catastrophic failure assumed.

[a]Updated fracture mechanics data ($K_{IC} \approx 140$ ksi $\sqrt{\text{in.}}$) indicates that this fault is not initially catastrophic. However, it will propagate quickly under cyclic load to the failure point.

Selection rationale

- Weld joint
  - Close-out weld; increases weld inspection difficulty
- Joint geometry
  - Not significant
- Stress
  - Moderate plate longitudinal membrane stress
- Concern
  - Decreased weld inspectability increases *probability of potentially* critical flaw existing. Joint failure and subsequent redistribution of stresses may result in excessive deflections and conductor pack crushing

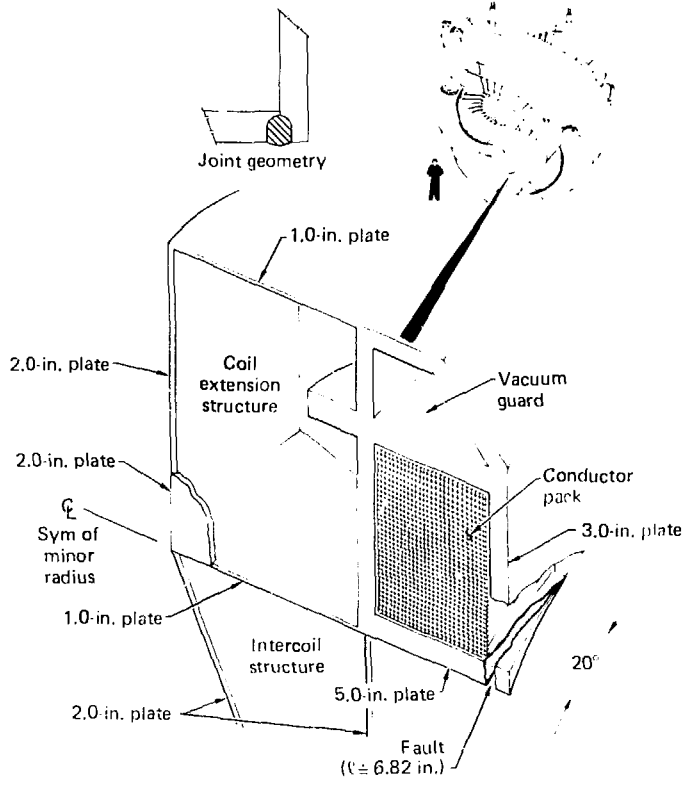

FIG. 90. Fault No. 4: 3-in. plate close-out weld at the centerline of symmetry in the minor radius at the bottom of the 9 section.

Selection rationale

- Weld joint
  - One sided butt joint (unbalanced)
  - Weld bead reinforcement (K_T)
  - Heat sink gradient
- Joint geometry
  - 3- to 5-inch plate transition produces local stress raiser
- Stress
  - Plate membrane stresses normal to this joint approach 60 ksi
  - Transverse secondary bending moments approach 95 in.- kips/in.
- Concern
  - Joint failure causes a significant reduction in magnet section modules resulting in redistribution of stresses and possible system catastrophic failure

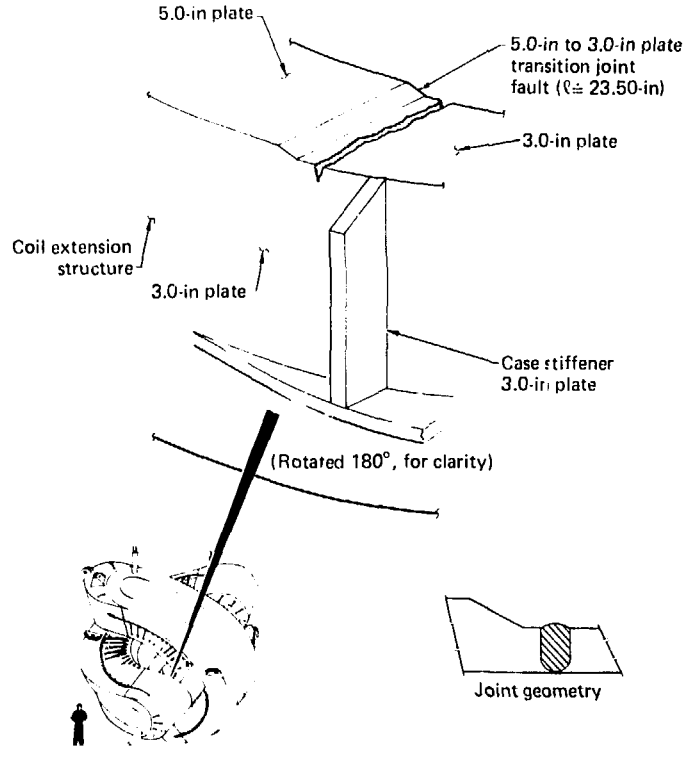

FIG. 91. Fault No. 5: major-to-minor radius transition, 3-in. to 5-in. butt-weld joint on the conductor case top plate.

potentially catastrophic; i.e., the calculated stress intensity factors are lower than the critical stress intensity factor but under cyclic loading this fault will continue to propagate until repaired or a suitable crack arrest mechanism is encountered.

Fault number 1, the 3- to 5-in.-plate intersection in the chamfer region of the minor radius, is potentially catastrophic, even with updated NBS fracture toughness data. At the calculated K_I of 120 ksi $\sqrt{in.}$, the stress intensity is less than the K_{IC} of 140 ksi $\sqrt{in.}$ measured for the 316L weld. This indicates that the fault would not fail immediately but would continue to grow under cyclic load until failure.

SECTION 11
STRUCTURAL METALLURGY

INTRODUCTION

Following the Baseball II magnet experience Nitronic 40 was first selected for the MFTF magnet structure. However, plate of sufficient size was unavailable, and welding across major stress planes was necessary. Accordingly, an effort was made to develop a weld procedure using Inconel 625: a nickel-base alloy, which, it was hoped, could match the parent metal strength and toughness. Because poor fracture toughness of both the Inconel 625 weld and the Nitronic 40 base metal precluded design stresses above 80 ksi, it was decided to abandon the this approach and use a tougher and less expensive austenitic stainless steel, 304 LN, with a ferrite-free 316L weld metal. In this section the experience with both base-metal systems are described.

INITIAL WELD DEVELOPMENT

Initial weld development programs were oriented toward development of procedures to join Nitronic-40 stainless steel for the case structural material, whose nominal composition is Fe-21%Cr-6%Ni-9%Mn (Refs. 87–90). Fusion-welding of thick sections of this alloy (thicker than 1/4-in.) had been greatly hampered by the inability to develop a weld filler metal that matched both the base metal's high yield strength ($\geq$180 ksi) and moderate fracture-toughness ($\approx$75 ksi $\sqrt{\text{in.}}$) at 4 K (Refs. 87-90). The filler metals selected for evaluation were a modified Nitronic 40, with nominal composition Fe-20%Cr-7%Ni-9.5% Mn, and a nickel-base alloy, known as "Alloy 625," with nominal compositions Ni-22%Cr-9%Mo-3.5%Cb-3.5% Fe. The latter material was selected on the basis of its known good 77 K ductility as a weld filler-metal for joining both stainless steels and nickel-base alloys (Ref. 91). Welding processes evaluated were shielded-metal arc (SMA), gas-metal arc (GMA), gas-tungsten arc (GTA), and submerged arc (SA). All four processes were evaluated using the Alloy 625 filler, while modified Nitronic filler was used with the GMA and GTA processes.

MODIFIED NITRONIC-40 FILLER METAL

Details of welding are presented in Ref. 92 and summarized in Table 22 of this report [see information tabulated for welds No. 1 (GMA) and No. 2 (GTA)]. Weld-metal chemical compositions were typical for this material (Table 23). Weld-metal Charpy V-notch impact tests performed at 77 K were used as a screening tool to avoid extensive and expensive 4 K testing of many specimens. Results of 77 K charpy impact tests are presented in Table 24. Average energy absorption values were 17.5 ft-lb for the GTA weld and 27.0 ft-lb for the GMA weld, as compared with typical annealed-base metal values of 60–70 ft-lb at 77 K (Ref. 90). Microscopic examination of both welds showed the usual duplex austenite-ferrite microstructure with ferrite contents of 4.5% for the GMA weld and 8% for the GTA weld. The disappointing 77 K Charpy V-notch impact performance confirms the SMA results presented at the October 1977 Vail Workshop on Structural Materials for Low Temperature Service, (Ref. 90), and further work on evaluation of modified Nitronic-40 weld metal was discontinued in favor of increased efforts on the Alloy 625 weld metal.

ALLOY 625 WELD METAL

Details of weld manufacture and resulting chemical composition, microstructure, and mechanical-property performance are discussed in detail in Refs. 93 and 94 and summarized in Tables 22 through 26 of this report (see information tabulated for welds Nos. 3–6 for the SMA, GTA, GMA, and SA welds, respectively). Welds were made in 2-in.-thick Nitronic-40 plate, heavily-restrained by welding the free edges of the plates to a 4 to 6-in.-thick steel plate, to simulate the high degree of restraint that would be imposed on weldments in the actual case structure. Chemical compositions were usual for Alloy 625 weldments (Table 23). Welds were evaluated for soundness by radiography, which revealed no unacceptable

TABLE 22. Welds made in the multiprocess study.

Weld No.	Process	Flux or shielding gas	Electrode					Weld joint			Base metal
			Filler	Diam (in.)	Supplier	Heat No.	Lot No.	Type	Origin	Position	
1	Gas-metal arc	Argon + 2% O_2	Nitronic 40	0.030	Armco	91520		Double-V	LLNL	Flat	Nitronic 40
2	Gas-tungsten arc	Helium	Nitronic 40	0.030	Armco	91520		Double-V	LLNL	Flat	Nitronic 40
3	Shielded-metal arc		Alloy 625	5/32	Inco			Butt	LLNL	Flat	Nitronic 40
4	Gas-tungsten arc	Helium	Alloy 625	1/8	Inco	NX 8511		Butt	LLNL	Flat	Nitronic 40
5	Gas-metal arc	Argon + 2% O_2	Alloy 625	1/16	Inco	NX 7478		Butt	LLNL	Flat	Nitronic 40
6	Submerged arc	Arcos N82	Alloy 625	1/16	Inco	NX 7478		Butt	LLNL	Flat	Nitronic 40
8	Gas-metal arc	Argon + 2% O_2	316L	1/16	Unibraze	IF2-9201047		Butt	LLNL	Flat	304 LN
9	Submerged arc	Hobart HS300	316L	3/32	Johnson	17222		Butt	LLNL	Flat	304 LN
10	Flux-cored arc		316 LT-3	3/32	Stoody	0388		Butt	LLNL	Flat	304 LN
11	Electroslag	Arcos N82	Alloy 625	1/16	Inco	NX 7990		Butt	LLNL	Vertical	304 L
12	Electroslag	Arcos N82	316L	3/32	Unibraze	IF2-8311246		Butt	LLNL	Vertical	304 L
13	Electroslag	Arcos N82	316	3/32	Unibraze	IF2-8311246		Butt	LLNL	Vertical	304 LN
17	Pulsed gas-metal arc	75% He/25% Ar	2RM69	1/16	Sandvik	743802		Double-V	CBI-Hstn	Vertical	304 LN
20	Pulsed gas-metal arc	75% He/25% Ar	316L	0.045				Double-U	FMC San Jose	Flat	304 LN
21	Electroslag	Hobart PT203	316L	3/32	McKay	04634	31821	Butt	FMC San Jose	Vertical	304 LN

TABLE 23. Chemical composition of welds made in the multiprocess study (wt%).

Weld No.	Process	C	Mn	Si	S	P	Cr	Ni	Mo	Ti	Cb+Ti	N_2	Other
1	Gas-metal arc	0.017	9.52	0.14	0.007	0.012	19.93	7.17					
2	Gas-tungsten arc	0.017	9.52	0.14	0.007	0.012	19.93	7.17					
3	Shielded-metal arc	0.046	0.25	0.58			21.48	Bal.	8.85	0.06	3.60	0.05	Al:0.04, Fe:3.06
4	Gas-tungsten arc	0.05	0.09	0.28	0.002	0.010	22.13	61.68	8.87	0.22	3.33	0.08	B:0.001, Fe:3.06, Al:0.28
5	Gas-metal arc	0.02	0.24	0.14	0.004	0.012	21.90	60.34	9.56	0.27	3.39	0.04	Fe:3.91, Al:0.21
6	Submerged arc	0.02	0.24	0.14	0.004	0.012	21.90	60.34	9.56	0.27	3.39	0.05	B:0.001
11	Electroslag	0.05	0.40	0.30			20.90	48.40	6.80	0.15	.70	0.08	Al:0.15, Fe:19.50
12	Electroslag	0.030	1.70	0.48			18.70	12.70	2.10				
13	Electroslag	0.015	4.60	0.17	0.007	0.010	24.76	21.48	2.14				
17	Pulsed gas-metal arc												
20	Pulsed gas-metal arc												

TABLE 24. Charpy V-notch impact performance at 77 K at welds made in the multiprocess study.

Weld No.	Process	Ferrite number		Energy absorbed		Lateral expansion	
		Vender	LLL	Average,[a] ft lb	Range, ft-lb	Average[a], mils[b]	Range, mils[b]
1	Gas-metal arc		4.5	17.5	16.5 – 18.5	6.0	4.0 – 8.0
2	Gas-tungsten arc		8.0	27.7	24.5 – 31.0	12.5	12.0 – 13.0
3	Shielded-metal arc			37.0	37.0 – 37.0	31.2	29.5 – 32.8
4	Gas-tungsten arc			45.3	43.0 – 46.0	41.4	36.7 – 46.8
5	Gas-metal arc						
6	Submerged arc			70.6	19.5 – 21.5	18.9	12.8 – 24.6
8	Gas-metal arc		5.5	26.8	23.1 – 30.0	19.5	16.6 – 23.4
9	Submerged arc		5.5	26.9	21.5 – 31.0	13.9	10.8 – 18.4
10	Flux-cored arc		13.0	14.1	9.8 – 17.9	8.7	4.6 – 11.6
11	Electroslag			88.0	71.0 – 111.0	57.3	51.0 – 66.4
12	Electroslag			95.4	80.2 – 110.5	75.2	63.6 – 75.4
13	Electroslag			103.0	95.0 – 111.0	50.8	44.0 – 57.5
17	Pulsed gas-metal arc	0		68.2	63.0 – 79.0	55.0	49.0 – 63.0
20	Pulsed gas-metal arc		8.5	35.9	31.0 – 42.5	22.1	19.0 – 28.6
21	Electroslag		5.0	34.9	28.0 – 41.5	30.4	24.2 – 38.0

[a]Average of 3 to 5 specimens.

[b]1 mil = 0.001 in.

TABLE 25. 4 K tensile and fracture-toughness properties of welds made in multiprocess study.

Weld No.	Process	Ultimate strength, ksi	Yield strength, ksi	Elongation, %	Reduction in area, %	K_Q,[a] ksi $\sqrt{in.}$
3	Shielded-metal arc	183.0[b]	127.0	30.7	25.0	122.8
4	Gas-tungsten arc	173.3[b]	138.0	18.0	15.0	121.3
5	Gas-metal arc	157.7[b]	121.0	22.7	26.7	136.0
9	Submerged arc	157.9[b]	97.2	60.0	39.0	101.0
11	Electroslag	107.1[b]	82.6	11.0	14.0	
12	Electroslag	204.1[b]	74.7	39.9	26.2	146.0
13	Electroslag	200.1[c]	65.1			
20	Pulsed gas-metal arc	200.5[b]	118.3	48.0	38.5	
21	Electroslag	170.1[b]	96.2	35.0	20.4	
		193.7[c]	85.8	35.0	27.9	
		183.5[d]	75.6	30.5	26.4	

[a]K_Q is an invalid, nonconservative, measure of fracture-toughness due to inadequate specimen thickness or improper test procedure.

[b]L—Longitudinal, parallel to weld axis.

[c]LT -Long transverse, across weld axis.

[d]ST—Short transverse, through weld axis.

TABLE 26. 4 K mechanical properties of 2-in.-thick Nitronic 40 plate used in the alloy 625 welding study.

	Ultimate tensile strength, psi	0.2% offset yield strength, ksi	Elongation in 1 in., %	Reduction in area, %	Fracture-toughness	
					Longitudinal,[a] K_Q	Transverse, ksi $\sqrt{in.}$
	245	198	22	35	138	175
	251	195	26	30	130	136
	245	196	20	25	131	132
Average	247.0	196.3	22.7	30.0	133.0	131.0

[a] K_Q is a nonconservative value of fracture-toughness, i.e. $K_Q > K_{IC}$, the minimum-value or "plane-strain fracture-toughness," caused by the specimen thickness of 0.5 in. being less than that required to ensure attainment of plane-strain conditions at the crack-tip during testing.

defects, and by room temperature side-bend testing, which places the entire thickness of a slice cut through the weld in tension. Side-bend specimens cut from SMA, GTA, and SA welds were bent around a 2t (t = specimen thickness) radius mandrel to an angle of 180° without any evidence of failure. However, the GMA side-bend specimens failed at a bend angle of about 30°. Both microscopic examination and chemical analysis of the failed GMA bend-test specimens failed to reveal any cause for this poor performance. Post-weld heat-treatment (PWHT) of another GMA bend specimen at 2150°F for 1 h, followed by testing as described above, resulted in this specimen passing the side-bend test. This indicated that the cause of premature failure of the as-welded GMA specimens was associated with the presence of a metallurgical-phase formed during solidification and/or during cooling to room temperature after welding, and that this phase could be removed or rendered innocuous by a high-temperature PWHT. However, such a PWHT is not practical during assembly of the massive case sections, and is certainly not a practical treatment on the case close-out welds once the magnet was sealed inside the case.

Low temperature evaluation of the Alloy 625 weldments consisted of 77 K Charpy V-notch impact tests (Table 24) and 4 K tensile and fracture-toughness tests (Table 25). Notches in the charpy specimens and cracks in the fracture-toughness specimens were oriented so that the cracks propagated from the top to the bottom of the weld metal. Average Charpy V-notch test energy absorption values were 37 ft-lb for the SMA weld, 45.3 ft-lb for the GTA weld, and 20.6 ft-lb for the SA weld. While below the 60 ft-lb value for unwelded Nitronic 40 (Ref. 90), results for the SMA and GTA welds represented a distinct improvement over 77 K Charpy V-notch test energy-absorption values shown by the modified Nitronic 40 weld metal (Table 24).

Tensile test results at 4 K of the Alloy 625 weld metals are summarized in Table 25 and of the Nitronic-40 base metal in Table 26. All materials exhibited satisfactory values of tensile ductility, with average elongation values for the base metal and SMA, GTA, and GMA weld metals of 22.7%, 30.7%, 18.0%, and 22.7%, respectively. Average tensile yield strength values of the base metal and SMA, GTA, and GMA weld-metals were 196.3 ksi, 127.0 ksi, 138.0 ksi, and 121.0 ksi, respectively. Scanning electron microscopy examination of the fracture surfaces of representative tensile specimens showed no signs of brittle failure, with all fracture surfaces exhibiting a ductile fracture appearance.

Fracture-toughness test results of the weld metals are summarized in Table 27 and of the Nitronic-40 base metal in Table 26. While the numerical values are adequate, with average values for the base metal, SMA, GTA, and GMA weld-metals of 132.0 ksi $\sqrt{in.}$, 122.8 ksi $\sqrt{in.}$, 121.3 ksi $\sqrt{in.}$, and 136.0 ksi $\sqrt{in.}$, respectively, further examination of the test specimens and test records give rise to serious doubts about the validity of these values for the reasons presented below:

1. While the range of numerical values of the weld metal fracture-toughness for the three weld processes are high (122.8 to 136.0 ksi $\sqrt{in.}$), examination of the fracture-toughness test methods

TABLE 27. Comparison of minimum fracture-toughness specimen thickness required to achieve plane-strain test conditions in Inconel 625 weld metal.[a]

Weld process	K,[b] ksi $\sqrt{in.}$	σ_y,[b] ksi	a, B_{calc} in.	B_{meas} in.
SMA	123	127	2.35	0.5
GTA	121	138	1.92	0.5
GMA	136	121	3.16	0.5
Base metal	132	196	1.13	0.5

[a]From ASTM E 399-74, $aB \geq 2.5\,(K/\sigma_y)^2$, where a,B are the width and thickness of the fracture-toughness specimen, K the measured value of stress intensity at fracture, and σ_y the yield strength.

[b]Average values used in calculations.

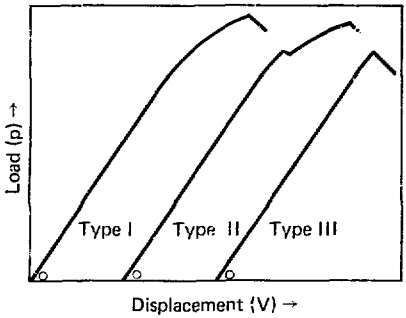

FIG. 93. Types of load displacement traces obtained during fracture toughness testing.

indicated that the values determined are nonconservative and use of these values for design would result in over-estimation of these weld metals' resistance to brittle fracture. These nonconservative results were obtained because the size of the fracture-toughness samples used were too small (Table 27 and Ref. 95) to achieve conservative or "plane strain" values. Figure 92 schematically represents the variation of stress intensity factor K, with specimen or component thickness. For conditions of plane strain, where the material thickness is great enough to constrain plastic flow (yielding) in the plane of a crack or other defect, $K = K_{IC}$. For other than conservative or plane strain conditions, $K = K_Q > K_{IC}$. What had been determined for the

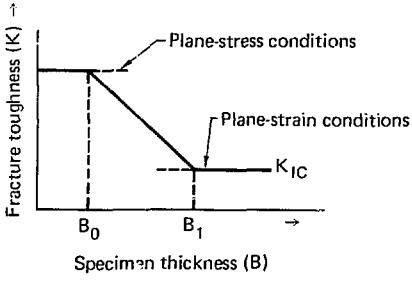

FIG. 92. Effect of specimen thickness on fracture toughness.

Nitronic 40 base metal and the alloy 625 welds was K_Q.

2. In addition to the nonconservative fracture-toughness values of the various weld metals, examination of fracture-toughness test procedures indicated that the form of fracture-toughness test load/displacement traces indicate that all the test results exhibited evidence of catastrophic crack propagation. Representative load/displacement curves are shown in Fig. 93. Referring to this figure, either Type 1 or Type 2 behavior is representative of acceptable service-behavior, i.e., propagation of a preexisting flaw requires increasing load. However, Type 3 behavior, where once a flaw begins to propagate, it continues to do so even with a decreasing load situation, is unacceptable from the standpoint of rational brittle-fracture-resistant design practices.

3. Examination of the 4 K tensile test results shows that the Alloy 625 weld-metal yield strengths, irrespective of weld process used, fall in the range of 117 to 143 ksi, or about 60–73% of the base metal value. Design of the magnet case requires that some of the welds be located in the primary load paths. Under these conditions, it is good design practice to match the base-metal and weld-metal yield-strengths to prevent localization of load and strain in the weaker weld-metals to avoid over-loading of the weld metal, early development of cracks, and rapid propagation of the small, preexisting flaws expected in any weld. At this time, late June 1978, it

was recognized by the MFTF magnet project engineer that reconsideration of the selection of the magnet case structure material and the associated welding development efforts was needed. Experts in the associated areas of structural materials for cryogenic service and welding development from within LLNL and from other organizations (National Bureau of Standards at Boulder, General Dynamics/Convair, and the DOE) met at Livermore on June 23, 1979 to reexamine the related issues of selection of the case structural material and associated welding development. The recommendations of this review committee are summarized below and were adopted by the MFTF magnet project engineer for implementation.

By using as a guide the principle of selecting a base metal:weld metal pair with equal 4 K tensile yield strengths, a base metal 4 K tensile yield strength not less than 1.5 times the General Dynamics/Convair design stress of 80 ksi, and a 4 K fracture-toughness value of 125 ksi $\sqrt{\text{in.}}$, the following preliminary recommendations were proposed:

Type 304LN base metal :316L weld metal, or

Type 316LN base metal :316L weld metal.

Welds should be made by the GMA process for optimum control of purity, 4 K fracture-toughness, and ferrite content. Neither of these approaches entails materials costs as high as the Nitronic 40:Inconel 625 approach. The need for resolution of the one open issue, optimization of weld-metal composition to prevent weld-metal microfissuring during production of the restrained, heavy-section welds (up to 3-in. thick) in the actual case, versus limitation of ferrite content to guard against degradation of 4 K weld-metal fracture-toughness, was recognized.

WELD DEVELOPMENT PROGRAMS PERFORMED IN SUPPORT OF JOINING TYPE-304LN BASE METAL

Once the choice of type 304LN stainless steel was made, three separate but related weld-development programs were begun to provide an initial evaluation of the suitability of the common welding processes, such as SMA, GMA, GTA, SA, FCMA (flux-cored metal arc), and ESW (electroslag welding), for deposition of type 316L stainless steel weld metal. Evaluation of a variety of processes was necessary to ensure the eventual selection of one or more processes that would enable out-of-position (other than flat position) welding to be done, as well as qualify a process, such as SA or ESW, that would enable large quantities of weld metal to be deposited in a short time with a concurrent reduction in welding time and costs (Table 28). With this task essentially completed, and the SMA process selected by Chicago-Bridge and Iron Company (CBI), the successful bidder on the case-fabrication contract, two parallel programs were initiated. One of these programs involved qualification of CBI's SMA welding procedures using

TABLE 28. Estimated time required to weld MFTF magnet case assuming 20,000 lb of weld metal deposited.

Weld metal deposition data	Shielded-metal arc	Gas-metal arc	Flux core	Submerged arc	Electroslag (Note a)	Electroslag (Note b)
Deposition data						
100% arc time, lb/h	2.5	9.0	13.0	14.5	15.0	40.0
Est. arc time, %	20.0	30.0	40.0	50.0	95.0	95.0
Actual deposition rate, lb/h	0.5	2.7	5.20	7.25	14.25	38.0
Welding time						
Total hours to weld	40,000	7,407.4	3,846.2	2,758.6	1,403.5	526.3
No. man-hours required[c]	240	44.4	23.1	16.6	8.4	3.1
No. man-months required[c]	20	3.70	1.92	1.38	0.7	0.26

[a] Per measured lab rate using a 400-A power supply (max). Not sufficient.

[b] Attainable with power supply of adequate capacity.

[c] Values based on available man-hr/yr = (8 h/d)(5 d/wk)(5 wk/yr) = 2000 man-hr/yr/man.

E316L-15 electrodes, and the other involved development of welding information for use in other areas of magnet fabrication, such as the magnet jacket, and for a backup weld metal should difficulties arise with the weld metal deposited by type E316L-15 electrodes. The status of each of these programs, including results to date, open issues, and ongoing work, is presented below.

Multiprocess Study

Welds were made by the SMA, GMA, SA, FCMA, and ESW processes in type 304LN stainless steel plate ranging in thickness from 1-3/4 to 3 in. using type 316L weld metal in the form appropriate to the welding process. Details of the joint design and welding position are summarized in Table 22. Most of the welds were made at Livermore, but two welds, one GMA and one ESW, were made at FMC (San Jose). The fabrication subcontractor for the magnet case, CBI, supplied a GMA weld using a ferrite-free filler, 2RM69, for evaluation by LLNL. All the welds made at LLNL were made under heavily-restrained conditions, i.e., the plates were first welded to a 4- to 6-in.-thick mild-steel plate to prevent free thermal expansion and contraction of the plates and connecting test weld, thus simulating the situation that exists during assembly of the magnet case.

Those weld-metal chemical compositions determined to date are reported in Table 23. Initial evaluation of welding performance was by room temperature side-bend testing. Failures were seen in both specimens from weld No. 8 (GMA process, 316L, filler) and one of two specimens from weld No. 9 (SA, 316L filler) made at LLNL. Failure in the latter case was associated with an entrapped-slag defect in the tension-side of the sample. Such a defect is associated with incomplete removal of the fused slag during welding, and is not an inherent problem in either the choice of weld filler material or process. However, the two failures in the GMA welds were traced to thin oxide films on the solidifying weld metal, caused by the presence of 2% O_2 in the shielding gas. Oxygen is added to the argon shielding gas to lower the surface tension of the molten stainless steel weld metal and promote flow of the molten metal to the edge of the weld joint, thus ensuring complete wetting along the entire weld-metal-to-base-metal interface (Ref. 96). As such, the cause of failure in the GMA samples was associated with the weld process and was considered to be sufficient reason to eliminate conventional GMA welding, which uses Ar-O_2 gas mixtures, from further consideration.

Intergranular cracks of lengths insufficient to constitute failure according to Section III of the ASME Boiler and Pressure Vessel Code were seen in side-bend specimens of Weld No. 17 made by CBI (Houston), using the pulsed GMA process, 2RM69 filler and 75% He–25% Ar shielding gas. Details of evaluation of this weld conducted by both LLNL and CBI (Houston) are contained in Refs. 97–99. Briefly, many intergranular fissures, with lengths up to 0.008 in., were found in the as-deposited weld metal. After side-bend testing, these defects grew to lengths of up to 0.156-in. While the exact cause of these defects was not determined, the fact that they occurred on a weld metal specially developed for freedom from this type of defect (Ref. 100) and in weld deposits made with a process (GMA) known to be sensitive to both operator and process variables (Ref. 96) causes one to view with concern any use of conventional GMA welds and 2RM69 filler metal for the stringent requirements of 4 K high-stress service.

Low-temperature mechanical-property evaluations of all welds included 77 K Charpy V-notch impact tests, followed by 4 K tensile and fracture-toughness testing of selected welds. Results are presented in Tables 24 and 25 and discussed below.

77 K Charpy V-Notch Impact Test Results (Figure 94).

As a function of weld process, from largest to smallest value of average energy absorption, the results for the Livermore-produced welds were: ESW, SMA, SA, GMA, and FCMA. Using average lateral expansion at the root of the notch as a rating tool, the results for the Livermore-produced welds were: ESW, SMA, GMA, SA, and FCMA. Results are also shown in Fig. 94 for two welds made by FMC (San Jose). Their ESW weld exhibited much lower impact performance than the two ESW welds made by Livermore, but their pulsed-GMA weld results fell between the SMA and Livermore GMA results. Based on the results of the Livermore-produced welds, the SMA, SA and ESW welds were selected for evaluation at 4 K.

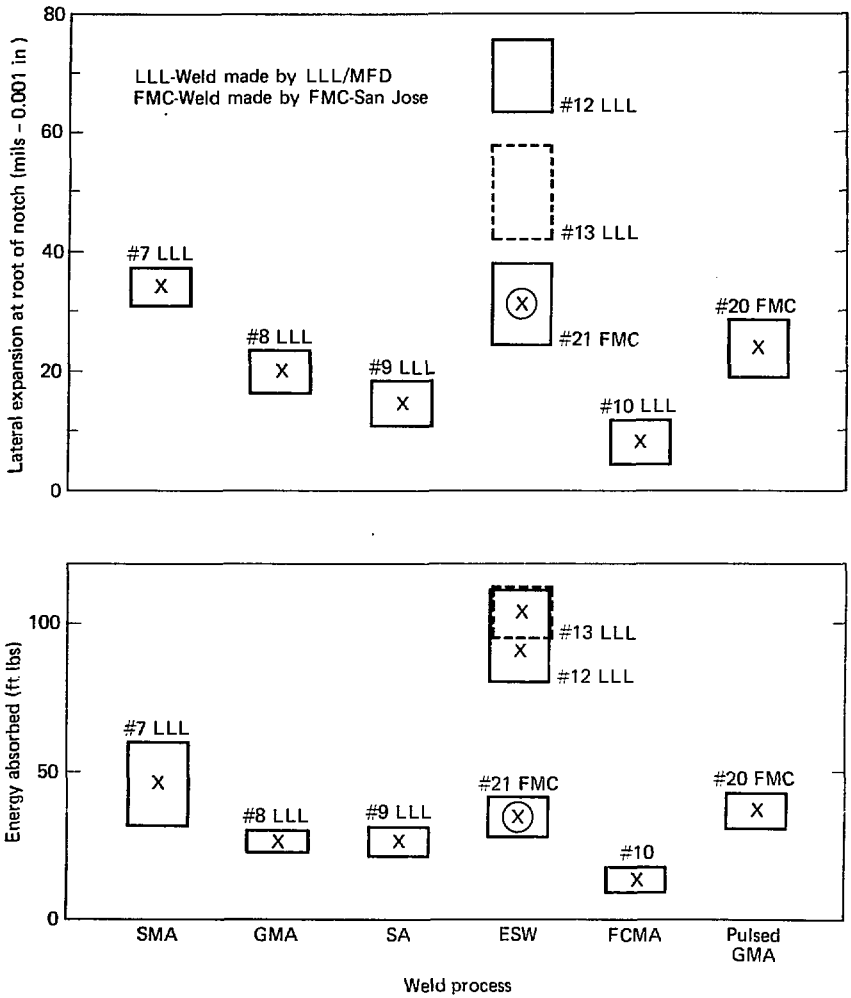

FIG. 94. Results of 77 K Charpy V-notch impact tests on type 316L weld metal deposited by various welding processes and laboratories.

4 K Tensile and Fracture-Toughness Test Results (Table 25 and Fig. 95)

Table 25 and Fig. 95 give our 4K tensile and fracture toughness test results, together with data from other sources (Refs. 101 and 102). Examination of Fig. 95 shows that the SMA weld, No. 7, exhibited a superior combination of yield strength and fracture-toughness relative to both the SA weld, No. 9, and the ESW weld, No. 12. This provided additional support for selection of the SMA process as the primary candidate for fabrication of the magnet case. Most of the data from Refs. 101 and 102 was generated after testing of welds 7, 9, and 12 was completed. The consistently superior performance of SMA welds shown in Fig. 95 confirms the choice made in the basis of data from the three Livermore-produced welds.

Evaluation of Weld-Metals Deposited by the SMA Process Using Type E316L-15 Electrodes

Welds have been made by both Livermore and the CBI corporate welding laboratory, using E316L-15 electrodes supplied by both the Teledyne-McKay Corporation under the trade name "Kryokay" and by the ARCOS Corporation. Both companies supply product to specification AWS 5.4-75, the industry standard, with an added restriction of a ferrite number (FN) of zero, i.e., an all-austenitic weld metal. All butt welds were made in 3-in.-thick type 304LN plates which were heavily restrained by first welding the plates to a 6-in.-thick strongback (LLNL) or by welding into a rigid restraint fixture (CBI-Houston). These welds are described in Table 29.

Those weld-metal chemical compositions determined to date are reported in Table 30. Initial evaluation of weldment performance was by room temperature side-bend testing. No failures were observed.

Low-temperature mechanical-property evaluations included 77 K Charpy V-notch impact tests of most welds, followed by 4 K tensile, fracture-toughness, and fatigue-crack growth testing of selected welds. Results are presented in Tables 31 and 32. The 77 K Charpy V-notch impact test results are presented in Table 31 and summarized in Fig. 96. On the basis of these results, there was little difference between ARCOS and Teledyne-McKay filler metals, or between welds made in the flat or vertical positions. The 4 K tensile and fracture-toughness test results are presented in Table 30 and summarized in Fig. 97. Note that the performance

TABLE 29. Shielded-metal-arc welds in type 304LN, using type E316L-15 electrodes.

Weld No.	Diam. (in.)	Electrode			Weld joint			Ferrite No. by	
		Supplier	Heat No.	Lot No.	Type	Origin	Position	Vendor	LLNL
7	5/32	McKay	02146	2161376	Butt	LLNL	Flat		1.0
14	3/16	McKay	21333	3186938	Butt	LLNL	Flat		1.0
16	3/16	Arcos	T-12150-2		Flat	LLNL	Flat	0	0
18	5/32 & 1/8	McKay	386022	3086644	Butt	CBI-Hstn	Vert.	0	
19	1/4	McKay	N/A	0631-401	Butt	LLNL	Flat		
22	5/32 & 3/16	McKay	N/A	N/A	Butt	CBI-Hstn	Flat		
23	1/4	Arcos	T-12150-2		Butt	CBI-Hstn	Flat		
24	1/8	McKay	386022	3086683	Butt	CBI-Hstn	Vert.	0.5	
28	5/32	McKay	02146	2161376	Dble-V	LLNL	Vert.		0
29	5/32	McKay	16329	3178554	Dble-V	LLNL	Vert.		0
34	5/32	McKay	586108	2397723	Butt	LLNL	Flat	0	
35	5/32	McKay	586108	2397723	Dble-V	LLNL	Vert.	0	
38	5/32	McKay	586108	2397723	Butt	CBI-Hstn	Vert.	0	

N/A—Data not available.

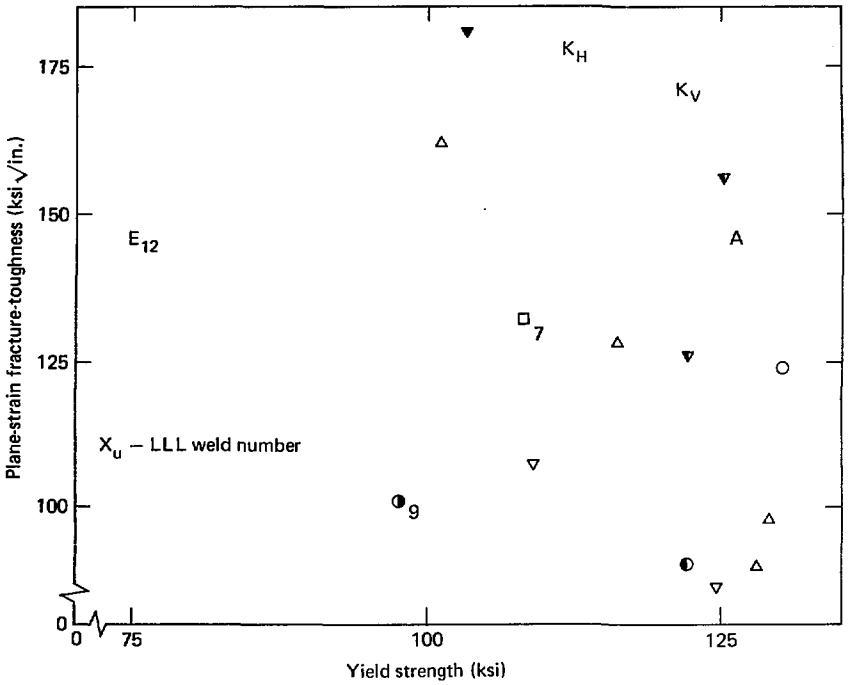

Symbol	Welding process and details	Base metal	Reference
△	SMA E316L-16	304 L	101
▽	SMA E316L-15	316 LN	101
▼	SMA E316L-15, Interpass peening	316 LN	102
▼	SMA E316L-15, Interpass peening plus 1900 F/1 hr/H_2O Quench	316 LN	102
K_H	SMA "KRYO-KAY", Horizontal weld	304 LN	This Report
A	SMA ARCOS E316L-15	304 LN	
K_V	SMA "KRYO-KAY", Vertical weld	304 LN	
○	SA 316L	304 LN	102
◐	SA 316L	304 LN	102
◑	SA 316L	304 LN	This Report
E	ESW 316L	304 LN	
□	SMA E316L-15 Flat weld	304 LN	

FIG. 95. 4 K plane-strain fracture toughness as a function of yield stress for type 316L weld metal deposited by various processes.

TABLE 30. Chemical compositions of shielded metal-arc welds made in type 304LN using type E316L-15 electrodes (wt%).[a]

Weld No.	C	Mn	Si	S	P	Cr	Ni	Mo	Ti	Cb+Ta	Cu	N_2	V
14	0.030	1.65	0.35			18.0	13.2	2.25					
16	0.033	2.44	0.36	0.007	0.032	18.20	13.81	2.14				0.056	
	0.033	2.54	0.33	0.010	0.035	18.07	13.81	2.23				0.061	
18	0.023	2.14	0.30	0.014	0.022	18.12	13.22	2.29	0.05	0.02	0.18		0.45
23	0.033	2.44	0.36	0.007	0.032	18.20	13.81	2.14				0.056	
24	0.025	1.94	0.28	0.012	0.021	17.80	13.00	2.22	0.06	0.02	0.22		0.042
28	0.030	1.64	0.35			18.0	13.2	2.25					
29	0.030	1.65	0.35			18.0	13.2	2.25					
34	0.036	2.18	0.22	0.012	0.018	17.84	13.58	2.10		0.02	0.28		0.084
35	0.036	2.18	0.22	0.012	0.018	13.58	13.58	2.10	0.052	0.02	0.28		0.084
38	0.036	2.18	0.22	0.012	0.018	13.58	13.58	2.10	0.052	0.02	0.28		0.084

[a]As determined on undiluted weld pads deposited in flat position.

of the individual weld metals is independent of both supplier and weld position and falls at the upper end of the scatter-band for all data in type 316L weld metals deposited by the SMA process. Examination of the 4 K tensile ductility data in Table 32 indicated a large variation in both elongation (5.4% to 44.0%) and reduction area (6.8% to 33.5%). Since low values of both of these quantities are indicative of some factor in the weld metal being out of control, metallographic examinations of the welds having both high and low values of these ductility parameters were conducted.

Metallographic Examinations of Welds

Examinations were performed using standard optical-microscopy techniques, and indicated that low values of elongation and reduction in area appear to be associated with the presence of extensive weld-metal defects in or near the plane of fracture. Such defects include microfissures (Refs. 100, 104-107) or small (0.005-0.030-in. long) inter-granular cracks that form during solidification of low-ferrite or ferrite-free weld metal (Fig. 98) and such operator-related defects as lack of fusion (Fig. 99) and slag entrapment (Fig. 100), which are caused by less than satisfactory welding practices. A semi-quantitative rating of the occurrence of microfissures was made, presented in Table 32, indicates that the presence of appreciable amounts of this type of defect is limited to the vertical welds Nos. 18, 28, and 29 made with Teledyne-McKay "Kryokay" electrodes. As this fact was discovered too late during the fabrication-cycle of the two magnet cases to change to another weld metal, certain remedial steps to limit the occurrence of microfissuring and assess the effect of heavily microfissured welds on the expected performance of simulated case close-out welds were undertaken and are discussed later.

Fatigue-Crack Growth Behavior of Type-316L Weld Metals

Fatigue-crack growth behavior was evaluated by the National Bureau of Standards and the results are presented in Fig. 101. Note that the behavior of type-316L weld metals are consistent in that the fatigue crack growth (FCG) rates fall with a factor of about 5 of each other and are about a factor of 3 to 10 less than that of the type-304LN base metal used for fabrication of the magnet cases. An informal report (Ref. 103) prepared by General Dynamics/Convair, using the actual 4 K mechanical properties of the base metal and welds presented in Fig. 101, demonstrated the structural adequacy of this case at a design stress of 80 ksi at 4 K.

TABLE 31. Charpy V-notch impact performance at 77 K of shielded-metal arc welds in type 304LN plate using type E316L-15 electrodes.

Weld No.	Energy absorbed		Lateral expansion	
	Average, ft-lb[a]	Range, ft-lb	Average, mils[a,b]	Range, mils
7	41.7	32.0 to 60.0	37.8	30.8 to 37.2
14	33.8	29.5 to 38.0	30.0	18.5 to 54.0
16	39.4	38.0 to 42.0	26.0	24.0 to 28.5
18	43.7	34.0 to 53.0	30.5	24.0 to 40.0
22	37.6	27.0 to 48.0	29.6	21.0 to 35.0
24	39.8	35.0 to 45.0	30.2	26.0 to 41.0
34	40.5	39.8 to 41.2	29.0	27.0 to 31.0
35	40.5	39.8 to 41.2	29.0	27.0 to 31.0
38	46.6	39.0 to 56.0	30.0	28.0 to 40.0

[a]Average of 3 to 5 specimens.

[b]1 mil = 0.001 in.

TABLE 32. 4 K tensile properties of shielded-metal arc welds made in type 304LN plate using type E316L-15 electrodes.

Weld No.	Spec. orient.[a]	4 K tensile properties				K_{IC}[b]	Occurrence/ extent of microfissures	Micro-structure	Ferrite No. by	
		Ultimate strength, ksi	Yield strength, ksi	Elong. 1 in., %	Reduction in area, %				Vendor	I.I.I.
7	L	178.2	108.0			132.0		Austenite		1
								Ferrite		
14	LT	189.4	152.3	26.0	25.7			Austenite		1
	L	176.4	119.8	25.0	25.0		Few	Ferrite		
	ST	176.2	117.0	44.0	27.4					
16	L	153.5	111.1	18.0	27.5					
	ST	187.4	125.7	44.0	33.5	146.0	Some	Austenite	0	0
18	L	159.4	123.8	5.4	6.8	170.0	Many	Austenite	0	0
22	L	183.2	112.0	36.4	28.1	183.0	Some	Austenite		
23	L	163.6	130.7	10.0	10.9					
	LT	180.7	128.5	16.0	14.5				0.5	
	ST	171.4	123.5	32.0	24.3					
28	L	168.7	111.9	14.5	16.2		Some	Austenite		0
29	L	184.2	145.3	9.5	10.8		Some	Austenite	1	0
35	L	188.3	111.3	19.0	17.6				0	

[a]Specimen orientation relative to centerline of weld.

L—Longitudinal, parallel to weld axis.

LT—Long transverse, across weld axis.

ST—Short transverse, through weld thickness.

[b]Determined by elastic-plastic J-integral test.

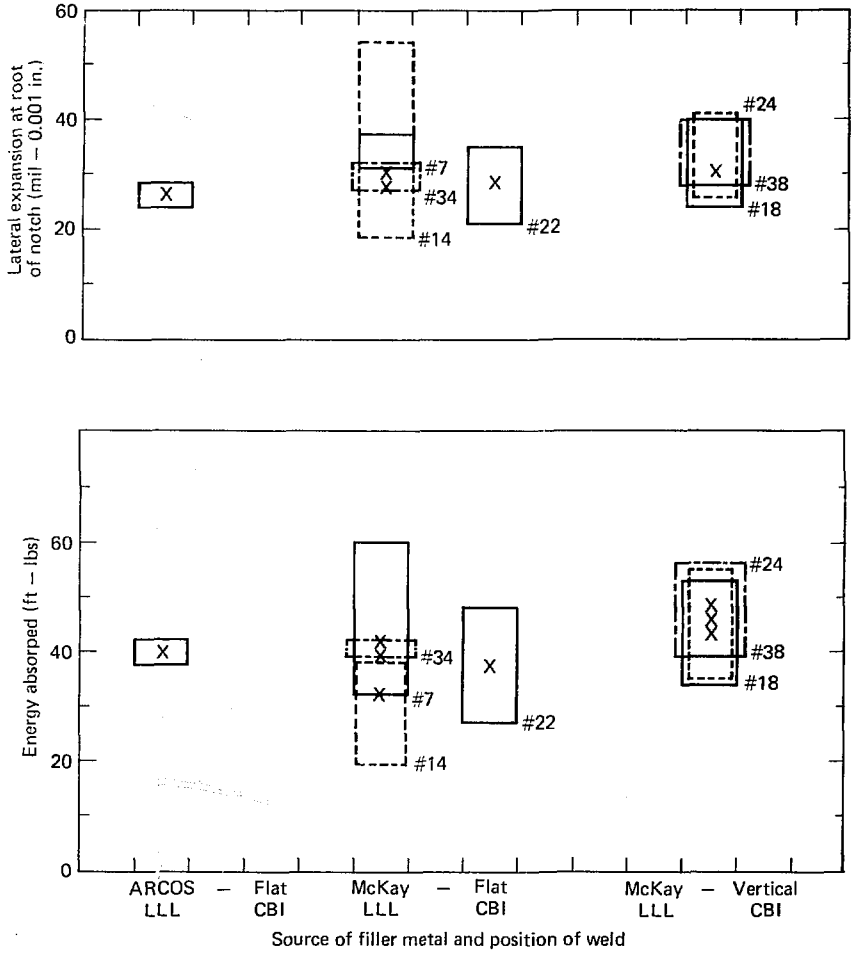

FIG. 96. Results of 77 K Charpy V-notch impact tests on type 316L-15 weld metals deposited on type 304LN base plate.

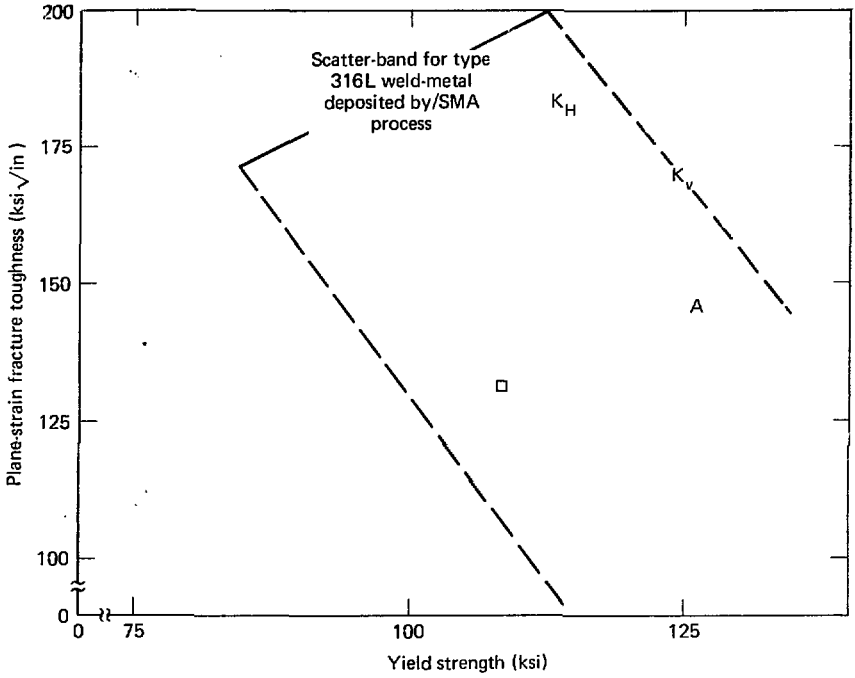

Symbol	Filler-metal vendor	Base metal	Comments	LLL welding
K_H	Teledyne-McKay	304 LN	Flat weld	22
A	ARCOS	304 LN	Flat weld	16
K_v	Teledyne-McKay	304 LN	Vertical weld	18
□	Teledyne-McKay	304 LN	Flat weld	7

FIG. 97. 4 K plane-strain fracture toughness as a function of yield strength for type 316L weld metal used in fabrication of MFTF.

FIG. 98. Microfissure (a) in SMA weld No. 18. A vertical weld made with Kryokay electrodes, magnified 100 times.

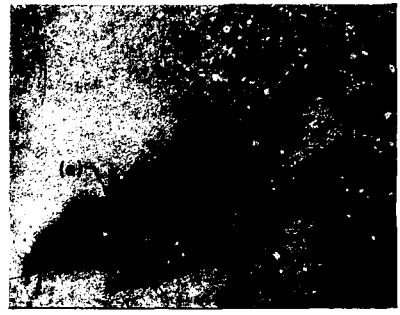

FIG. 99. Lack-of-fusion defect (a) near fusion line (b) in weld No. 52. A flat-position weld made with Kryokay electrodes, magnified 63 times.

EVALUATION OF SHIELDED METAL ARC WELD-METALS DEPOSITED BY OTHER THAN TYPE E316L-15 ELECTRODES

Details of joint design for these welds are given in Table 33. Evaluation of these weld-metals was confined to a limited number of chemical analyses (Table 34), 77 K Charpy V-notch impact tests (Table 35), and 4 K tensile tests and metallographic examinations (Table 36). Brief descriptions of the results reported in Tables 34-35 are presented for each weld metal evaluated:

ARCOS 17-15 Cr-Ni

This was a lower Cr higher Ni modification of type 316L, intended to give improved 77 K impact performance relative to ARCOS' type E316L-15 filler metal. Comparison of 77 K impact test results for the 17-15 Cr-Ni weld metal (Table 35) with the values obtained for ARCOS commercial product (Table 31 and Fig. 96) showed about a 7 ft-lb increase in average energy absorption values and about a 6-mil increase in average lateral expansion values. Results of 4 K tensile tests (Table 36) showed unsatisfactory behavior in that the ultimate tensile strength values, when the weld metal was tested in three mutually perpendicular directions, were very slightly greater than the tensile yield strengths. This type of behavior is generally considered indicative of unstable structural behavior, since once yielding commences, the material is incapable of strain hardening to relieve local stress concentrations, and unstable plastic flow will continue at a constant or decreasing load until the occurrence of failure. For this reason, further work on this material was discontinued.

Type 316-16

This type was evaluated for suitability for joining the inner jacket which surrounds the magnet. Evaluation was limited to a few 4 K tensile tests and microstructural evaluations (Table 36), which indicated that no evidence of weld-defect formation or undesirable effects on 4 K tensile properties is expected.

FIG. 100. Slag inclusions in SMA weld No. 52. A vertical weld made with Kryokay electrodes, magnified 63 times.

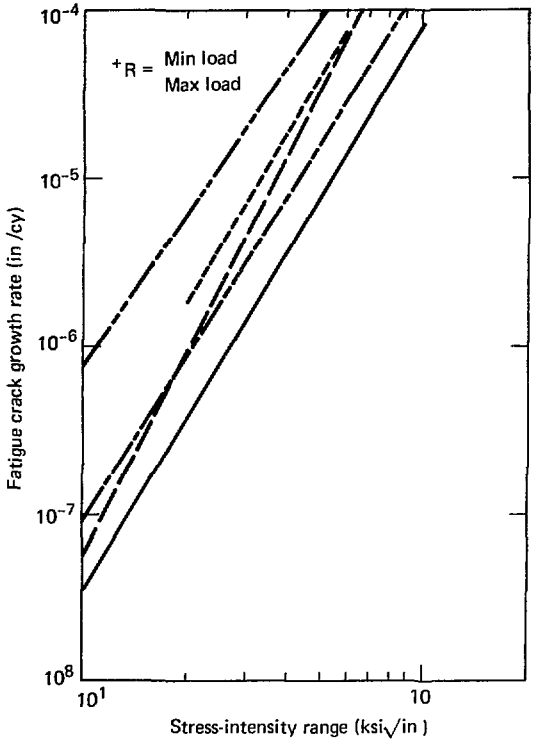

Symbol	Product form	Filler metal and details	Base plate	R^+
1	3-in. weld	Arcos flat weld	304 LN	+0.1
2	3-in. weld	McKay flat weld	304 LN	+0.1
3	3-in. weld	McKay vertical weld	340 LN	+0.1
4	1-in. weld	Chemetron flat weld, 1900°F-1 h	316 LN	+0.1
5	3-in. plate	Fan cooled	304 LN	+0.1

FIG. 101. Liquid-helium fatigue crack growth behavior of the type 316L weld metals deposited by the shielded-metal arc process using a -15 coating.

TABLE 33. Shielded-metal-arc welds in type 304LN base metal using other than type E316L-15 electrodes.

Weld No.	Electrode					Weld joint			Ferrite No.	
	Filler metal	Diam. (in.)	Supplier	Heat No.	Lot No.	Type	Origin	Position	Vendor	LLNL
15	16-[illegible]	3/16	McKay	386022	2197476	Butt	LLNL	Flat	0	0
25	17/1[illegible] Cr-Ni	1/8	ARCOS	N/A	T12984	Butt	CBI-Hstn	Vert.	0	0
27	17/15 Cr-Ni	5/32	ARCOS	1345-40-145	T12984	Dble-V	LLNL	Vert.		0
32	316-16	5/32	Coor.-Indus.	N/A	N/A	Dble-V	LLNL	Vert.		
33	316-16	1/8	Coor.-Indus.	N/A	N/A	Dble-V	LLNL	Vert.		
36	316L-16	5/32	Nemco	83118	N/A	Dble-V	LLNL	Vert.		
37	Mod 316L	5/32	ARCOS	T13243	N/A	Dble-V	LLNL	Vert.		
26	316-16	5/32	Coor.-Indus.	N/A	N/A	Dble-V	LLNL	Vert.		1.5
30	In 625	1/8	Inco	1877	N/A	Dble-V	LLNL	Vert.		
31	In 625	5/32	Inco	N/A	N/A	Dble-V	LLNL	Vert.		

N/A—Date not available.

TABLE 34. Chemical compositions and ferrite levels of shielded-metal arc welds in type 304LN base metal using other than type E316L-15 electrodes (wt %).[a]

Weld No.	C	Mn	Si	S	P	Cr	Ni	Mo	Ti	Cb	Ta	Cu	N2	V	Ferrite No. Vendor	Ferrite No. LLNL
25	0.041	2.80	0.30	0.04	0.025	17.57	15.85	2.01	0.006	0.06	0.13	0.017	0.159	0	0	

[a]As determined on undiluted weld pad deposited in flat position.

TABLE 35. Charpy V-notch impact performance at 77K of shielded-metal arc welds in type 304LN base metal using other than type E316L-15 electrodes.

Weld No.	Energy absorbed		Lateral expansion	
	Average, ft-lb[a]	Range, ft-lb	Average, mils[a,b]	Range, mils
25	47.3	45.0 to 53.0	31.4	22.6 to 41.5
27	46.9	41.0 to 50.0	34.9	31.0 to 40.0

[a]Average of 3 to 5 specimens.

[b]1 mil = 0.001 in.

TABLE 36. 4 K tensile properties and microstructural observations of shielded-metal arc welds in type 304LN base metal using other than type E316L-15 electrodes.

Weld No.	Spec. orient.[a]	4 K tensile properties: Ultimate strength, ksi	Yield strength, ksi	Elongation 1 in., %	Reduction in area, %	Occurrence and extent of microfissures	Microstructure
15		(b)	(b)	(b)	(b)		
	L	136.4	132.3	11.0	19.6		
25	LT	132.3	129.8	13.5	16.2		
	ST	94.2	94.2	56.0	38.9		
27	L	175.0	146.1	12.5	13.7	Some	Austenite
32	L	201.0	162.9	9.0	16.3		
33	L	197.3	119.4	7.0	16.1		
36	L	202.0	129.7	20.0	16.8		
37							
26	L	162.1	162.1	7.0	10.9	Few	Austenite and
30		(b)	(b)	(b)	(b)		ferrite
31	L	188.9	132.3	27.0	22.4	None	
							Austenite

[a]Specimen orientation relative to centerline of weld.
L—Longitudinal, parallel to weld axis.
LT—Long transverse, across weld axis.
ST—Short transverse, through weld thickness.
[b]Not available or determined.

Multiprocess Study

Results of this study represent the first systematic evaluation of a variety of welding processes for the deposition of stainless steel weld metal for 4 K service. As such, this program was truncated once the magnet case fabricator, CBI, indicated a willingness to use the SMA process for fabrication of the magnet cases. The results contained in Tables 22-24 and summarized in Figs. 94-95, although far from complete, support the following *very tentative* conclusions:

1. Selection of the SMA process, using type E316L-15 electrodes manufactured by Teledyne-McKay and sold under the trade name "Kryokay", was a technically-valid decision at the time the selection was made, December 1978–January 1979. Even though this process exhibits the lowest rate of weld-metal deposition (Table 28), the combination of good 4 K tensile and fracture-toughness properties exhibited by weld No. 7, made with Teledyne-McKay E316L-15 electrodes, coupled with the case fabricator's willingness to use this process over other, higher weld metal deposition-rate processes, such as SAW and FCMA for which little or no 4 K data was available at the time of issuance of the magnet case RFQ, reenforces the basic validity of the selection. Type 316L weld metal deposited by *the SMA process was the only process:filler metal* combination where anything more than fragmentary information on 4 K properties was in existence in the December 1978 to January 1979 time frame.

2. Use of O_2 additions to Ar to stabilize the welding arc and/or improve the weld-bead contour during GMA welding of Type 316L or 2RM69 fillers should *not* be used because of the pronounced tendency towards formation of weld-pass-boundary oxide-films, which reduce low-temperature toughness and promote premature failures in side-bend testing. Rather, the use of pulsed GMA welding and Ar-H_e shielding gases should be evaluated.

3. The following weld-process:filler-metal combinations, although not selected for use, exhibited sufficently satisfactory combinations of mechanical properties at 77 K and 4 K which, when coupled with their known improved weld metal deposition-rates over those shown in Table 28 for the SMA process, make them candidates for further evaluation for "out-of-position," i.e., other than flat-position applications:

Process	Filler metal	Shielding gas or flux
Pulsed GMA	E316L	Ar or Ar-He
Electro-slag	316L	neutral, such as Hobart HS-300

EVALUATION OF SHIELDED-METAL ARC WELDS USING TYPE 316L-15 ELECTRODES

Results of this investigation indicate that, on the basis of 4 K tensile, fracture-toughness, and FCG test results, type 316L stainless steel weld-metal deposited with SMA electrodes with a lime-titania (-15) coating should be adequate for the intended application. However, the fairly consistent occurrence of reduced 4 K tensile ductility in vertical welds made with both Teledyne-McKay and ARCOS electrodes, and the occurrence of large numbers of microfissures, slag inclusions, and lack of fusion in these fully-austenitic welds, gives cause for concern regarding the structural integrity of these vertical welds. To determine whether the defect-containing welds might be unsuitable under the anticipated service conditions, while maintaining fabrication of the magnet cases, several efforts were mounted in parallel:

1. Review of available literature on the effects of microfissures and other defects on the low-temperature properties of stainless steel weld metals.

2. Manufacture and testing of several large fatigue specimens from highly microfissured stainless steel welds.

3. Evaluation of candidate backup weld metals deposited by the SMA process, should either or both of the above efforts indicate the existence of serious impairment of the fracture-toughness or FCG performance of microfissure-containing 316L weld metal.

4. Accelerated development of ultrasonic test (UT) nondestructive inspection methods to ensure that the critical close-out welds in the magnet cases are free of flaws that are large enough to propagate to failure of the welds under design conditions.

Review of the published information on microfissures in stainless steel weld metals (Refs. 104–107, for example) revealed over 100 applicable references on possible mechanisms of microfissuring and how to minimize or eliminate it. Only one (Ref. 107) was found that evaluated the effects of microfissures on mechanical properties from room temperature to 77 K in completely austenitic types 316 and 310 stainless steel weld metals deposited by the SMA process. Their conclusions were that:

a. Microfissures are unlikely to significantly affect the tensile strength or ductility between 77 K and 300 K in types 316 or 310 stainless steel weld-metals if the loss in load-bearing area due to microfissures is less than 5%. Above 5% loss in load-bearing area, a progressive decrease in tensile ductility with increasing loss in load-bearing area up to the maximum loss of load-bearing of about 20% was seen for type 310 weld metal. No data on this effect was available for type 316 weld metal, since not more than 5% loss in load-bearing area due to microfissure formation was seen in this material.

b. Higher Charpy V-notch impact energy-absorption values were obtained for fully austenitic weld-metals (types 316 and 310) containing microfissures than for microfissure-free deposits of type-316 weld metal containing as much as 17% ferrite. An estimated plane-strain fracture-toughness value for the fully austenitic type-316 weld metal at 77 K is 150 ksi $\sqrt{\text{in.}}$, which is comparable to a value of 144 ksi $\sqrt{\text{in.}}$ at 77 K for a similar material in which no microfissures were seen (Ref. 101).

Specimens for 4 K fatigue testing of heavily-microfissured type-316L weld metal have been machined and nondestructively examined for location, size, and amount of defects, and are awaiting shipment to Martin-Marietta, Denver Division, for testing under a fatigue-spectrum representative of anticipated case operating conditions. Also the candidate backup SMA welding consumables listed in

Table 32 have been or are in the process of being manufactured into 2- to 3-in.-thick restrained welds for evaluation by microscopy, side-bend testing, and 4 K tensile and fracture-toughness testing. For production quality control a subcontract is being placed with a manufacturer of ultrasonic testing equipment for the purpose of optimizing special UT transducers and constructing a prototype operating UT system for inspection of the case weldments. Reference 108 contains additional details on this activity.

EVALUATION OF SHIELDED-METAL ARC WELD METALS DEPOSITED BY OTHER THAN TYPE E316L-15 ELECTRODES

The unsatisfactory 4 K tensile and microfissuring results on the ARCOS 17-15 Cr-Ni filler metal has resulted in discontinuance of work on this material. Any additional work on other filler metals will be carried out under the evaluation of candidate backup filler metals task previously described.

REFERENCES

1. F. H. Coensgen, W. F. Cummins, B. G. Logan, A. W. Molvik, W. E. Nexsen, T. C. Simonen, B. W. Stallard, and W. C. Turner, *Phys. Rev. Lett.* **35**, 1501 (1975).
2. C. D. Henning et al., "Large Superconducting Baseball Magnet—Part II," in *Proc. 8th Intl. Cong. of Refrigeration, Washington, D.C., 1971* (Intl. Inst. of Refrigeration, 1971).
3. G. A. Carlson, B. Arfin, W. L. Barr, B. M. Boghosian, J. L. Erickson, J. H. Fink, G. W. Hamilton, B. G. Logan, J. O. Myall, and W. S. Neff, Jr., *Tandem Mirror Reactor with Thermal Barriers*, Lawrence Livermore National Laboratory, Rept. UCRL-52836 (1979).
4. D. N. Cornish, J. P. Zbasnik, R. L. Leber, D. G. Hirzel, J. E. Johnston, and A. R. Rosdahl, *IEEE Trans. Magn.* **MAG-15**: 530 (1979).
5. D. N. Cornish, D. W. Deis, A. R. Harvey, D. G. Hirzel, J. E. Johnston, R. L. Leber, R. L. Nelson, and J. P. Zbasnik, *Development Work on Superconducting Coils for a Large Mirror Fusion Test Facility*, Lawrence Livermore National Laboratory, Rept. UCRL-78891 (1977).
6. J. W. Ekin, "Fatigue and Stress Effects in NbTi and Nb_3Sn Multifilamentary Superconductors," *Advances in Cryogenic Engineering*, **24**, Plenum Press, New York (1977), p. 306.
7. J. H. Van Sant and R. M. Russ, "MFTF Magnet Thermal Control," *Advances in Cryogenics Engineering*, **25**, Plenum Press, New York (1979).
8. *Fluid Flow Data Book* (General Electric Co., Schenectady, N.Y., 1977).
9. C. D. Henning and E. N. C. Dalder, "Structural Materials for Fusion Magnets," in *Trans. Intl. Conf. on Structural Mechanics in Reactor Technology, 5th Berlin, 1979.* (Commission of the European Communities and the Nuclear Regulatory Commission, 1979), vol. N.
10. J. W. Wohlwend, C. D. Poniktera, and S. Dharmarajan, *Structural Analysis of the Magnet System for Mirror Fusion Test Facility (MFTF)*, General Dynamics/Convair, Rept. CASC-LLL-78-003 (1978).
11. H. I. McHenry and R. P. Reed, *Nucl. Eng. Design* (to be published).
12. F. R. Fickett and R. P. Reed, *Materials Studies for Magnetic Fusion Energy Applications at Low Temperatures-II*, National Bureau of Standards, Rept. NBS-IR-79-1609 (1979).
13. C. E. Witherell, Lawrence Livermore National Laboratory, private communication (1979).
14. E. Adams, E. Gregory, and W. Marancik, in *Proc. Intl. Conf. on Magnet Technology, 6th, Bratislava, Czechoslovakia, 1977.*
15. D. F. Neal, A. C. Barber, A. Woolcock, and J. A. F. Gidley, *Acta Metall.* **19**, 143 (1971).
16. R. M. Scanlan, J. E. Johnston, P. A. Waide, B. A. Zeitlin, G. B. Smith, and C. T. Nelson, "Manufacturing and Quality Assurance for the MFTF Superconductor Core," in *Proc. Symposium on Engineering Problems of Fusion Research, 8th, San Francisco, CA, 1979* (ORNL, IEEE, ANS, and DOE, 1979).
17. D. N. Cornish, D. W. Deis, and J. P. Zbasnik, "Cold-Pressure-Welded Joints in Large Multifilamentary Nb-Ti Superconductors," in *Proc. Symposium on Engineering Problems of Fusion Research, 7th, Knoxville, TN, 1977* (ORNL, IEEE, ANS, and DOE, 1977); IEEE Publication No. 77CH1267-4-NPS (1978) p. 1266.
18. J. W. Ekin, A. F. Clark, and J. C. Ho, *J. Appl. Phys.* **49**, 3410 (1978).
19. D. W. Deis, *MFTF Superconductor Core*, Lawrence Livermore National Laboratory, Spec. MEL77-001373-D (1979).
20. *Wrap Around Flat Pattern, MFTF Square Conductor*, Lawrence Livermore National Laboratory, Dwg. AAA78-105238 (1978).
21. D. W. Deis, *MFTF Stabilized Superconductor*, Lawrence Livermore National Laboratory, Spec. MEL77-001376-B (1978).
22. J. Horvath, Lawrence Livermore National Laboratory, internal memorandum to J. Van Sant, MF-TR-1.1.1 (June 26, 1979). Readers outside the Laboratory who desire further information on LLNL internal documents should address their inquiries to the Technical Information Department, Lawrence Livermore National Laboratory, Livermore, California 94550.

23. H. S. Freynik, Jr., D. R. Roach, D. W. Deis, and D. G. Hirzel, *Nickel-Chromium Strain Gauges for Cryogenic Stress Analysis of Superconducting Structures in High Magnetic Fields*, Lawrence Livermore National Laboratory, Rept. UCRL-72726 (1977).
24. R. Hintz, Lawrence Livermore National Laboratory, internal memorandum, MF-TR-1.1.2.6.2 (December 18, 1978).
25. R. E. Hinkle, *MFTF Coil Winding Procedure*, Lawrence Livermore National Laboratory, Spec. MEL78-001432 (1978).
26. *Interturn Spacer Strip, Superconductor Magnet Development, MX Coils*, Lawrence Livermore National Laboratory, Dwg. AAA76-115794 (1976).
27. *Perforated Sheet, MFTF Magnet System 1.1.2.6.2, Coil Insulation*, Lawrence Livermore National Laboratory, Dwg. AAA78-110166 (1978).
28. J. Horvath, Lawrence Livermore National Laboratory, internal memorandum (January 25, 1979).
29. R. Hinkle, Lawrence Livermore National Laboratory, internal memorandum to C. Henning (March 30, 1979).
30. J. Horvath, Lawrence Livermore National Laboratory, internal memorandum to C. Henning (October 16, 1979).
31. R. Hinkle, Lawrence Livermore National Laboratory, internal memorandum to C. Henning (October 15, 1979).
32. T. B. Miller, D. R. Roach, and H. S. Freynik, Jr., Lawrence Livermore National Laboratory, EMS-79-48 (October 22, 1979).
33. R. Hinkle, Lawrence Livermore National Laboratory, internal memorandum to C. Henning (September 10, 1979).
34. D. Deis, Lawrenee Livermore National Laboratory, internal memorandum to R. Hinkle, MF-TR-1.1.2.6 (May 18, 1978).
35. R. H. Bulmer, Lawrence Livermore National Laboratory, internal memorandum MF-EN-1.1 (February 3, 1978).
36. S. J. Sackett, *EFFI-A Code for Calculating the Electromagnetic Field, Force, and Inductance in Coil Systems of Arbitrary Geometry*, Lawrence Livermore National Laboratory, Rept. UCRL-52402 (1978).
37. S. J. Sackett, *EFFI-User's Manual*, Lawrence Livermore National Laboratory, Rept. UCID-17621 (1977).
38. S. J. Sackett, *Calculation of Electromagnetic Fields and Forces in Coil Systems of Arbitrary Geometry*, Lawrence Livermore National Laboratory, Rept. UCRL-77244 (1977).
39. J. Horvath, Lawrence Livermore National Laboratory, internal memorandum to R. Hintz (January 23, 1979).
40. J. Horvath, Lawrence Livermore National Laboratory, internal mamorandum to C. Henning, MF-TR-1.1.1.2 (March 28, 1979).
41. J. Horvath, Lawrence Livermore National Laboratory, internal memorandum to J. Van Sant, MF-TR-1.1.2 (May 7, 1979).
42. *Stress Analysis of the Coil Form and Coil Mounting Adapter for Lawrence Livermore Laboratory's Mirror Fusion Test Facility*, EG&G, Rept. SRO-226 (1978).
43. *Structural Stability Analysis for the Mirror Fusion Test Facility (MFTF) Jacket Assembly*, General Dynamics-Convair, Rept. GDC-LLL-79-003 (1979).
44. J. Horvath, Lawrence Livermore National Laboratory, internal memorandum to J. Van Sant (August 30, 1978) and to D. Roach and H. Freynik (November 9, 1978), MF-TR-1.1.1.4.
45. J. Horvath, Lawrence Livermore National Laboratory, internal memorandum to D. Cornish, MX-SR-1.1.1 (January 18, 1977).
46. J. Horvath, Lawrence Livermore National Laboratory, internal memorandum to V. Kopytoff (February 16, 1978).
47. R. W. Baldi and D. C. Poniktera, *Conductor Stress Analysis for the Mirror Fusion Test Facility (MFTF) Magnet System*, General Dynamics/Convair, Rept. GDC-LLL-79-001 (1979).

48. J. Horvath, Lawrence Livermore National Laboratory, internal memorandum to C. Henning (July 27, 1979).
49. R. C. Ling, *Coil Winder, MX Magnet*, Lawrence Livermore National Laboratory, Spec. MEL 76-001323 (1976).
50. R. C. Ling, "The Coil Winder for the Magnet of the MFTF," in *Proc. Symposium on Engineering Problems of Fusion Research, 7th Knoxville, TN, 1977* (ORNL, IEEE, ANS, and DOE. 1977), p. 728; Lawrence Livermore National Laboratory, Rept. UCRL 79744 (1977).
51. R. C. Ling, MFTF Reel Support, Lawrence Livermore National Laboratory, Spec. MEL 77-001342 (1977).
52. R. C. Ling, Y. Chang, and L. D. Hunt, "Reel Support for Winding the MFTF Magnet," in *Proc. Symposium on Engineering Problems of Fusion Research, 7th Knoxville, TN, 1977* (ORNL, IEEE, ANS, and DOE. 1977) p. 733; Lawrence Livermore National Laboratory, Rept. UCRL-79747 (1977).
53. D. Deis, *Results on MFTF Test-Coil Turn-to-Turn Insulation*, Lawrence Livermore National Laboratory, internal memorandum, MX-SR-6.1.2 (April 15, 1977).
54. D. Cornish, *Cold-Pressure-Welded Joints in Large Multifilamentary Nb-Ti Superconductors*, Lawrence Livermore National Laboratory, Rept. UCRL-79723 (1977).
55. *Coil Mounting Adapter Support*, Teledyne, Dwg. 550-011897 (1977).
56. *Coil Mounting Adapter*, Lawrence Livermore National Laboratory, Dwg. AAA78-105254 (1978).
57. R. E. Hinkle, *End Clamp Design*, Lawrence Livermore National Laboratory, internal memorandum, MX-EN01-4 (October 12, 1976).
58. R. E. Hinkle, *Side Clamp Design*, Lawrence Livermore National Laboratory, internal memorandum, MX-EN01-3 (October 8, 1976).
59. R. E. Hinkle, *Coil Clamp Assembly, Major Radius*, Lawrence Livermore National Laboratory, internal memorandum, MX-EN-6.1.2 (January 28, 1977).
60. Experimental load derived by winding similar layer on test coil Baseball and MFTF practice coil.
61. Experimental load required to remove 100% of the winding gap from a section of the conductor between clamps (10 feet).
62. *End Clamp Plate*, Lawrence Livermore National Laboratory, Dwg. AAA78-117505 (1978).
63. *Router Guide Assembly*, Lawrence Livermore National Laboratory, Dwg. AAA79-107707 (1979).
64. NEMA Standard (November 12, 1970).
65. Kapton polyimide, Type H, film properties, E.I. DuPont de Nemours and Co., Inc., bulletin H-1D.
66. J. Horvath, *MFTF Slip Plane Analysis*, Lawrence Livermore National Laboratory, internal memorandum (October 16, 1979).
67. R. E. Hinkle, *Reinforced Joint Stabilizer Design*, Lawrence Livermore National Laboratory, internal memorandum (November 13, 1978).
68. *MFTF Superconductor Joining Procedure*, Lawrence Livermore National Laboratory, Spec. MEL 78-001434 (1979).
69. R. Hintz, *Magnet Work Shop*, Lawrence Livermore National Laboratory, (July 1979).
70. *Instrumentation Plan for MFTF*, General Dynamics/Convair, Rept. CAS-LLL-78-005 (1979).
71. *Instrumentation Installation*, Lawrence Livermore National Laboratory, Dwg. AA79-101290 (1979).
72. R. F. O'Neill and D. H. Reimer, *Thermodynamic Analysis of the Magnet System for Mirror Fusion Test Facility*, General Dynamics, Rept. CASD-LLL-78-002 (1978).
73. R. F. O'Neill, *MFTF Superconducting Magnet Cooldown and Warmup Revised Thermal Analysis*, General Dynamics, Rept. 696-0-T-79-491 (1979).
74. *Handbook on Materials for Superconducting Machinery*, Battelle Memorial Institute, Rept. MCIC-HB-04 (1977), p. 5.1.3-12 (1976).
75. *Thermophysical Properties of Helium-4 from 4 to 3000 R with Pressures to 15,000 psia.*, National Bureau of Standards, Technical Note 622 (1972).
76. M. B. Kasen, *Properties of Filamentary-Reinforced Composites at Cryogenic Temperatures*, ASTM STP 580 (1975).

77. *304L Stainless Steel Thermal Conductivity*, Ref. 90 (1974) p. 8.1.2-7.
78. R. W. Jennings, *Thermophysical Properties of Selected Materials*, General Dynamics/Convair, Rept. 966-3-CHM-66-002 (1966). This Convair internal reference was employed for 316L stainless steel thermal conductivity and for 316 and 340L stainless steel specific heat. It was also employed for a best estimate of G-10 specific heat.
79. R. F. O'Neill and E. R. Neuharth, *Convair Thermal Analyzer Computer Program No. P4560*, General Dynamics/Convair, Rept. GDC-BTD69-005A (1969).
80. Intermagnetic General Corporation, *Quench Detection and Magnets Protection Study*, Lawrence Livermore National Laboratory, Rept. UCRL-15097 (1979).
81. E. W. Owen, *Currents and Voltages in the MFTF Coils During the Formation of a Normal Zone*, Lawrence Livermore National Laboratory, Rept. UCID-18490 (1980).
82. E. W. Owen, *Detection of a Normal Zone in the MFTF Magnets*, Lawrence Livermore National Laboratory, Rept. UCID-18309 (1979).
83. K. R. Loss and J. W. Wohlwend, *Structural Analysis of the Magnet System for Mirror Fusion Test Facility (MFTF), Addendum 1*, General Dynamics/Convair, Rept. CASD-LLL-78-003 (Addendum 1) (1979).
84. R. W. Baldi and D. E. Poniktera, *Case Fault Analysis for the Mirror Fusion Test Facility (MFTF) Magnet System*, General Dynamics/Convair, Rept. CASD-LLL-79-002 (1979).
85. K. Tada, *The Stress Analysis of Cracks Handbook*, Del Research Corporation (1973).
86. D. Read and S. Dharmarajan, *Material Property Data, 304LN and 316L Filler*, Telecan Record of Conversation between Dr. Read (NBS Boulder) and Dr. Dharmarajan (GDC), internal memorandum, MF-TF-T-2000-040 (June 28, 1978).
87. J. M. Wells, W. A. Logsdon, and R. Kossowsky, "Evaluation of Weldments in Austenitic Stainless Steels for Cryogenic Applications," presented at the *Intl. Cryogenics Materials Conference, Boulder, Colorado, 1977* (Westinghouse Research Laboratory, Scientific paper, 77-9D9-CRYMT-P5).
88. C. E. Witherell, *Welding Inner and Outer MX Magnet Cases*, Lawrence Livermore National Laboratory, interdepartmental communication to J. N. Doggett (October 7, 1976).
89. C. E. Witherell, *Welding Outer Case for MFTF Magnet*, Lawrence Livermore National Laboratory, interdepartmental communication to R. H. Butler (January 18, 1978).
90. R. H. Espey, "Weldability of 21-6-9 Stainless Steel," in *Materials Studies for Magnetic Fusion Energy Applications at Low Temperatures – I*" National Bureau of Standards, Rept. NBS-IR 78-884, (1978) pp. 169–177.
91. *Joining Huntington Alloys*, Huntington Alloy Products Division, International Nickel Company, Inc. (1972) pp. 36–39.
92. C. E. Witherell, Lawrence Livermore National Laboratory, interdepartmental communication to R. H. Bulmer (February 10, 1978).
93. R. R. Vandervoort and C. E. Witherell, Lawrence Livermore National Laboratory, interdepartmental communication to V. Kopytoff (May 8, 1978).
94. R. R. Vandervoort, "Mechanical Properties of Inconel 625 Welds in 21-6-9 Stainless Steel at 4 K," *Cryogenics*, **448** (1979).
95. *Standard Test Method for Plain-Strain Fracture-Toughness of Metallic Materials*, American Society for Testing Materials, Rept. ASTM-E-399-74 (1974) Sec. 7.1.1.
96. A. B. Crichten, J. R. Crisci, N. A. Freytag, V. Hasken, R. B. Hitchcock, and G. P. Yanok, "Gas-Metal Arc Welding," in *Welding Handbook* (American Welding Society, 1978) 7th ed., vol. 2, pp. 114–152.
97. C. E. Witherell, Lawrence Livermore National Laboratory, interdepartment communications (February 13, 1979).
98. O. W. Seth, Lawrence Livermore National Laboratory, private communication to E. Dalder (February 9, 1979).
99. O. W. Seth, Lawrence Livermore National Laboratory, private communication to C. E. Witherell (February 20, 1979).

100. A. Bachmann and B. L. Lundquist, "Properties of a Fully Austenitic Stainless Steel Weld Metal for Severe Corrosion Environments," *Welding Journal* **56**, 230 (1977).
101. H. I. McHenry, D. T. Read, and P. A. Steinmeyer, "Evaluation of Stainless Steel Weld Metals at Cryogenic Temperatures," in Materials Studies for Magnetic Fusion Energy Applications at Low Temperature - II National Bureau of Standards, Rept. NBS-IR-79-1609 (1979) pp. 299–312.
102. T. A. Whipple, "Mechanical Properties of Stainless Steel Weldments at Cryogenic Temperatures," presented at the NBS-DOE Workshop on Materials at Low Temperatures, Vail, Colorado, 1979.
103. General Dynamics-Convair, private communication, July 1979.
104. R. J. Castro and J. J. deCadenet, *Welding Metallurgy of Stainless and Heat-Resisting Steels*, (Cambridge University Press, New York, 1975) pp. 82–134.
105. C. D. Lundin and D. R. Spond, *The Ferrite-Fissuring Relationship in Austenitic Stainless Steel Weld Metals*, Welding Research Council, University of Tennessee, Knoxville, TN, Final Report (1975).
106. T. G. Gooch and J. Honeycombe, *Microcracking in Fully Austenitic Stainless Steel Weld Metal: Overall Assessment of the Welding Institute Investigation*, The Welding Institute, Rept. M/73/73 (1973).
107. J. Honeycombe and T. G. Gooch, *The Effect of Microcracks Upon the Mechanical Properties of Austenitic Stainless Steel Weld Metals*, The Welding Institute, Rept. M/69/72 (1972).
108. E. Dalder, private communication to C. D. Henning (December 7, 1979).